Comptes Rendus
de l'Académie des sciences

1878-1535 (electronic)

Physique

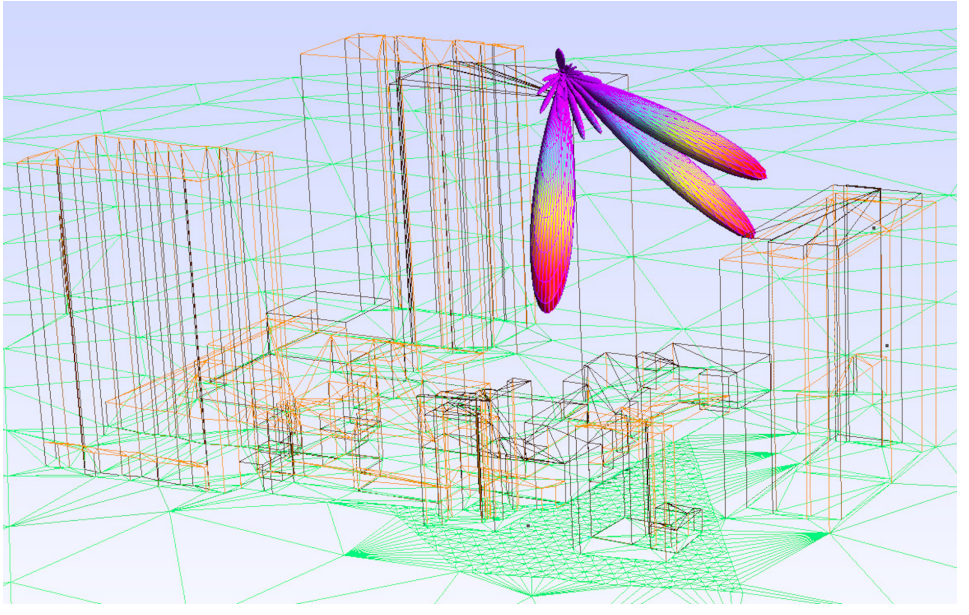

Volume 22, Special Issue S1, 2021

Special issue / *Numéro thématique*

URSI-France 2020 Workshop / *Journées URSI-France 2020*

Guest editor / *Rédacteur en chef invité*

Joe Wiart

Académie des sciences — Paris

INSTITUT DE FRANCE
Académie des sciences

CENTRE MERSENNE

Comptes Rendus

Physique

Objective of the journal

Comptes Rendus Physique is a peer-reviewed electronic journal of international standing, covering all fields of physics and astrophysics. It publishes mainly thematic issues, but also original research articles, preliminary announcements, review articles, historical perspectives, pedagogical texts or conference proceedings, without length limit, in English or in French. It also publishes special issues devoted to certain recent and/or significant aspects of the discipline, whose authors are chosen from among the most active researchers on the subject and whose coordination is assured by guest editors.

Comptes Rendus Physique is published according to a virtuous policy of diamond open access, free for authors (no publication fees) as well as for readers (immediate and permanent open access).

About the journal

All journal's information, including the text of published articles, which is fully open access, is available from the journal website at https://comptes-rendus.academie-sciences.fr/physique/.

Author enquiries

For enquiries relating to the submission of articles, please visit this journal's homepage at https://comptes-rendus.academie-sciences.fr/physique/.

Contact

Académie des sciences
23, quai de Conti, 75006 Paris, France
Tel: (+33) (0)1 44 41 43 72
CR-Physique@academie-sciences.fr

Comptes Rendus
Physique
2021, 22, nº S1

Contents / *Sommaire*

Comptes Rendus
Physique
2021, 22, nº S1, p. 1-2
https://doi.org/10.5802/crphys.73

URSI-France 2020 Workshop / *Journées URSI-France 2020*

Foreword

Joe Wiart [a]

[a] LTCI, Telecom Paris, Institut Polytechnique de Paris, Institut Mines Telecom, France
E-mail: Joe.wiart@mines.org

The year 2020 saw the commercial opening of fifth generation mobile phone networks. Since the 1990s, generations of mobile networks have followed one another every 10 years. The second generation, GSM, has democratized access to wireless mobile telephony. For the first time it was possible to be far from home while remaining close to family. The third generation in the 2000s and then 4G in the 2010s enabled mobile Internet access, first at moderate speed then at high/very high speed. These generations had in common that they had the human person at the center of uses. With 5G, wireless networks will have been designed for the first time from the outset with the aim of making possible both person-to-person, person-to-machine and machine-to-machine communications, giving potential access to a plethora of data-based services. The studies that have enabled the deployment of 5G are opening up new challenges. The technological developments specific to this generation, the frequency rise, the foreseeable evolutions that will require going beyond the framework of 5G towards the next generation, will continue to stimulate significant efforts and new lines of research, involving the academic world and industry. The deployment of this new generation also raises many societal questions linked on the one hand to the energy consumption of 5G and on the other to electromagnetic waves and associated exposure. The question of possible health impacts has given rise to numerous debates where the perception of risk has been favored at the expense of an objective assessment of the risk and of the actual exposure.

In view of all these challenges, opportunities and questions, URSI France decided in 2019 to organize its 2020 annual scientific workshop on the theme of "Networks of the future: 5G and beyond", on the campus of Telecom Paris (Institut Polytechnique de Paris), Palaiseau, March 11–13, 2020.

This special issue is organized in 8 papers covering different aspects and challenges of future networks. The first papers deal with the exposure induced by 5G system.

The paper entitled "*In-situ* evaluation of exposure induced by 5G antennas in the 3.4–3.8 GHz band" is written by E. Conil and J. B. Agnani. It describes exposure measurements performed in the vicinity of four pilot sites. The authors point out variations in the levels of exposure depending on use of network resources and they propose a new indicator of exposure.

The second one, "Numerical modeling of downlink electromagnetic wave exposure generated by 5G beamforming antennas", authored by N. Noé and F. Gaudaire, analyses scenarios used for numerical modeling of electromagnetic wave exposure to beamforming antennas. The authors underline the influence of the environment around the antennas on the distribution of the electric field.

The third paper, entitled "On the Measurement Procedures for the Assessment of the Specific Absorption Rate (SAR) from MIMO Cellular-Equipment of Fast Varying Relative Phases", is authored by M. Teniou, M. Ramdani, O. Jawad, T. Julien, S. Pannetrat and L. Aberbour. This paper introduces a measurement methodology for the evaluation of the specific absorption rate (SAR) of MIMO systems (multiple-input and multiple-output), in which the relative phases between the antennas are rapidly changing over very short durations.

The fourth paper, entitled "Investigating Sub-THz PHY Layer for Future High-data-rate Wireless Backhaul", is authored by G. Gougeon, Y. Corre, M. Z. Aslam, S. Bicaïs and J.-B. Doré and is dedicated to future networks. It analyses the feasibility and characteristics of the in-street sub-THz mesh backhauling. The study relies on a highly realistic simulation of the physical layer performance, based on a detailed geographical representation and on ray-based propagation modelling, for a new modulation scheme resistant to phase noise impairments.

The fifth paper, entitled "Multi-beam Modulated Metasurface Antenna for 5G Backhaul Applications at K-band", by J. Ruiz-García, M. Faenzi, A. Mahmoud, M. Ettorre, P. Potier, Ph. Pouliguen, R. Sauleau and D. González-Ovejero, explores the use of a new modulated metasurface (MTS) antenna topology as a solution for wireless backhaul at K band. The authors show that employing a modulated MTS, combined with the compactness of a pillbox approach, leads to a high-gain and low-profile antenna.

The sixth paper "Bandpass NGD function design for 5G microwave signal delay synchronization application" by S. Lalléchère, L. Rajaoarisoa, L. Clavier, R. Sanchez Galan and B. Ravelo, introduces a design method of simple bandpass (BP) NGD topology. The authors show that the BP NGD circuit can be useful for the improvement of phase linearity and group delay equalization of future 5G microwave devices.

The seventh paper, entitled "Enhanced Integrated Multiband HPM Radiator, combining a Hyperband Source with a High-Q Frequency Selective Surface" is authored by F. Albarracin-Vargas, F. Vega, C. Kasmi, D. Martinez and L. Ole Fichte. This work presents advances on the development of a resonant radiator and shows also that the system analysis methodology can be applied to other FSS geometries.

The last paper, by T. Caillet and entitled "Compatibility between EESS (passive) in band 23.6–24 GHz and 5G in band 24.25–27.5 GHz", describes the studies undertaken by several European countries for the protection of frequency bands used by satellites for the observation of the Earth. The elements provided in this document are the basis of the European position for WRC-19 on the protection of passive EESS in 23.6–24 GHz.

We hope that this special issue offers you the possibilities to have a wide view on the future networks, existing questions and challenges.

Joe Wiart
Président du Comité scientifique des
Journées URSI-France 2020
France
Joe.wiart@mines.org

Comptes Rendus
Physique
2021, 22, nº S1, p. 3-13
https://doi.org/10.5802/crphys.65

URSI-France 2020 Workshop / *Journées URSI-France 2020*

In-situ evaluation of exposure induced by 5G antennas in the 3.4–3.8 GHz band

Emmanuelle Conil[*, a] **and Jean-Benoît Agnani**[a]

[a] ANFR, 78 avenue du général de Gaulle, 94700, Maisons Alfort, France
E-mails: emmanuelle.conil@anfr.fr (E. Conil), jean-benoit.agnani@anfr.fr (J.-B. Agnani)

Abstract. In this paper, exposure induced in the vicinity of four pilot sites with 5G NR antennas in the 3.4–3.8 GHz band is assessed in-situ. Different manufacturers of antennas and different types of antenna are considered. Measurements are performed without any traffic, with continuous traffic in one direction and with on demand download of files. These measurements highlighted the variation in the level of exposure depending on use and led to the proposal of a new indicator to calculate the actual exposure created by 5G networks with steerable beams. This indicator results in a reduction factor that is used to assess the exposure in live conditions based on the configured maximum antenna power.

Keywords. 5G NR, EMF exposure, In-situ evaluation, Massive-MIMO, Beamsteering antennas.

1. Introduction

The key new elements of 5G New Radio, for exposure, in the new high frequency bands are steerable beam antennas to users, wider frequency bands, finer beams and alternating exposure (Time Division Duplex, TDD mode). The expected consequences are a lower level of exposure outside the beams, a higher exposure level in the beam and a shorter exposure time.

The French National Agency of Frequencies (ANFR) carried out exploratory exposure measurements during the first trials in collaboration with the operator and the antenna manufacturer in order to better understand 5G signals, to anticipate the need to update the in situ measurement protocol and to work on the definition of a new indicator. During the tests, the 5G pilots were not open to operator subscribers.

In this paper, we are focused on four trials to consider different antennas manufacturers and configurations.

* Corresponding author.

Table 1. List of 5G pilot sites under study

Town/City	Manufacturer	Antenna type	Height of antenna
Mérignac	Huawei	64T64R	8 m
Nozay	Nokia	64T64R	40 m
Douai	Ericsson	64T64R	28 m
Pau	Huawei	32T32R and 8T8R	45 m

2. Sites characteristics and measurement configuration

2.1. *Sites characteristics*

The sites selected for these measurements were chosen in order to cover different configurations of antennas tested in France in the 3.4–3.8 GHz band. These sites were also selected on the basis of the direct and unobstructed visibility of the antennas.

The sites that were the subject of this analysis are listed in Table 1.

The 5G NR standard defined by 3GPP [1] is very open and provides great flexibility in the choice of the many parameters that characterize the signal.

Similarly to 4G, 5G NR uses OFDMA (*orthogonal frequency division multiple access*) modulation, which is based on a division of the time/frequency matrix into elementary resources. In frequencies, the unit is the size of a sub-carrier in kHz; in time, it is the duration of an OFDM symbol in milliseconds. The OFDM symbols are grouped by 14 to form *slots*. These elementary resources are then grouped together to form frequency blocks (RB for *resource block*) containing a number of sub-carriers, one-millisecond sub-frames and ten-millisecond frames.

In the tested 3.4–3.8 GHz band, a TDD (*Time Division Duplexing*) mode is used. The split between *uplink* and *downlink* transmissions over time uses predefined frame formats. In the first cases observed in the field, this split was achieved by slot with a "DDDSU" format i.e. 3 successive D slots (reserved for downlink traffic), one S slot (for a switch shared between downlink traffic, a buffer zone without transmission and uplink traffic) and one U slot (reserved for uplink traffic). Using this configuration, the TDD ratio is about 75% in favour of the downlink. However, this first format tested in the field was not the one adopted by the French regulator Arcep in its decision No. 2019-0862 [2] on the synchronization of terrestrial networks in the 3.4–3.8 GHz band in continental France. Another format compatible with this Arcep decision was therefore also tested on certain pilots: the "DDDDDDDSUU" format which also leads to a TDD ratio of around 75% in favour of downlink.

The 5G NR antenna scans its environment to identify the users to be served using SSBs (*synchronisation signal blocks*) that occupy a bandwidth of 20 RB, i.e. 7.2 MHz in the case of the tested pilots.

Table 2 summarizes the main characteristics of the 5G signals tested on the pilots under study in this paper.

2.2. *Measurement configuration*

The sites were not open to users. Three types of configurations were tested:

- A—Configuration without traffic
  The base station only sent signaling, no users were connected to the network via the antenna.

Table 2. Main characteristics of 5G NR signals tested on the pilots under study

Parameters	Tested 5G pilots
Bandwidth	100 MHz
Spacing between sub-carriers	30 kHz
Size of an RB resource block	12 sub-carriers
Number of available resource blocks	273
Frame duration	10 ms
Slot duration	0.5 ms
Number of symbols per slot	14 symbols
Frame format	DDDSU or DDDDDDDSUU
TDD ratio	75% downlink
Signalling signal position (SSB)	Central
SSB periodicity	20 ms
Number of SSBs	1, 6, 7 or 8
Configured maximum power	200 W

Table 3. Electric field strength measured without traffic on the sites that were the subject of supplementary measurements

Town/City	Manufacturer	Electric field strength without traffic
Mérignac	Huawei	0.1 V/m–0.2 V/m
Nozay	Nokia	0.05 V/m–0.6 V/m
Douai	Ericsson	0.1 V/m
Pau	Huawei	0.01 V/m–0.1 V/m

- B—Test configuration with continuous traffic in a blocked beam
  In this configuration, the base station sent a constant and continuous stream of data in a given direction. This was achieved either by using a test mode implemented in the antenna or by using a user equipment (UE) downloading continuously data. In this configuration, the beam was therefore blocked in a given direction.
- C—File transfer configuration in a blocked beam
  In this configuration, traffic was generated by on-demand download using different size files (150 MB, 500 MB, 1 GB, 10 GB).

The measurements were taken at different points at 1.5 m above the ground, outdoors, in direct view of the antenna, within an antenna beam and outside the beams. A spectrum analyzer and a suitable tri-axis antenna probe have been used. The isotropic field strengths were assessed in the channel power mode with 100 MHz bandwidth and averaged over 6 min, in compliance with French regulation.

3. Results

3.1. *Exposure levels without traffic*

The isotropic averaged electric field strength measured at distances ranging from 35 m to 200 m from the 5G antennas, in the absence of traffic, over the 100 MHz transmitter frequency band is between 0.01 V/m and 0.6 V/m (see Table 3). In absence of traffic, exposure is extremely low compared to the limits of 61 V/m in this frequency band. Signaling traffic is very limited in 5G NR.

3.2. *Exposure levels with full traffic in a blocked beam*

3.2.1. *Huawei site in Mérignac*

On this site, a 64T64R Huawei antenna (64 transmitters and 64 receivers) is installed at a height of 8 m on a tree-shaped support (see Figure 1). The user equipment (UE) is in line of sight of the antenna at about 150 m. The maximum electric field was measured at this site at about 9 V/m in the vicinity of the UE served by the antenna.

Figure 2 shows, on the left, the electric field strength measured at different distances from the 5G antenna, along the UE axis. Reflections from the ground result in constructive and destructive field combinations which explain the field strength of only 4 V/m at 120 m from the antenna and the field strength of 8.5 V/m at 90 m from the antenna.

Figure 2 shows, on the right, the beam width at 1.5 m from the ground and at a distance of 150 m from the antenna. As one moves away from the UE served by the antenna, the averaged field strength drops rapidly (by a factor of 2 at 7.5 m on either side of the UE). On one side of the UE the reflection of the field on the large building is observed, this reflection causes a field strength of 8 V/m at about 15 m from the UE compared to a little more than 1 V/m at the same distance from the UE, but on the other side, with no reflection.

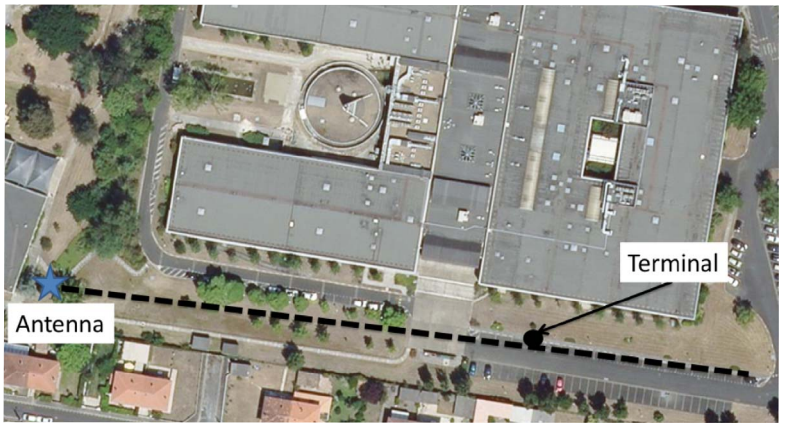

Figure 1. Satellite view of the Mérignac measurement site with the positioning of the antenna, the UE which receive the data sent by the antenna and the measurement axis in black.

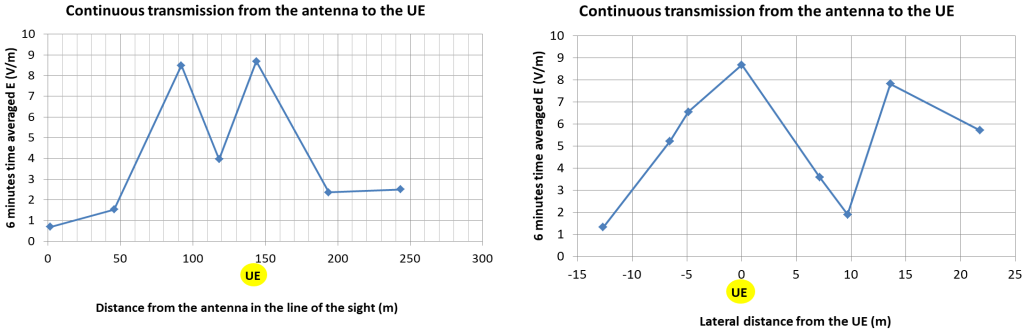

Figure 2. 6-min averaged field strengths measured over 100 MHz band in the antenna line-of-sight for the left figure and on the sides of UE for the right figure.

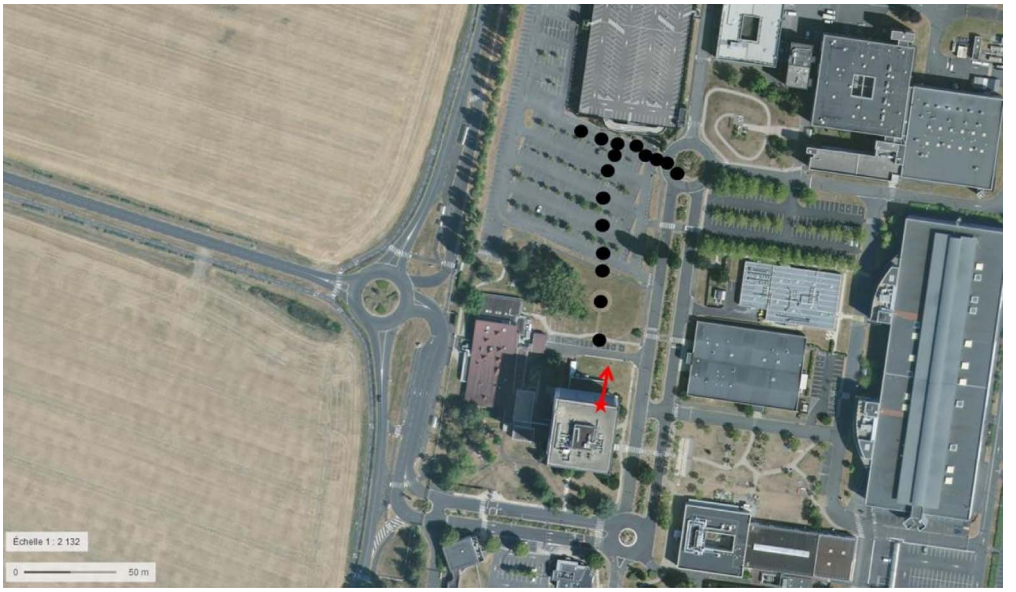

Figure 3. Satellite view of the Nozay site and sector no. 1 pointing towards a car park, the measurement points are shown in black. The antenna and its line of sight are shown in red.

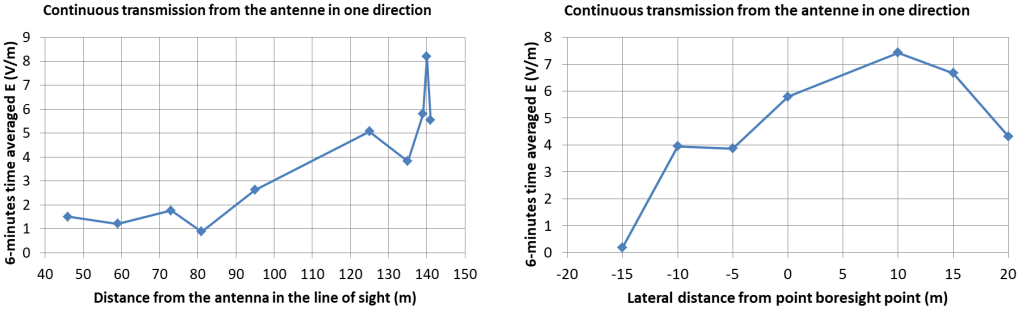

Figure 4. 6-min averaged electric field strengths measured at sector 1 of the Nokia site in Nozay on the left in the line of sight of the antenna and on the right perpendicular to the line of sight of the antenna at about 140 m from the antenna.

3.2.2. *Nokia site in Nozay*

In Nozay, two 64T64R Nokia antennas are installed on a 40 m high building. One of the antennas (sector 1) is installed on the top floor of the building at a height of 38.5 m and is directed towards a car park with a very high mechanical tilt of 18° (see Figure 3). An antenna test mode is used to send traffic continuously and with the antenna at maximum load. Considering the 18° tilt, the boresight point is at about 125 m from the antenna.

The maximum 6-min averaged field strength assessed over 100 MHz bandwidth is 6 V/m in this sector and these configurations. Figure 4 shows the field strengths measured in the line of sight of the antenna and perpendicular to it. A building located about 150 m from the antenna can explain the field variations between 130 and 140 m in the line of sight of the antenna.

The other antenna (sector 2) is installed on the roof of the building at a height of 41.5 m and is directed towards fields with a mechanical tilt of 8° (see Figure 5). The antenna test mode makes it

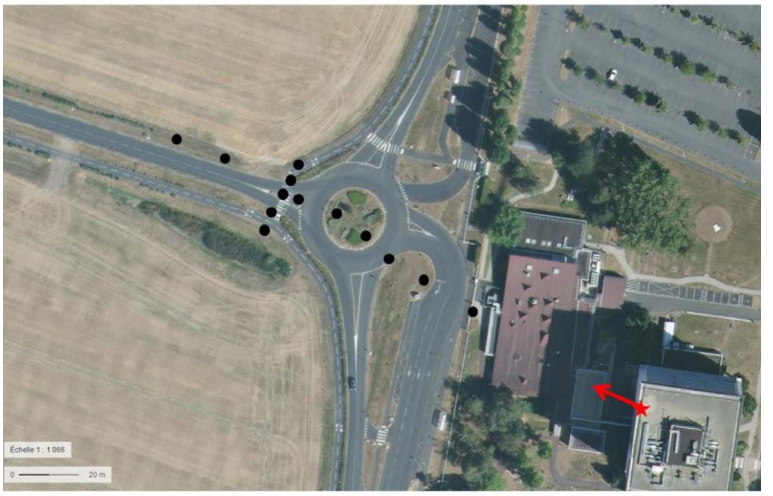

Figure 5. Sector 2 of Nokia's site in Nozay with an antenna installed at a height of 41.5 m (shown in red in the picture) and measuring points shown in black in the picture.

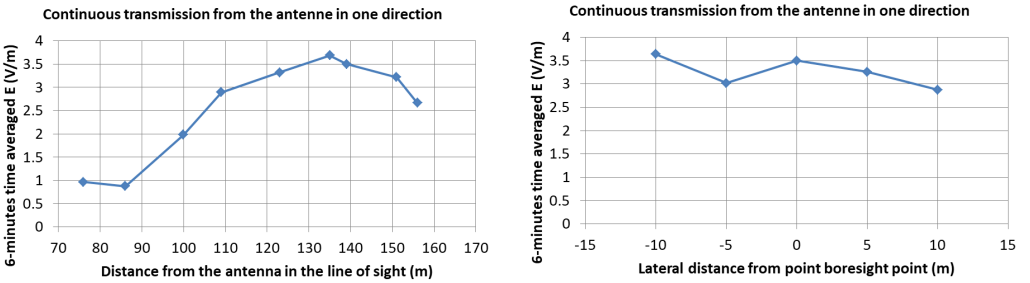

Figure 6. 6-min averaged electric field strengths measured at sector 4 of the Nokia site in Nozay on the left in the line of sight of the antenna and on the right perpendicular to the line of sight of the antenna at just under 140 m from the antenna.

possible for data to be transmitted in a tilted beam of 18° (8° mechanical and 10° electrical) with a boresight point at theoretically 134 m from the antenna.

The maximum 6-min averaged field strength assessed over 100 MHz bandwidth is 3.5 V/m in this sector and these configurations. This electric field strength is lower than in sector 1 because of the electrical tilt which causes gain losses. Figure 6 shows the field strengths measured in the line of sight of the antenna and perpendicular to it. Perpendicular to the main azimuth of the antenna, it was not possible to move away as far as in the other cases and the width of the beam is not identifiable.

3.2.3. *Ericsson site in Douai*

In Douai, the 64T64R antenna was located on a building at a height of 28 m and the measurements were taken near a terminal in a car park in direct view of the antenna and in its main line of sight (see Figure 7).

The maximum 6-min averaged field strength assessed over 100 MHz bandwidth is 1.4 V/m on this site in these configurations. The 6-min averaged field strengths measured along the axis of the antenna and at the sides of the modem are shown in Figure 8. These field strengths are lower

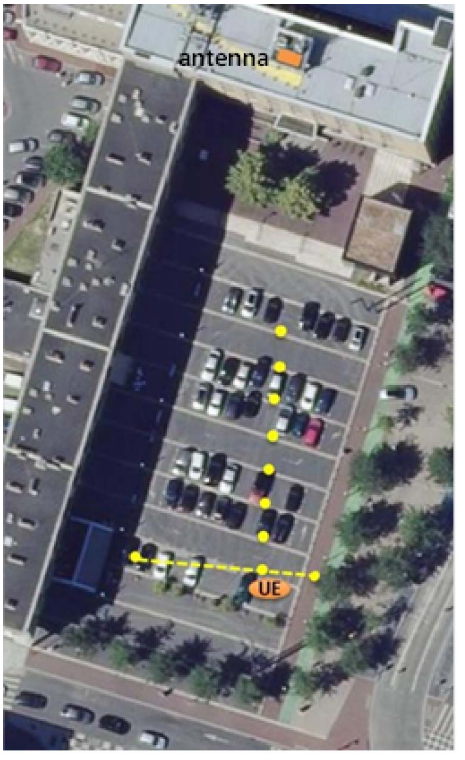

Figure 7. Satellite view of the Douai site with the antenna on a building roof, the user equipment (UE) in a car park (orange dot) and the measurement points in yellow.

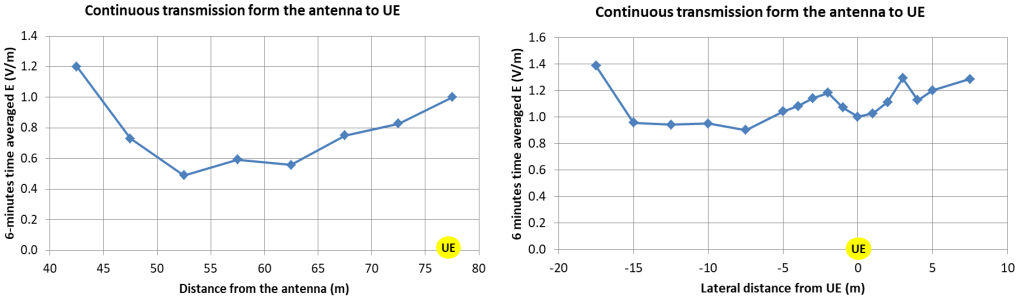

Figure 8. 6-min averaged field strengths measured over 100 MHz band in the antenna line-of-sight for the left figure and on the sides of UE for the right figure.

than those observed in similar conditions (such as at Nozay's site for example). These lower levels are probably due to a lower antenna steering capability and a lower level of gain in the direction of the terminal than the maximum antenna gain.

3.2.4. *Huawei site in Pau*

On this site, the antennas were located on a 45 m high building and traffic was continuously directed towards a UE located 125 m from the antenna, in direct view in a street at the foot of the building supporting the antennas (see Figure 9).

Figure 9. Satellite view of the Pau site with the antennas on a building 45 m high and the UE located 125 m from the antenna, in direct view in a street at the foot of the building supporting the antennas. The yellow and orange dots are the measuring points.

On this site, the transmission came from either a 32T32R or an 8T8R antenna. The 8T8R antenna's vertical orientation capability is much lower than that of the 32T32R antenna, which in turn is less than that of a 64T64R antenna.

The maximum field strengths averaged over 6 min and measured over 100 MHz bandwidth are 1.8 V/m in the case of the 32T32R antenna and 1 V/m in the case of the 8T8R antenna (see Figure 10). Probably neither the UE nor the measurement points were located in the direct lobe of the antenna, whether in the case of the 32T32R or the 8T8R antenna, which explains the lower field strengths than in other cases, such as in Toulouse or Mérignac for example.

3.3. *Exposure levels generated by on-demand downloads in a blocked beam*

In this configuration, exposure is triggered by a file download requested by the UE. Different file sizes from 150 MB to 10 GB were used. Thus there was no transmission throughout the 6 min of averaging time but only the time to transmit the files. As a reference, a measurement without traffic, i.e. without downloading, was also taken, as well as a measurement in the configuration discussed in the previous paragraph, i.e. with a continuous transmission at full antenna load in the direction of the equipment (named infinite case in the following tables).

Tables 4 and 5 summarize the field strengths measured over 6 min in the vicinity of the UE receiving the files of different sizes for the 2 sites where this configuration was processed. As it was on two different sites with two different antennas, the results are not exactly the same but the trend is the same.

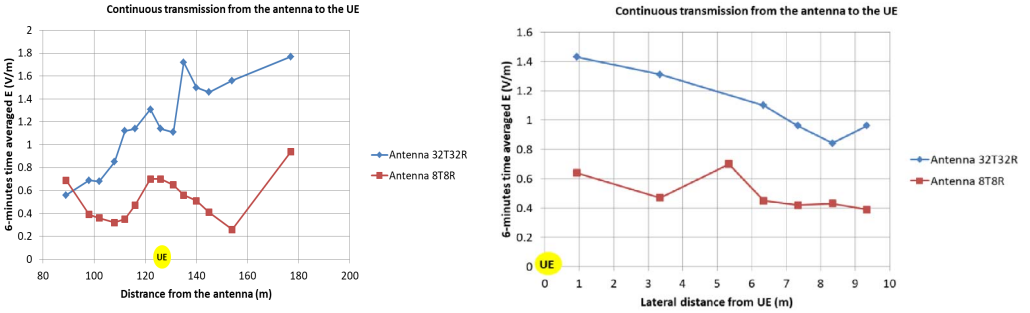

Figure 10. 6-min averaged field strengths measured on 100 MHz bandwidth in the antenna line-of-sight on the left and on the side of the UE on the right in the case of continuous transmission from the antenna—32T32R for the blue dots and the 8T8R antenna for the red dots.

Table 4. Averaged E field strengths measured over 6 min near a UE downloading files of different sizes from the Huawei site in Mérignac

Download time	File size	Averaged E field over 6 min
No downloads	0 MB	0.2 V/m
2 s	150 MB	0.5 V/m
7 s	500 MB	0.8 V/m
15 s	1 GB	1.1 V/m
150 s	10 GB	3.9 V/m
Infinity	Infinity	6.5 V/m

The infinite case corresponds to a continuous data transmission at full antenna load to the equipment.

Table 5. Averaged E field strengths measured over 6 min near a UE downloading files of different sizes on the Nokia site in Nozay

Download time	File size	Averaged E field over 6 min
No downloads	0 MB	0.28 V/m
19 s	1 GB	1.6 V/m
190 s	10 GB	4.8 V/m
Infinity	Infinity	8.2 V/m

The infinite case corresponds to a continuous data transmission at full antenna load to the equipment.

The exposure level is assessed over 6 min and therefore depends mainly on use. By way of comparison, a typical current monthly 4G 10 GB package could be used up in about 150 s (2 min 30 s) in the test conditions.

4. Exposure indicator

The measurement of exposure in the field in particular fulfils a need for information on the levels of exposure encountered on a daily basis. For legacy technologies, in the national guidelines on the presentation of simulation results published by the ANFR [3], a factor of 1.6 (i.e. 4 dB) is

Table 6. Estimated electric field strength at 100 m from a 5G antenna inside a building with a low power assumption and a high power assumption

5G	Low assumption	High assumption
Configured maximum power	80 W	200 W
Maximum gain	24 dBi	24 dBi
6-min attenuation	−13.5 dB	−13.5 dB
Glazing	−2 dB	−2 dB
TDD	−1.25 dB	−1.25 dB
E field estimated at 100 m	**1.1 V/m**	**1.8 V/m**

applied to the calculated electric field strength to account for statistical variations over 6 min for fixed beam antennas. For *indoor* use, it is supplemented by a factor of 20% (i.e. 2 dB) to take into account the attenuation by single glazing.

With 5G steered beam antennas, greater spatial and temporal variability is foreseeable. The level of exposure will indeed highly depend on the use. A new indicator is therefore proposed, based on a foreseeable use of 5G: one gigabyte of data sent in a given direction every 6 min. Assuming an average rate of 500 Mbps, the antenna will only transmit in the given direction for about 15 s out of the 6 min (about 4% of the time). This indicator for steered beam antennas has been included in the national guidelines on the presentation of simulation results of exposure to waves created by radio installations.

Assuming 8 active beams to serve the antenna coverage area, the area covered by the antenna will thus receive an average of 8 GB every 6 min, which corresponds to 960 GB per day assuming 12 h of network use per day, and 28,800 GB per month. There were 47.7 million 4G SIM cards in France at the end of 2018 and nearly 40,000 4G sites in service, which means that the average number of users per site can be estimated at 1000. Using these assumptions, the monthly 5G consumption would be 28 GB per month. By way of comparison, the averaged 4G consumption in the last quarter of 2018 was 7 GB per month on average: taking into account the fourfold increase in consumption currently observed, this volume takes into account the change in uses that seems likely to be brought about by 5G.

The assumptions used to define this indicator will be compared with the exposure measurements in the field for the 5G commercial networks and will be revised if necessary, particularly in the event of an increase in data consumption.

The interest of this indicator is that it makes it possible to assess exposure in real conditions by applying a reduction factor in relation to theoretical maximum antenna power.

For 5G, several factors will apply:

- the TDD ratio, as the antennas do not transmit continuously and provide listening ranges to receive signals from terminals: typically 75% power (i.e. 1.25 dB);
- the statistical variations over 6 min in the case of variable-beam antennas: considering the high beam mobility, which must constantly scan the entire sector covered by the antenna in order to serve the terminals located there: these are reflected by a power ratio of 4% (i.e. 13.5 dB);
- attenuation through glazing: identical to 4G, 20% in field (i.e. 2 dB).

This indicator results in a reduction factor which makes it possible to calculate the exposure in real conditions using the theoretical maximum antenna power.

The field strengths at 100 m from a 5G antenna resulting from the application of the indicator (see Table 6) appear to be comparable to those found at the same distance from a 4G antenna (see Table 7).

Table 7. Estimated electric field strength at 100 m from a 4G antenna inside a building with a typical current power assumption and a future power assumption

4G	Current	Future
Configured maximum power	60 W	160 W
Maximum antenna gain	18 dBi	18 dBi
6-min attenuation	−4 dB	−4 dB
Glazing	−2 dB	−2 dB
E field estimated at 100 m	**1.7 V/m**	**2.8 V/m**

However, for 4G, the reduction factor applies to the maximum antenna gain value which is only measured in the main antenna direction: outside this main direction, the field strength will be lower. On the other hand, with 5G steered beam antennas, the exposure calculated using the indicator will be valid in a higher number of directions.

5. Conclusion

These initial measurements considered several antenna configurations (different brands of antenna, different sizes) and different implementations of 5G NR (for example with a different number of SSBs or different frame formats).

The levels of the measured fields are all well below the regulatory limit value of 61 V/m in the 3.4–3.8 GHz frequency band.

The measurements which were carried out have confirmed that the exposure to the waves depends on many parameters, including:

- the distance between the antenna and the terminal, which is classic;
- the beam focus and the number of beams controlled by the antenna;
- the duration of presence of the beam in each direction and therefore of the data requests by the terminals in the beam.

These first measurements were carried out in special configurations allowing good control of the measurement conditions. A new indicator of exposure is proposed with a reduction factor of 13.5 dB on the maximum transmitted power to take into account the variability in time and space.

The measurements configurations were implemented in networks which were not open to the operators' customers. After the networks have been opened to the operators' customers, new measurements will make it possible to test more realistic configurations in terms of traffic and to supplement the conclusions of this paper.

References

[1] The Mobile Broadband Standard, "3GG specification series for 5G NR", https://www.3gpp.org/DynaReport/38-series.htm.

[2] Arcep – Autorité de régulation des communications électroniques et des postes, "Decision No. 2019-0862", 2019, https://www.arcep.fr/uploads/tx_gsavis/19-0862.pdf.

[3] ANFR – national guidelines on numerical simulations, "La simulation des champs", 2019, https://www.anfr.fr/controle-des-frequences/exposition-du-public-aux-ondes/la-simulation-de-champs/.

Comptes Rendus
Physique
2021, 22, nº S1, p. 15-24
https://doi.org/10.5802/crphys.61

URSI-France 2020 Workshop / *Journées URSI-France 2020*

Numerical modeling of downlink electromagnetic wave exposure generated by 5G beamforming antennas

Nicolas Noé[*, a] **and François Gaudaire**[b]

[a] CSTB, Division Acoustique Vibration Éclairage et Électromagnétisme, Nantes, France

[b] CSTB, Division Acoustique Vibration Éclairage et Électromagnétisme, Saint-Martin-d'Hères, France

E-mails: nicolas.noe@cstb.fr (N. Noé), francois.gaudaire@cstb.fr (F. Gaudaire)

Abstract. In this paper different scenarios were compared for the numerical modeling of electromagnetic wave exposure to beamforming antennas. These scenarios range from the simplest (using an average radiation pattern) to an almost realistic one (MU-MIMO beamforming taking into account user locations) with intermediate. The results underline the influence of the environment around the antennas on the distribution of the electric field.

Keywords. 5G, Antenna, Beamforming, Exposure, Ray-tracing.

Available online 6th May 2021

1. Introduction

The issue of EMF exposure to smart antennas used for 5G networks was approached as a first step from the point of view of dimensioning security perimeters around antennas. Indeed, to respect the health standards of workers exposure, a security perimeter has to be established around the antenna, inside of which it is prohibited to intervene when the antenna is in operation. Usually this perimeter is determined by calculating the minimum distance around the antenna beyond which the electric field level is always less than the mandatory threshold. This distance is evaluated in free space conditions and hence only depends on the Equivalent Isotropic Radiated Power (EIRP) of emitters.

For beamforming antennas, the antenna gain can vary dynamically up to a maximum gain when a beam is formed in a given direction. Hence using EIRP to compute security perimeters would lead to very long distance. Furthermore in this article we focus on the exposure of the general public in urban environments, beyond the security perimeter.

* Corresponding author.

2. Previous work

While there are several techniques to forecast EMF exposure in urban environments, they mainly rely on measurements [1–3] to feed numerical or statistical models. Therefore, they are not suitable for not-yet existing networks.

In this article we will focus on downlink exposure, leaving aside uplink exposure due to the mobile phone itself. Some metrics [4] exist to handle both simultaneously.

In [5–7] a statistical approach was used to obtain adapted values for security perimeter size for beamforming antennas. In [8] the method consisted in defining different exposure scenarios, depending on a very limited number of parameters: cell type (macro or micro), number of users served simultaneously K and duration of service D. Users were randomly distributed in the environment (80% indoor, 20% outdoor) and the antenna behavior was simulated (at full load) for a set duration of time (6 min) in order to obtain the probability distribution function (pdf) and cumulative distribution function (cdf) of the effective maximum gain of the antenna. The cumulative distribution function of the maximum gain therefore only depended on the chosen parameters. As a consequence this allowed the safety distance to be estimated with a given probability for a maximum level of exposure.

3. A new approach

The previous approach was perfectly suited for security perimeters dimensionning, but it seems insufficient for quantifying public exposure in real urban environments. The question of exposure is not limited to concerns of safety limits. One might indeed try to know precise local exposure (for the search for atypical points in France for example, or for compliance with much more restrictive local laws on the level of exposure such as in the Brussels-Capital region of Belgium). The local exposure may vary greatly depending on the actual configuration of the environment (layout of buildings, construction materials, ...), even for the same type of cell (macro or micro).

With the previous approach, an average diagram could be determined (as a complement to the maximum gain alone). This diagram can be used as an input to a detailed exposure simulation in a given environment, but it is likely that the simulation with the averaged diagram will give results different from the one that could be obtained by averaging the exposure over time.

We therefore propose a new approach to model exposure levels to beamforming antennas, by studying several antenna description scenarios, from the simplest one based on an average antenna diagram to the most complex one by taking into account beamforming operation. The beamforming scenario, being the most realistic, will be used as a the reference scenario.

The main objective of this study is to compare the influence of these different scenarios on electric field exposure level in representative urban environnements.

4. Antenna, environments and simulation method

4.1. *Antenna*

The input antennas can either be a single point with a far field radiation pattern or a set of radiating sub-elements with to model a Uniform Planar Array (UPA) antenna with its beamforming capability. The characteristics of the theoretical UPA antenna used in this study are:

- a 3GPP base element [9] with a 12.6 dBi gain, with a 65° horizontal aperture and a 20° vertical aperture,
- an 8×8 array of base elements with 0.5λ horizontal spacing and 0.6λ vertical spacing,

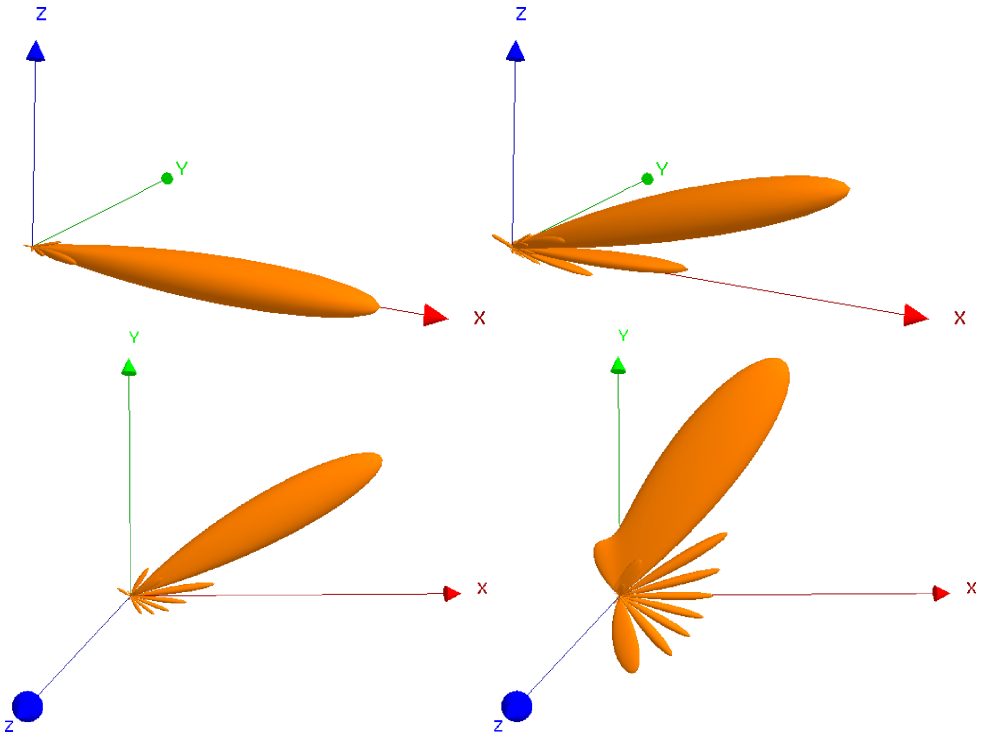

Figure 1. Beamforming to azimuth & tilt: 0° & 0° (top left), 0° & 20° (top right), 30° & 0° (bottom left), 60° & 0° (bottom right), linear scale.

- beams that can be steered from −60° to +60° horizontally and from −20° to +20° vertically,
- a 24.8 dBi gain for a single beam and an input power of 52.04 dBm (160 W).

Beamforming with this antenna is illustrated on Figure 1. It should be noted that the antenna diagram has strong sides lobes for extreme azimuths (close to 60°) since it is a purely analytical model and no side lobes suppression technique was applied.

5. Urban environments

Three different urban environments have been studied (see Figure 2). They were extracted from an exposure simulation study in the city of Paris and represent different configurations: one with mainly line-of-sight (LOS) exposure, one with other building reflections and a canyon street with indirect exposure. Only the buildings in the vicinity of the antenna have been kept (since only one antenna is used). The antenna is mechanically tilted 3° downward.

6. Simulation method

All simulations are performed using a 3D beam-tracing method [10]. This method computes paths between emitters and receivers, taking into account reflection, diffraction and transmission by obstacles, in order to get a complex electric field level (amplitude and phase).

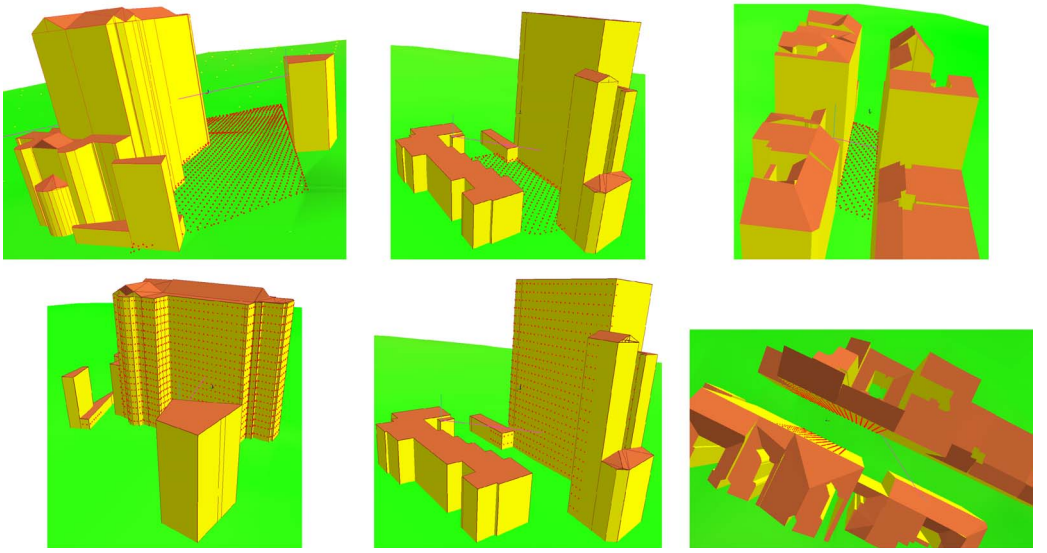

Figure 2. First (left), second (middle) and third (right) environments: antenna with default main lobe direction, ground (top) and facade (bottom) maps of receivers.

7. Scenarios for antenna modeling

7.1. *Scenario 0*

For this scenario a single simulation is performed with an averaged (over all beam directions) far field antenna diagram. This diagram has a 13.17 dBi gain and is illustrated on Figure 3. The averaging is done linearly on the emitted power by sampling the beams every 1° in both directions, hence from $121 \times 41 = 4961$ diagrams ($-60°$ to $60°$ horizontally and $-20°$ to $20°$ vertically).

7.2. *Scenario* $0'$

This slightly more complex scenario is related to the next ANFR guidelines for 5G networks exposure simulation. It is a kind of envelop of all beams, made from the 3GPP base element with a 120° horizontal aperture and a 40° vertical aperture and an (artificial) gain of 24.3 dBi. Once again a single simulation is performed with this diagram and then a 13.5 dB loss factor (defined in the ANFR guidelines [11]) is applied to the final result. This 13.5 dB loss factor fits in with a 1 GB download with a 500 Mbps during a 6 min measurement (hence a 4.4% antenna load).

This diagram is illustrated on Figure 3.

While the shape of the radiation pattern is slightly different from the averaged far field diagram (scenario 0), both scenarios are very similar. Another choice could have been to apply this reduction factor to a maximum envelop of all beams, but this would not significatively change the results.

7.3. *Scenario 1*

In this scenario, beams are formed in every possible direction (whatever the environment). One simulation is performed with a radiation pattern for each beam direction, with a 1° sampling

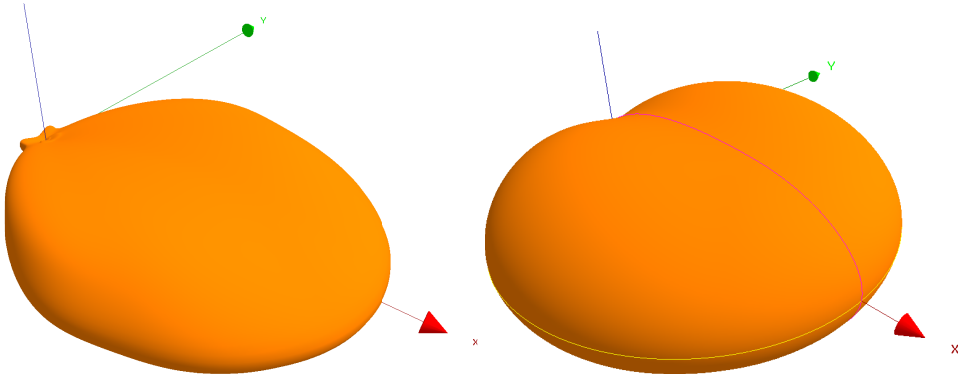

Figure 3. Far field diagrams (linear) used for scenarios 0 (left) and 0′ (right), linear scale.

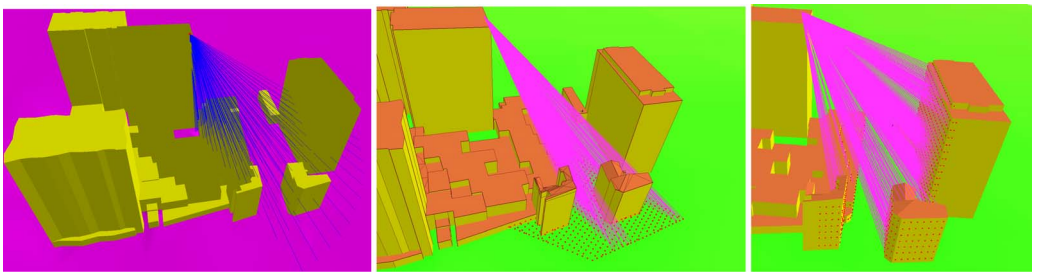

Figure 4. Scenario 1 (left, beams in all possible directions), scenario 1′ (middle and right, beams towards LOS exposure points on the ground and on the facades.

(hence 4961 simulations and exposure maps) as illustrated on Figure 4. In this scenario each beam has the same probability, not taking into account user location. That is to say that beams can be formed in directions where no user stands (toward the sky for instance).

Then an average exposure map is computed to compare with other scenarios. The averaged electric field is one again computed with a linear averaging on the power density.

7.4. *Scenario* 1′

A smart antenna is assumed to form beams in the direction of standing users. A rough approximation is to consider only beams pointing to exposure points (either on the ground or on the building frontages) that are in line-of-sight of the antenna. As a matter of fact users are either in the streets or in the building, and not floating in air yet.[1] The main point of this scenario is that it is easy to set up without any change in simulation tools, as it is only a sub-case of scenario 1. For the studied environments, LOS exposure points represent 10% of the ground surface and 20% of the facades (mainly the building in front of the antenna) as illustrated on Figure 4.

This scenario likely overestimates exposure, as the full power of the antenna is concentrated toward the exposure areas in LOS.

[1] That might change in the future with drones using mobile telephony network.

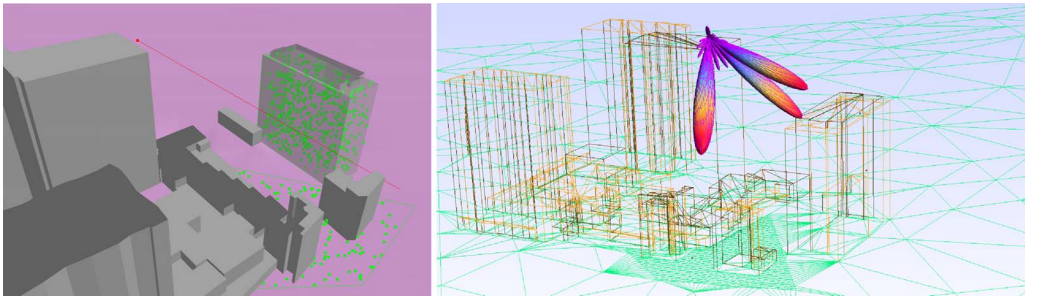

Figure 5. Scenario 2′: randomly generated UEs (left) and MU-MIMO beamforming for $K = 3$ served UEs (right).

7.5. *Scenario 2*

In this scenario, users are taken into account and beamforming is dynamically computed depending on the channel between the antennas sub-elements and the users. It aims to reproduce the real behaviour of a MU-MIMO beamforming antenna. The methods used to simulate such a behaviour are detailed in the following sections. In this scenario exposure points and user locations are independant.

The time dimension is introduced in this scenario by using the same drop duration D for all users and averaging the exposure maps over 6 min. In this work we set the value of D to 1 s, thus requiring 360 iterations to get an average exposure map.

7.5.1. *Users*

A pool of user equipments (UEs), i.e. terminals, is created in the urban environnement. UEs are randomly distributed on the ground and inside buildings with a ratio (for the same footprint) of 80% indoor UEs and 20% outdoor UEs. There are far more UEs in this pool than real users, in order to represent moving UEs and changing receiving conditions. In each environment described in this study, 640 UEs were generated (540 indoor, 100 outdoor), see Figure 5.

7.5.2. *Beamforming*

In this study we use zero-forcing beamforming [12]. It aims at maximizing the SINR (signal to interference and noise ratio) to serve a maximum number of UEs simultaneously. The beamforming weights applied to each sub-element are obtained by computing the pseudo-inverse of the channel matrix between the 64 sub-elements of the antenna and a set of N UEs ($N \leq 64$). The channel matrix is computed with the simulation method; each channel is the result of multiple paths contributions.

A greedy user selection algorithm is used to find the number K of UEs that can be served simultaneously amongst the N UEs with the overall higher rate with a given noise. Power allocation between users is done with a water-filling method. It is worth noting that K is not an actuel parameter here, as it is automatically computed (usually 3 or 4). An example of beamforming for 3 users simultaneously is illustrated on Figure 5.

7.5.3. *Full algorithm*

- UEs are handled by batches of 64 UEs. First these 64 UEs are removed from the pool of UEs (keeping the ratio between indoor and outdoor UEs, hence 50 indoor UEs and 14 outdoor UEs). Beamforming is performed on the 64 UEs by successive iterations, until every UE has been served (each UE has the same drop duration D). Hence

for each iteration i of beamforming, K_i UEs are served, with their allocated power. An exposure map is computed for each iteration, corresponding to the full antenna power.
- Once the 64 UEs have served, 64 others are extracted from the pool and so one, until the pool empties.
- When the pool is empty, an average (over the total number of iterations and also over time since D is constant) exposure map is computed.

The downlink rate for each UEs is computed but is not used yet, as a constant drop duration is considered for each UE. Each iteration, serving K_i UEs has a 1 s duration.

8. Results and analysis

8.1. *About results*

There are three urban environments and four scenarios in this work. Each scenario allows us to compute an exposure map of the antenna for all receiver points (1.5 m above the ground and on building facades). This exposure map is either directly computed from average diagrams (scenarios 0 and 0′), averaged from multiple simulations of several beams (scenarios 1 and 1′), or averaged over 6 min (scenario 2).

The cumulated distribution function (cdf) of the electric field is then computed for each scenario, for both ground and facade exposure.

8.2. *Preliminary results*

First we compare scenarios 0 (map with average diagram) and 1 (average of maps for each diagram). As expected the mean error between them is very close to zero. Nevertheless the error on some isolated points can be quite high. For instance the interference (either constructive or destructive) between direct and reflected field is amplified in scenario 0 due to the conservative diagram (with a far larger main lobe). Results for five highly exposed points (expressed in V/m) are shown on Table 1.

One important conclusion is that with an average diagram it is not necessary to perform an advanced simulation (with reflections for instance) since it introduces more error and decreases the accurray (scenario 0 without reflection gives results closer to scenario 1).

8.3. *Comparisons between scenarios*

For each urban environment, we compare the cumulated distribution function of electric field levels (in V/m) of the four antenna modelling scenarios. Cumulative distribution functions are calculated by averaging results on receivers for ground maps anf for building facade maps. This allows us to determine both the maximum value and the shape of the distribution function.

8.3.1. *On the ground (outdoor exposure)*

See Figure 6.

8.3.2. *On the facades (indoor exposure)*

See Figure 7.

8.3.3. *Analysis*

In all the cases of this study, the differences between scenario 0 (*a priori* average diagram of all beams) and scenario 1 (*a posteriori* average of all maps, with one map per beam) are significant,

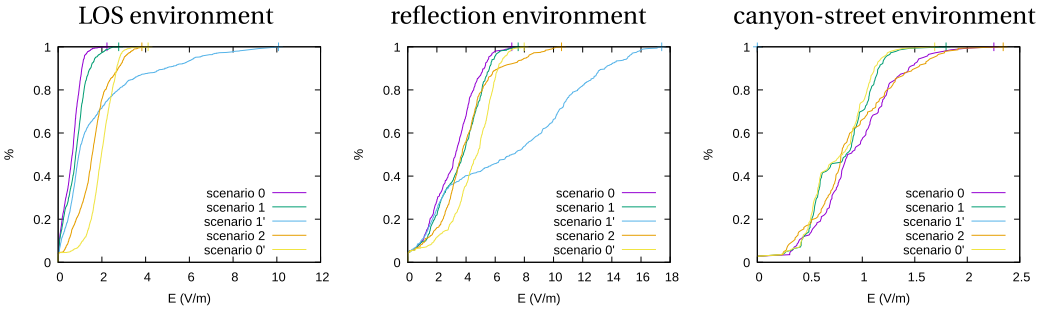

Figure 6. Comparisons between scenarios 0, 0′, 1, 1′ and 2, on the ground for the three environments.

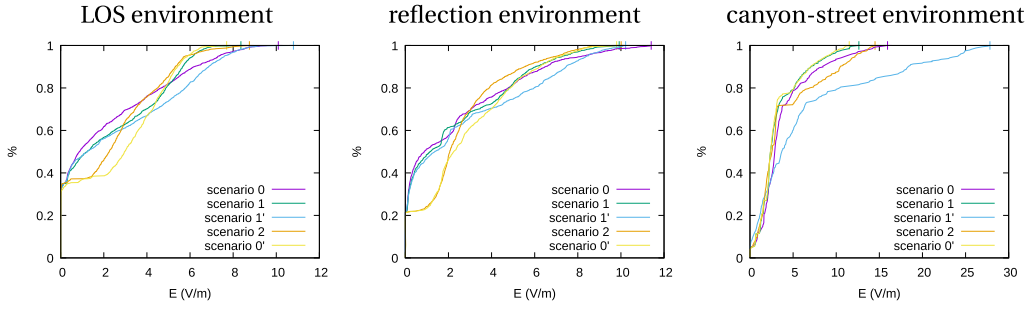

Figure 7. Comparisons between scenarios 0, 0′, 1, 1′ and 2, on the facades for the three environments.

Table 1. Differences between scenarios 0 and 1 at a few selected points with high exposure levels, with ($r = 2$) and without ($r = 0$) reflections taken into account

	#464		#100		#224		#202		#325	
Point	$r = 2$	$r = 0$	$r = 2$	$r = 0$	$r = 2$	$r = 0$	$r = 2$	$r = 0$	$r = 2$	$r = 0$
Scenario 0	4.41	7.44	4.51	7.29	4.56	6.99	6.44	7.37	6.45	6.72
Scenario 1	8.24	7.39	8.04	7.22	7.23	6.92	7.58	7.29	7.44	7.68

first concerning the shape of the distribution function of the electric field, and second concerning the maximum exposure level. In some cases the difference can reach 20%. The use of an average diagram has an influence on the characterization of the exposure levels, specially when there is a significant range of beam directions and changing beam shapes (with the appearance of non-negligible side lobes). This result should be confirmed with manufacturer antenna diagrams for which attenuation values of the side lobes would be available.

Most of the time, scenario 1′ (average of the maps for the beams in line of sight of the exposition areas) is a maximizing one. But it can be matched (for its maximum level) by scenario 2 in open range areas. In fact, the latter can form beams independently of direct visibility, in shadow areas or via reflected multi-paths.

The comparison between scenarios 0′ (ANFR guidelines) and 2 (dynamic beamforming) is what mainly interests us in this study. In all our case studies, scenario 2 gives maximum exposure levels higher or similar to scenario 0′. The usage assumptions of this study surely have a large influence on scenario 2: constant distribution of users at ground level and in buildings (this

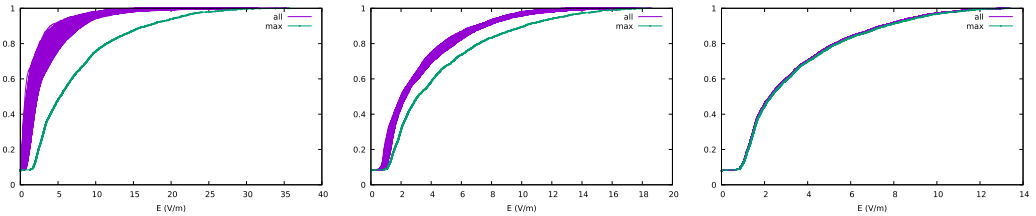

Figure 8. cdf of electric field, averaged over 6 min, for different drop durations D : D = 1 min (left), D = 10 s (middle) and D = 1 s (right).

could depend on the time of day), equal service (in assigned time) among all users, continuous service (antenna at full load). However, the differences between scenarios highlight that the configuration of the antenna environment has an influence on the exposure levels, which does not appear in the use of a scenario with a medium diagram, such as scenario 0 or 0′.

8.3.4. *Influence of drop duration*

On Figure 8 we illustrate the effect of the drop duration D on the cdf of the electric field. A sliding average over 6 min is used to get exposure maps as functions of time. We compare the cdf of all exposure maps (in magenta) with the cdf of the maximum exposure level at any point (in cyan). With D = 1 s, 6 min are enough to get a stable exposure level while for larger D values a longer averaging duration would be needed.

9. Conclusion and future work

By comparing the scenarios based on the use of an average diagram (scenarios 0 and 0′) with a scenario based on the average of the maps for all beams (scenario 1), it appeared that, in the case of beamforming antennas, taking into account the side lobes is essential to obtain a relevant characterization of the exposure levels. This is particularly the case for an antenna having a wide horizontal angular steering range. This conclusion should be refined and confirmed with more complete information from the manufacturers on the diagrams of the 5G antennas that will be field-deployed.

To make the calculation of exposure levels more precise and take into account the antenna environment, it is possible to implement in existing exposure tools a simple scenario which limits the focusing of the beams towards the points of exposure in line of sight of the antenna (scenario 1′). This scenario logically leads to a strong overestimation of the exposure in the majority of the cases studied. This result justifies the use and analysis of a more advanced scenario such as the scenario integrating dynamic beamforming, including the characteristics of the channel between the antenna and the users (scenario 2).

The study of the statistical distribution of the electric field levels shows that the scenarios based on an average diagram, including the scenario adopted for the ANFR guidelines, tend to overestimate the low electric field levels and under estimate the high levels, compared with the scenario incorporating dynamic beamforming (scenario 2). Here again, the statistical distribution of the electric field level shows the advantage of numerical modeling which considers both the environment of the antenna and its realistic behavior in channel estimation. The corollary of this conclusion is that accurately modeling the specific environment of the antenna (buildings, obstacles, etc.) for the numerical modeling of the exposure is of little interest with a simple hypothesis of a generic average antenna diagram.

This first study on a few sites therefore highlights the limitations of an overly simplified statistical approach for modeling the exposure due to smart antennas. These conclusions could

be confirmed by the study of larger sites, with more antennas and base stations and in larger-scale urban environments. The study could also be improved with access to more complete manufacturer data, on antennas actually deployed by telecom operators in the coming months. Future work could also focus on the spatial distribution of electric field, to go beyond the analysis of cumulated distribution functions of electric field levels. Preliminary works already show that this spatial distribution is strongly influenced by the environment.

Finally this study should be carried out on a larger scale. This would make it possible to analyze the shadowed areas (exposure "behind" the buildings in line of sight), areas located at a greater distance from the antenna, and more complex environments with several antennas and base stations. It is important to note that the level of exposure on the facade is the level outside but that the channel was formed with users located inside buildings (taking into account attenuation by the building walls). It should be noted that the methodology implemented in this study can be deployed operationally on any site, and requires calculation resources similar to those of a conventional calculation of exposure levels (only the diagrams of antennas are changed dynamically).

Acknowledgement

This work was partly funded by ANFR.

References

[1] S. Wang, J. Wiart, "Sensor-aided EMF exposure assessments in an urban environment using artificial neural networks", *Int. J. Environ. Res. Public Health* **17** (2020), article no. 3052.

[2] C. Regrain, J. Caudeville, R. de Seze, M. Guedda, A. Chobineh, P. Doncker, L. Petrillo, E. Chiaramello, M. Parazzini, W. Joseph, S. Aerts, A. Huss, J. Wiart, "Design of an integrated platform for mapping residential exposure to Rf-Emf sources", *Int. J. Environ. Res. Public Health* **17** (2020), article no. 5339.

[3] P. Combeau, N. Noé, S. Joumessi, F. Gaudaire, J.-B. Dufour, "A numerical simulation system for mobile telephony base station EMF exposure using smartphones as probes and a genetic algorithm to improve accuracy", *Prog. Electromagn. Res. B* **87** (2020), p. 111-129.

[4] S. Aerts, J. Wiart, L. Martens, W. Joseph, "Assessment of long-term spatio-temporal radiofrequency electromagnetic field exposure", *Environ. Res.* **161** (2017), p. 136-143.

[5] E. Degirmenci, B. Thors, C. Törnevik, "Assessment of compliance with RF EMF exposure limits: approximate methods for radio base station products utilizing array antennas with beam-forming capabilities", *IEEE Trans. Electromag. Compat.* **58** (2016), no. 4, p. 1110-1117.

[6] B. Thors, D. Colombi, Z. Ying, T. Bolin, C. Törnevik, "Exposure to RF EMF from array antennas in 5G mobile communication equipment", *IEEE Access* **4** (2016), p. 7469-7478.

[7] B. Thors, A. Furuskär, D. Colombi, C. Törnevik, "Time-averaged realistic maximum power levels for the assessment of radio frequency exposure for 5G radio base stations using massive MIMO", *IEEE Access* **5** (2017), p. 19711-19719.

[8] P. Baracca, A. Weber, T. Wild, C. Grangeat, "A statistical approach for RF exposure compliance boundary assessment in massive MIMO systems", in *WSA 2018; 22nd International ITG Workshop on Smart Antennas (Bochum, Germany, March 2018)*, 2018, p. 1-6.

[9] E. C. Commitee, "ECC Report 281: Analysis of the suitability of the regulatory technical conditions for 5G MFCN operation in the 3400–3800 MHz band", Tech. report, CEPT, 2018.

[10] N. Noé, F. Gaudaire, M. Diarra Bousso Lo, "Estimating and reducing uncertainties in ray-tracing techniques for electromagnetic field exposure in urban areas", in *2013 IEEE-APS Topical Conference on Antennas and Propagation in Wireless Communications (APWC) (Turin, Italy)*, IEEE, 2013, p. 652-655.

[11] ANFR, "Lignes directrices nationales sur la présentation des résultats de simulation de l'exposition aux ondes émises par les installations radioélectriques", Tech. report, ANFR, October 2019, https://www.anfr.fr/fileadmin/mediatheque/documents/expace/20191001-Lignes-directrices-nationales.pdf.

[12] N. S. G. Dimic, "On downlink beamforming with greedy user selection: performance analysis and a simple new algorithm", *IEEE Trans. Signal Process.* **53** (2015), no. 10, p. 3857-3868.

Comptes Rendus
Physique
2021, 22, nº S1, p. 25-33
https://doi.org/10.5802/crphys.64

URSI-France 2020 Workshop / *Journées URSI-France 2020*

On the measurement procedures for the assessment of the specific absorption rate (SAR) from MIMO cellular-equipment of fast varying relative phases

Mounir Teniou *, [a], **Mehdi Ramdani** [a], **Ourouk Jawad** [a], **Thomas Julien** [a], **Stéphane Pannetrat** [a] **and Lyazid Aberbour** [a]

[a] ART-Fi: Orsay, France

E-mails: mounir.teniou@art-fi.eu (M. Teniou), mehdi.ramdani@art-fi.eu (M. Ramdani), ourouk.jawad@art-fi.eu (O. Jawad), thomas.julien@art-fi.eu (T. Julien), stephane.pannetrat@art-fi.eu (S. Pannetrat), lyazid.aberbour@art-fi.eu (L. Aberbour)

Abstract. This article introduces a measurement methodology for the evaluation of the specific absorption rate (SAR) of MIMO systems (multiple-input and multiple-output) in which the relative phases between the antennas are rapidly changing and in very short durations.

This measurement methodology is enabled by SAR systems that uses vector field measurements combined with a vector spectral analysis of the measured radiofrequency signals for SAR assessment. By exploiting the equivalence principle and the uniqueness of the solution of Maxwell's equation, the proposed approach allows for an accurate SAR assessment of complex MIMO systems in a very short duration (few seconds).

Keywords. SAR, MIMO, Near field measurements, Vector field measurements, Time averaged SAR.

1. Introduction

In recent years, communication systems witnessed a fast evolution and an exponential increase of their complexity, especially with the advent of the LTE-advanced and the 5G. These technologies are based, among others, on the introduction of complex communication techniques such as the multiplication of transmitting and receiving antennas also known as MIMO (Multiple-Input Multiple-output) [1]. The introduction of MIMO technology in communication devices raises new challenges in the experimental evaluation of the specific absorption rate (SAR) and the human exposure to radiofrequency radiation [2]. In the case of a MIMO system, the exposure

* Corresponding author.

level must be evaluated for all the possible phase configurations of the system [3, 4]. By considering, for instance, a 10° step, this will lead to 36 measurements in the case of a two antennas system. Different methods have been proposed in the literature in order to evaluate the SAR of MIMO system with a small number of measurements [5, 6]. However, these methods assume a direct access to the excitations of the antennas of the systems, thus allowing a unique phase reference for the emitting antennas and the measurement. This is generally not possible in realistic practical scenarios.

In [7], time averaged local SAR is used in order to evaluate RF exposure level in the case of MIMO systems with a quick time domain variation. The proposed measurement method is faster than the classical measurement method. However, it requires a relatively large integration time of measurements in order to obtain the time averaged local SAR. It was also demonstrated in [7] that the sampling frequency used in the measurement of the electric field (E-field) is a key factor for the determination of the measurement time of this new MIMO technology. For measurement technologies using diode probes, the typical sampling frequency is of a few kHz. This requires the integration time of the measured signal ever more than one second at each point of the scan volume in order to achieve 2% precision on SAR. On the other hand, radiofrequency vector measurement technology such as the one introduced in [8] has a sampling frequency of 250 MHz that satisfy Shannon sampling theorem. The use of such high sampling frequency will drastically reduce the required integration time.

In this paper, a method for the evaluation of the time averaged SAR is presented. The proposed method is the extension of the work presented in [9, 10] to the case of MIMO systems with fast time domain variations. The proposed method is based on the use of vector measurement systems with a finite measurement probes grid and using E-field reconstruction in the measurement volume.

2. MIMO SAR measurement systems

2.1. *Signal classification*

Changes in the relative phases of signals transmitted by MIMO systems have a significant impact on the total electric field variation and thus on its time averaged value. Thus, it might be convenient to classify MIMO signals depending on the variation rate of their relative phases. In the context of SAR measurement, MIMO signals are divided into two main classes.

The first class consists of signals with relative phases that stay unchanged during a relatively long duration. The MIMO system configuration and the corresponding SAR value is then stable throughout this duration. This is for instance the case for antenna array systems where the phase shift is used to control the radiation pattern and the radiation direction. For these systems, the methods presented in [9,10] allow for a rigorous SAR assessment of all the possible configurations of the MIMO system using only $N+1$ measurements (where N is the number of antennas of the MIMO system). These fast and rigorous methods, requiring such minimal number of measurements, are made possible through the simultaneous measurement of the amplitude and the phase of the electric field phasor, combined with a vector spectral analysis of the radiofrequency signals for SAR assessment.

The second class includes signals with fast relative-phase variation rate. This is for instance the case when space–time coding is used such as STBC (space–time block code). In this type of configuration and due to its fast variation, the measurement of the SAR value is very difficult. However, it has been shown in [7] that the time averaged electric field converges when the integration time is sufficiently long. This integration time is significantly reduced if the SAR measurement system exploits a time domain acquisition of the demodulated RF signals with a sampling rate that satisfies the Shannon theorem.

In this paper, a SAR measurement method for MIMO systems with a fast relative phase variation rate is presented. This method is based on the work presented in [9, 10] and on the convergence of the time averaged electric field. The proposed method is intended for SAR measurement systems with vector probes measuring the electric field phasor, with a frequential selectivity and a time-domain acquisition of the demodulated radiofrequency signals.

2.2. *Time averaged SAR convergence*

The SAR value at a point (x, y, z) from space is defined as:

$$\mathrm{SAR}(x, y, z) = \frac{\sigma |\mathbf{E}(x, y, z)|^2}{2\rho} \tag{1}$$

where σ is the electric conductivity (S/m) and ρ is the mass density (kg/m^3) of the medium simulating the human tissues.

$\mathbf{E}(x, y, z)$ is the complex phasor of the harmonic electric-field.

Let's consider a MIMO system composed of two transmitting antennas that generates the electric fields $\mathbf{E}_1$ and $\mathbf{E}_2$ respectively. By injecting the signals $s_1(t)$ and $s_2(t)$ in these two antennas, the total field $\mathbf{E}_t$ is obtained as:

$$\mathbf{E}_t(x, y, z, t) = s_1(t)\mathbf{E}_1(x, y, z) + s_2(t)\mathbf{E}_2(x, y, z). \tag{2}$$

Squaring Equation (2) and calculating its module leads to:

$$\begin{aligned} |\mathbf{E}_t(x, y, z, t)|^2 \;=\; & |s_1(t)\mathbf{E}_1(x, y, z)|^2 + |s_2(t)\mathbf{E}_2(x, y, z)|^2 \\ & + 2|s_1(t)||s_2(t)||\mathbf{E}_1(x, y, z)||\mathbf{E}_2(x, y, z)|\cos(\phi(t)) \end{aligned} \tag{3}$$

with $\phi(t) = \arg(s_1(t)s_2(t)\mathbf{E}_1(x, y, z)\mathbf{E}_2(x, y, z))$.

The time averaging of (3) gives:

$$\begin{aligned} \langle |\mathbf{E}_t(x, y, z, t)|^2 \rangle \;=\; & \langle |s_1(t)|^2 \rangle |\mathbf{E}_1(x, y, z)|^2 + \langle |s_2(t)|^2 \rangle |\mathbf{E}_2(x, y, z)|^2 \\ & + 2\langle |s_1(t)||s_2(t)|\cos(\phi(t)) \rangle |\mathbf{E}_1(x, y, z)||\mathbf{E}_2(x, y, z)| \end{aligned} \tag{4}$$

where $\langle \cdot \rangle = (1/T)\int_0^T \cdot \mathrm{d}t$ and T is the integration time.

In the case of space time coding, the relative phase shift between the signals $s_1(t)$ and $s_2(t)$ changes very quickly, and the term $\langle |s_1(t)||s_2(t)|\cos(\phi(t)) \rangle$ tends to zero for a sufficiently long integration time T. From (4), the time average of the instantaneous SAR, $\mathrm{SAR}(x, y, z, t)$ becomes:

$$\langle \mathrm{SAR}(x, y, z, t) \rangle = \langle |s_1(t)|^2 \rangle \mathrm{SAR}_1(x, y, z) + \langle |s_2(t)|^2 \rangle \mathrm{SAR}_2(x, y, z) \tag{5}$$

where $\mathrm{SAR}_1(x, y, z)$ and $\mathrm{SAR}_2(x, y, z)$ are the local SAR values resulting respectively from the two antennas of the MIMO system when they are excited separately.

The result obtained in (5) can then be extended to the general case of an N antenna MIMO system.

2.3. *Measurement method*

In this section, a measurement method is proposed for SAR assessment in the case of MIMO signals with fast relative phase variation. Equation (5) shows that the assessment of the time averaged SAR of such systems comes down to the determination of the individual SAR ($\mathrm{SAR}_i(x, y, z)$) resulting from each antenna of the system, together with the time averaged value $\langle |s_i(t)|^2 \rangle$ of the squared amplitude of the signals that are injected in these antennas.

Considering these observations, a two steps method is proposed for the assessment of the time averaged SAR of MIMO systems composed of N antennas. The proposed method is presented as follows:

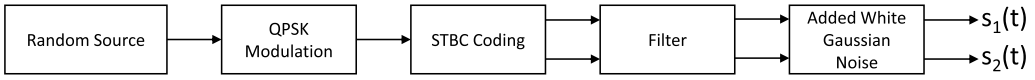

Figure 1. Block diagram of a MIMO system transmitting two signals with an STBC coding.

1. *Step 1—Configuration with slow relative phase variations:*
   a. Force the DUT to operate in a configuration with a stable relative phase distribution.
   b. Using $N+1$ measurements, follow the method presented in [9, 10] in order to obtain, at each point (x,y,z) of the measurement domain, the individual local SAR distributions $\mathrm{SAR}_i(x,y,z)$ corresponding to an independent excitation of each antenna of the MIMO system.
2. *Step 2—Configuration with fast relative phase variations:*
   a. Put the DUT in the configuration with quick relative phase variations where the SAR measurement needs to be performed.
   b. Measure the local instantaneous SAR $(\mathrm{SAR}(x_k,y_k,z_k,t))$ at K points (x_k,y_k,z_k) $(K \geq N)$ of the sensor grid, for a duration T that is sufficiently large in order to obtain the convergence of the time averaged local SAR $\langle \mathrm{SAR}(x_k,y_k,z_k,t)\rangle$.
   c. Using these time averaged SAR values $\langle \mathrm{SAR}(x_k,y_k,z_k,t)\rangle$ and the individual SAR of the MIMO antennas $\mathrm{SAR}_i(x,y,z)$ obtained in step 1, calculate the time averaged value $\langle |s_i(t)|^2\rangle = \alpha_i$ of the squared amplitude of the excitation signals, and this by minimizing the following expression:
   $$\min_{\alpha_i} \sum_{k=1}^{K} \left| \langle \mathrm{SAR}(x_k,y_k,z_k,t)\rangle - \sum_{i=1}^{N} \alpha_i \mathrm{SAR}_i(x_k,y_k,z_k) \right|. \tag{6}$$
   d. From the values of α_i, calculate the time averaged SAR value $\langle \mathrm{SAR}(x,y,z,t)\rangle$ at every point (x,y,z) of the measurement domain using the following equation:
   $$\langle \mathrm{SAR}(x,y,z,t)\rangle = \sum_{i=1}^{N} \alpha_i \mathrm{SAR}_i(x,y,z). \tag{7}$$

It should be noted that the step 1 of the proposed method does not need to be repeated if additional MIMO configurations with fast relative phase variations are considered.

3. Numerical validation

In order to validate the proposed measurement method, a MIMO configuration composed of two transmitting dipole antennas with a working frequency of 750 MHz. The electric field E generated by a horizontal dipole placed over a phantom of dielectric parameters $(\varepsilon_r;\sigma) = (42.8;0.85\ \mathrm{S/m})$ was simulated using the FDTD (Finite Difference in Time Domain) software EMPIRE XPU [11]. The result was then used in order to obtain the filed generated by the two dipole MIMO system for different configurations.

In order to obtain a high temporal variation of the relative phase, STBC coded time domain signals were generated by following the block diagram described in Figure 1. The obtained signals were then combined with the simulated electric fields in order to simulate a MIMO system with a high variation rate of the relative phase of the transmitted signals.

3.1. *Convergence of the time averaged SAR*

A first important step is the validation of the convergence of the time averaged SAR value and the validity of (5). This will allow us to determine the integration time T that is necessary in order to

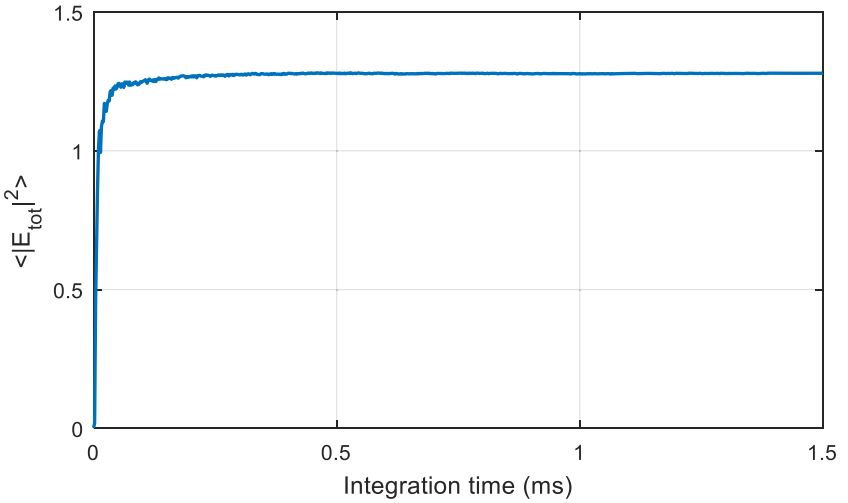

Figure 2. Variation of the time averaged squared amplitude of the electric field as a function of the integration time in (ms).

perform the measurement. In order to do that, random QPSK signals are generated by following the block diagram described in Figure 1. The generated signals have the following parameters:

Symbol rate: 10^6 symbol/s (corresponding to a symbol duration of 1 μs)
Modulation: QPSK
Coding: STBC
Filter: Raised cosine filter with a Rolloff factor of 0.25
Signal to Noise Ratio (SNR): 30 dB

The sampling frequency of the demodulated signals used by the SAR measurement system is set to 50 MHz, thus 5 times the higher frequency of the signal. It should be noted that acquiring analog-to-digital converters with a sampling frequency of several hundreds of MHz is very affordable.

The signals $s_1(t)$ and $s_2(t)$ that are generated at the end of this step are combined in order to obtain the total field (c_1 and c_2 are two complex numbers representing the electric fields generated by the two antennas of the system). The squared amplitude of the resulting total field is then averaged by varying the integration time T. The obtained results are represented in the Figure 2. It can be seen from the figure that the time averaged squared amplitude of the total electric field converges after a short integration time of a few fractions of milliseconds.

The calculation process is repeated many times (1000 times) for different sampling frequencies Fe in order to obtain the variation of the standard deviation with respect to the integration time. The obtained results are represented in the Figure 3. It can be seen from the figure that the sampling frequency has a significant effect on the convergence speed of the time averaged SAR. This is even more the case when the choice of the sampling frequency does not satisfy Shannon's theorem, such as for Fe = [10, 20, 50] MHz. This leads to a significant increase of the integration time ensuring less than 1% error. At the considered sampling frequency (50 MHz), the standard deviation is smaller than 1% for an integration time larger than 80 μs. It is this integration time that will be used for the rest of this article.

The generated STBC signals are combined with the electric fields of two horizontal dipoles simulated at a planar surface inside a flat phantom. This is performed in order to simulate SAR measurement system exploiting a vector measurement of the electric field over a finite

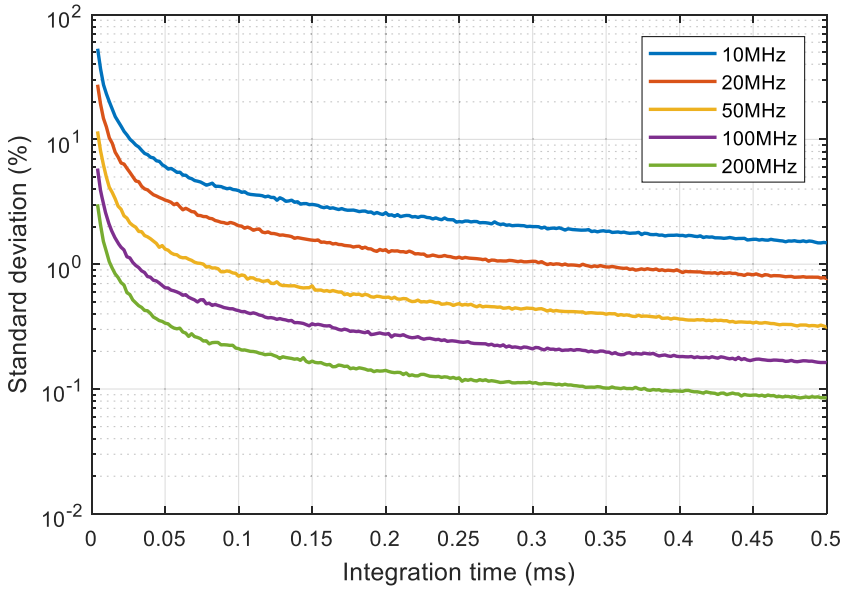

Figure 3. Variation of the local SAR standard deviation in % as a function of the integration time for different sampling frequencies. The results were obtained by repeating the calculation process 1000 times.

grid of sensors and using reconstruction algorithms of the electric field inside the measurement volume.

In the considered example, the two dipoles are centered at the positions à $(x, y) = (0, 30)$ mm and $(x, y) = (0, -30)$ mm and are rotated with respect to the z axis by $+45°$ et $-45°$ respectively. The considered transmitted signals have a unitary amplitude in order to obtain: $\langle|s_1(t)|^2\rangle = \langle|s_2(t)|^2\rangle = 1$. The corresponding variations of the time averaged squared amplitude of the fields over the measurement domain are represented in the Figure 4. It can be seen from the Figures 4(c) and (d) that the variations of $\langle|\mathbf{E}_t|^2\rangle$ and the sum $|\mathbf{E}_1|^2 + |\mathbf{E}_2|^2$ are very similar, with a quadratic error of less than 3%. This confirms that the term $\langle|s_1(t)||s_2(t)|\cos(\phi(t))\rangle$ to zero for a sufficiently large integration time and thus validating (5) on which the proposed measurement is based.

3.2. *Numerical validation of the proposed SAR measurement method for fast varying MIMO systems*

In order to validate the proposed measurement method, the steps described in Section 2.3 are applied on electric field distributions similar to those used in the previous subsection. The two considered dipoles are rotated by the angles $-15°$ and $45°$ respectively. The amplitudes of the generated excitation signals are defined in order to have $\langle|s_1(t)|^2\rangle = 0.5$ et $\langle|s_2(t)|^2\rangle = 0.75$.

As the first step of the measurement method was previously validated in [9, 10], the local SAR values $\mathrm{SAR}_1(x, y, z)$ and $\mathrm{SAR}_2(x, y, z)$ corresponding to the two antennas can be assumed to be known in every point of the measurement domain. The corresponding local SAR variations are represented in Figure 5.

By combining the signals $s_1(t)$ and $s_2(t)$ with the simulated electric fields E, the time averaged SAR values $\langle\mathrm{SAR}(x_k, y_k, z_k, t)\rangle$ is evaluated at two measurement points (x_1, y_1, z_1) and (x_2, y_2, z_2) of space (for example at the maximums of the individual local SAR of the two antennas).

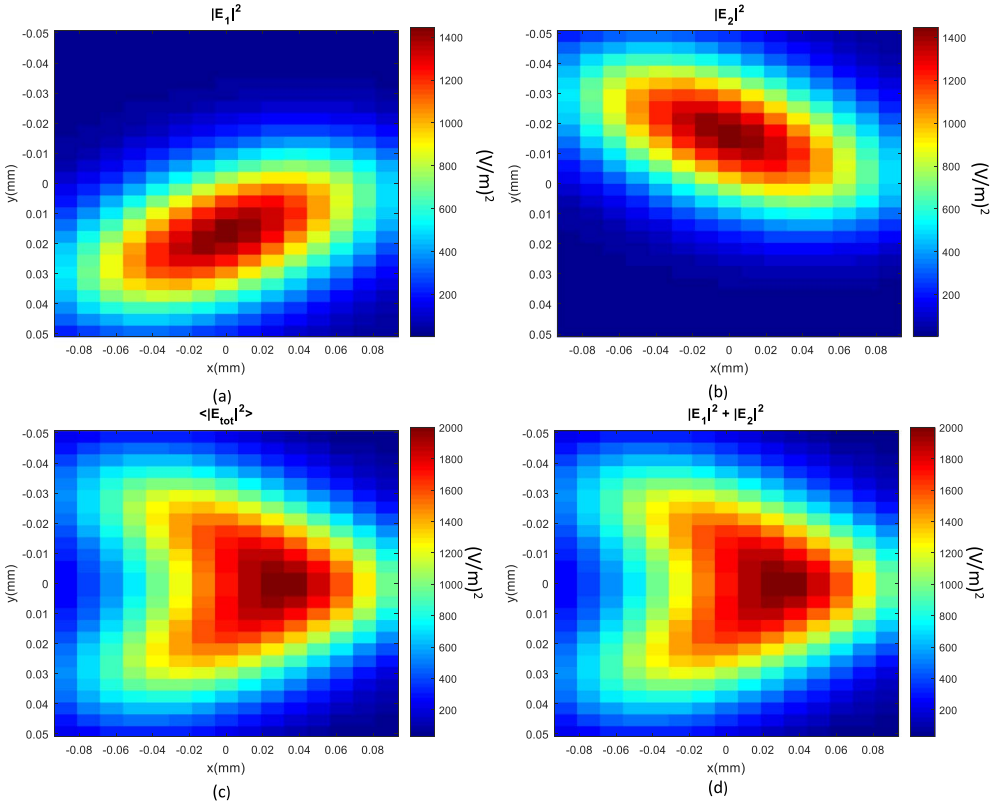

Figure 4. Variations of the time averaged squared field amplitudes in $(\mathrm{V/m})^2$: (a) $|E_1|^2$. (b) $|E_2|^2$. (c) $\langle|E_{\mathrm{tot}}|^2\rangle$. (d) $|E_1|^2+|E_2|^2$.

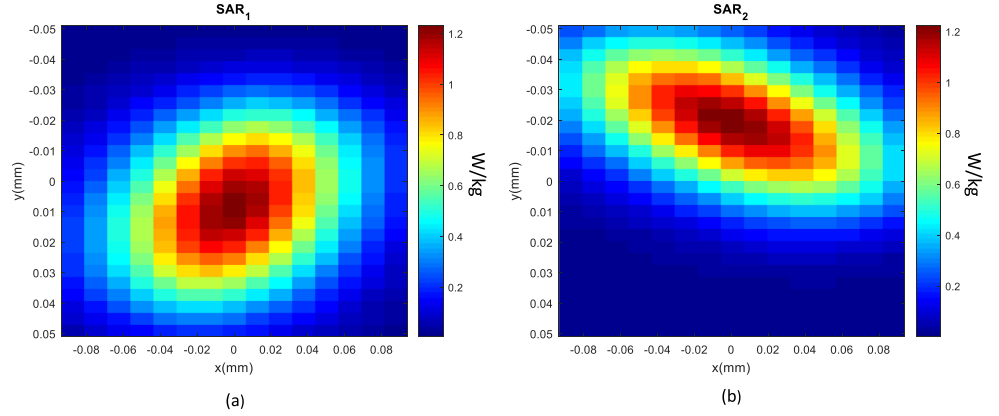

Figure 5. Variations of the simulated local SAR. (a) Antenna 1 alone. (b) Antenna 2 alone.

A cost function $f(\alpha_1,\alpha_2)$ is then defined as follows:

$$f(\alpha_1,\alpha_2)=\sum_{k=1}^{2}|\langle \mathrm{SAR}(x_k,y_k,z_k,t)\rangle-(\alpha_1\mathrm{SAR}_1(x_k,y_k,z_k)+\alpha_2\mathrm{SAR}_2(x_k,y_k,z_k))|. \tag{8}$$

The variations of the cost function defined in (8) are obtained by varying the values of the

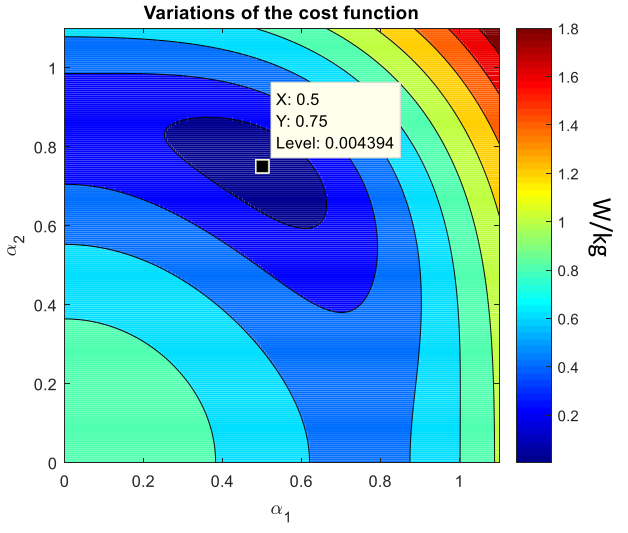

Figure 6. Variations of the cost function defined in (8).

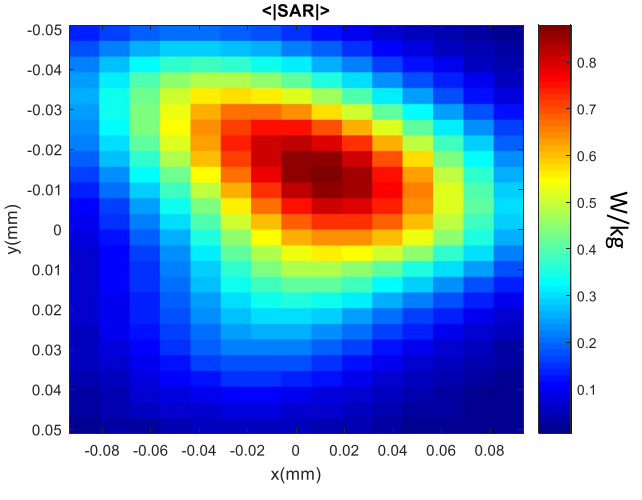

Figure 7. Time averaged local SAR distribution. The results were obtained by following the measurement method proposed in this article.

variables α_i. The corresponding results are represented in Figure 6. It can be seen from the figure that the minimum of the cost functions is obtained for $(\alpha_1, \alpha_2) = (0.5, 0.75)$. This corresponds to the time averaged values $\langle|s_1(t)|^2\rangle \langle|s_2(t)|^2\rangle$ that were imposed when generating the MIMO signals. From the retrieved values of (α_1, α_2), the time averaged SAR $\langle \mathrm{SAR}(x, y, z, t)\rangle$ is obtained at each point of the measurement domain by using (7). The obtained results are given in Figure 7.

In summary, the determination of the time averaged SAR (at every point of the measurement domain) in the case of a fast varying, 2 antenna MIMO system required a total of 3 classical vector measurements (with a typical duration of 15 s each) and two time averaged SAR measurements at two points of space (with a 80 µs duration each).

4. Conclusion

This article presents a practical, rigorous and innovative method for the experimental evaluation of electromagnetic exposure resulting from wireless communication devices exploiting MIMO technologies with a fast variation of the relative phases between its antennas. In the case of a N antenna system, the proposed method uses $N+1$ vector measurements of the E-field with distinct known interference states, coupled with additional measurements of time averaged SAR. These additional measurements have a typical duration a few milliseconds and are performed on a very limited number of points of the E-field sensor grid allowing the user to avoid the time integration of the instantaneous SAR at all the points of the measurement space.

In addition to its fastness and practicality, the proposed method is compatible with the case of a non-random relative phase distribution of the excitation signals as well as with the case of MIMO configurations of slow time domain variation. All the possible configurations of a MIMO can then be addressed with the same set of initial measurements.

Finally, it has been shown in this article that the use of the new generation of vector SAR-measurement systems, that integrates a time domain acquisition of the radiofrequency signal with a sufficiently high sampling frequency (a few hundreds of MHz), allow for the reduction of the SAR measurement time of fast varying MIMO systems to a few tens of seconds, whereas the typical measurement time is of a few tens of minutes with classical diode probe systems that suffer from a limitation of low sampling frequency of few kHz only.

Acknowledgement

We would like to thank Joe Wiart, Directeur of the C2M chair of Telecom ParisTech, for our very helpful exchanges on the subject of MIMO SAR.

References

[1] Z. Ying, “Antennas in cellular phones for mobile communications”, *Proc. IEEE* **100** (2012), no. 7, p. 2286-2296.

[2] ICNIRP, “Guidelines for limiting exposure to electromagnetic fields (100 kHz to 300 GHz)”, *Health Phys.* **118** (2020), no. 5, p. 483-524.

[3] International Electrotechnical Commission, “Guidance for evaluating exposure from multiple electromagnetic sources”, Tech. Report 62630, IEC, 2010, https://webstore.iec.ch/publication/7288.

[4] International Electrotechnical Commission, “Measurement procedure for the assessment of specific absorption rate of human exposure to radio frequency fields from hand-held and body-mounted wireless communication devices—Part 3: Vector measurement-based systems (Frequency range of 600 MHz to 6 GHz)”, Tech. Report 62209-3, IEC, 2019, https://webstore.iec.ch/publication/30773.

[5] N. Perentos *et al.*, “Exposure compliance methodologies for multiple input multiple output (MIMO) enabled networks and terminals”, *IEEE Trans. Antennas Propag.* **60** (2011), no. 2, p. 644-653.

[6] D. T. Le *et al.*, “A fast estimation technique for evaluating the specific absorption rate of multiple-antenna transmitting devices”, *IEEE Trans. Antennas Propag.* **65** (2017), no. 4, p. 1947-1957.

[7] D. T. Le *et al.*, “Averaging time required for measuring the specific absorption rate of a MIMO transmitter”, *IEEE Electromagn. Compat. Mag.* **3** (2014), no. 1, p. 57-64.

[8] B. Derat *et al.*, “A novel technology for fast and accurate specific absorption rate measurement”, in *2013 International Workshop on Antenna Technology (iWAT)*, IEEE, Karlsruhe, Germany, 2013, p. 363-366.

[9] L. Aberbour *et al.*, “Efficient experimental assessment of the specific absorption rate (SAR) induced by MIMO wireless communication devices; application of vector near-field measurement system”, in *2018 IEEE Conference on Antenna Measurements & Applications (CAMA)*, IEEE, Västerås, Sweden, 2018, p. 1-4.

[10] M. Teniou *et al.*, “A fast and rigorous assessment of the specific absorption rate (SAR) for MIMO cellular equipment based on vector near-field measurements”, in *2020 14th European Conference on Antennas and Propagation (EuCAP)*, IEEE, Copenhagen, Denmark, 2020, p. 1-5.

[11] EMPIRE XPU, https://www.empire.de/.

Comptes Rendus
Physique
2021, 22, nº S1, p. 35-45
https://doi.org/10.5802/crphys.66

URSI-France 2020 Workshop / *Journées URSI-France 2020*

Investigating sub-THz PHY layer for future high-data-rate wireless backhaul

Grégory Gougeon[*,a], **Yoan Corre**[*,a], **Mohammed Zahid Aslam**[*,a], **Simon Bicaïs**[*,b] **and Jean-Baptiste Doré**[*,b]

[a] SIRADEL, Saint-Grégoire, France

[b] CEA-Leti, Grenoble, France

E-mails: ggougeon@siradel.com (G. Gougeon), ycorre@siradel.com (Y. Corre), zaslam@siradel.com (M. Z. Aslam), simon.bicais@cea.fr (S. Bicaïs), jean-baptiste.dore@cea.fr (J.-B. Doré)

Abstract. Spectrum above 90 GHz is a promising investigation domain to offer future wireless networks with performance beyond IMT 2020 such as 100+ Gbit/s data rate or sub-ms latency. In particular, the huge available bandwidth can serve the backhaul transport network in the perspective of future ultra-dense deployments, and massive front-haul data streams. This paper investigates the feasibility and characteristics of the in-street sub-THz mesh backhauling. The study relies on the highly realistic simulation of the physical layer performance, based on detailed geographical representation, ray-based propagation modelling, RF phase noise impairment, and a new modulation scheme robust to phase noise. The achievable throughput is studied, and it is shown that each link of a dense mesh backhaul network can reliably deliver several Gbit/s per 1-GHz carrier bandwidth. The multi-path diversity is assessed, as well as the impact of rainfall and phase noise level.

Keywords. Sub TeraHertz, Backhaul, Propagation model, Modulation, Physical layer, 6G.

Available online 6th May 2021

1. Introduction

The long-term limitations of 5G standards are stressed already by the telecommunication industry and community research, for e.g. the delivery of ultra-low-latency broadband services, or the emergence of ubiquitous intelligence [1]. Next-generation wireless networks are imagined to be faster (1 Tbps for instance), more reactive (sub-ms latency), ultra-reliable and denser, thus allowing for very accurate positioning, highly-immersive experiences, smarter autonomous objects, etc. The exploitation of new and wider bandwidths at higher frequencies is an obvious and promising solution towards significantly increased data rates and capacity in beyond-5G or 6G communication systems. The "sub-THz" spectrum from 90 to 300 GHz is definitively identified

* Corresponding authors.

as a key enabler. An aggregated bandwidth of 58.6 GHz was identified in [2] as possibly available for terrestrial radio-communications between 90 and 200 GHz. Elaboration of future sub-THz systems is facing many challenges in particular at the PHY layer such as the strong propagation losses, or the increased phase noise (PN) w.r.t. mmWave band, which are both considered in this paper. Due to the strong propagation constraints, the short-range connectivity is a relevant sub-THz target application. However, the huge available bandwidth can also serve the backhaul transport network, and offer the future capacity required by cloud-RAN, ubiquitous AI (artificial intelligence), etc. That is why the authors explore the feasibility, reliability and achievable data rates of such a backhaul solution, with specific focus on the propagation impact.

First, the paper addresses the design of robust communication from both receiver and transmitter perspectives. The optimum symbol detection criterion and the corresponding probabilistic demapper is derived for channel with PN upon the maximum likelihood (ML) decision rule. We also propose a PN robust modulation scheme defined upon an efficient and structured constellation, adaptable to any signal-to-noise ratio (SNR) and PN variance. Second, the propagation channel properties are characterized and modelled to achieve a realistic evaluation of the proposed modulation. Only few sub-THz channel sounding campaigns have been published yet, as the equipments are new, complex and costly. Those recently realized inside a commercial hall [3], various indoor environments [4], a data center [5] or for outdoor–indoor penetration [6] are bringing valuable data that confirms the clear line-of-sight predominance, the channel sparsity and strong attenuations. Numerical simulation is a convenient solution to produce on-demand channel samples for any kind of scenario. The Volcano ray-based model [7], which has been updated up to the sub-THz frequencies, is employed in the present study to predict in-street propagation. The performance of the proposed modulation scheme has been assessed considering this propagation data combined with highly-directive antennas and different phase-noise conditions.

The PN characterization and proposed modulation scheme are presented in Section 2. The ray-based propagation model is described in Section 3. Then both techniques are combined in Section 4 to evaluate the performance of wireless outdoor backhaul links: throughput versus range, multi-path diversity, robustness to rainfall and phase noise. A conclusion is given in Section 5.

2. Phase noise and proposed modulation

PN in communications systems arises from the integration and amplification of noise sources within the circuitry by the phase-locked loop (PLL). Due to integration, PN presents a cumulative nature. Under the assumption that the oscillator is only subject to thermal noise, the oscillator PN is described with the superposition of a cumulative Wiener process (a Gaussian random-walk) and an uncorrelated Gaussian one. These stochastic processes respectively express the integration and amplification within the PLL of thermal noise. The spectrum of oscillator PN is in this case described by a colored characteristic (Wiener PN) and a white noise floor K0 (Gaussian PN). However, it has been shown in [8] and confirmed in [9] that the impact on communication performance of the Wiener PN is negligible in comparison to the Gaussian in case of large bandwidth systems. Subsequently, for sub-THz systems, the impact of oscillator PN on received symbols may be efficiently modeled with a Gaussian distribution. That is

$$r = s \cdot \mathrm{e}^{\mathrm{j}\phi} + n, \quad \phi \sim N(0, \sigma_p^2),$$

where r is the received symbol, s is the modulated one, ϕ is the oscillator PN, and n is the thermal noise with spectral density N_0. In the rest of the paper, a medium PN level with $\sigma_p^2 = 10^{-2}$ or a

strong PN level with $\sigma_p^2 = 10^{-1}$ have been considered. This corresponds to a floor noise spectral density $N_0 = -110$ dBc/Hz for a channel bandwidth of 1 GHz.

The design of the optimum modulation scheme for the PN channels has been largely investigated in the literature [10]. However many works derive complex optimization problems to determine the shape of a constellation, we have considered a pragmatic approach supported by a theoretical framework. Under a high-SNR assumption, it can be demonstrated that the channel with PN in the polar domain (amplitude/phase) is highly similar to an additive white Gaussian noise channel in the complex plane [11]. It follows that the optimum modulation, i.e. minimizing the symbol error probability, is the constellation that maximizes the minimum distance. Then for a fixed modulation order and average power, characterizing the optimal constellation may be interpreted as finding the densest sphere packing in the polar domain. Therefore, the optimal constellation is defined upon an hexagonal lattice in the polar domain. Nevertheless, for implementation considerations, it is relevant to exploit a rectangular lattice since the corresponding demodulation and binary labelling are greatly simplified with minor loss in performance. As a result, we propose the polar quadrature amplitude modulation P-QAM [12] that will be considered as the modulation scheme throughout the performance assessment.

3. Ray-based sub-THz modelling

The Volcano ray-tracing propagation channel model has recently been extended to support the sub-THz spectrum between 90 and 300 GHz [7], and serves in the assessment of new technologies and scenarios. Only few measurements have been published at those frequencies, e.g. [4]. However, the predicted mechanisms rely on a physical calculation approach—Fresnel reflection, uniform theory of diffraction (UTD) and knife-edge diffraction—, which are already exploited and validated in the 5G millimeter-wave (mmWave) spectrum. Major mmWave trends are supposed to persist: diffractions become negligible; critical blockage may come from environment details, in particular furniture and trees; reflections are still strong except when impacted by local surface roughness.

Volcano predicts 3D ray-paths from the combination of multiple reflections, transmission and diffractions, based on a fast ray-launching technique, the UTD and knife-edge diffraction coefficients. Both the transmission through the vegetation and the diffraction on bottom and top of the foliage are considered. The transmission is computed from an average linear loss (dB/m) that is multiplied by the propagation length inside the foliage. As illustrated in Figure 1, Volcano does support LiDAR point cloud data for outdoor predictions. This data allow the model to evaluate the blockage and transmission losses due to the trees and street furniture in a more realistic way compared to conventional geographical database.

The ray-tracing simulations, using LiDAR data, have been compared to in-street point-to-point measurements carried out with a Terragraph beamforming equipment at 60 GHz [13]. It was shown that with a precise representation of the trees and a proper calibration of the vegetation linear loss, the simulator can reproduce similar path-loss and channel properties (i.e. same propagation path sparsity) as observed in the measurements.

Some of the ray-tracing parameters and calculation methods are derived from ITU recommendations. The validity range of the ITU attenuation models for rain and atmospheric gas [14] encompasses the considered sub-THz frequencies. However, the application range of the ITU dielectric material properties, such as permittivity and conductivity, is not covering the sub-THz domain [15] (Table 3). We then have decided to employ the existing values beyond the recommended upper limit, which is typically 100 GHz, as in absence of any other simple alternative, this might be an acceptable assumption for exploration and preliminary studies.

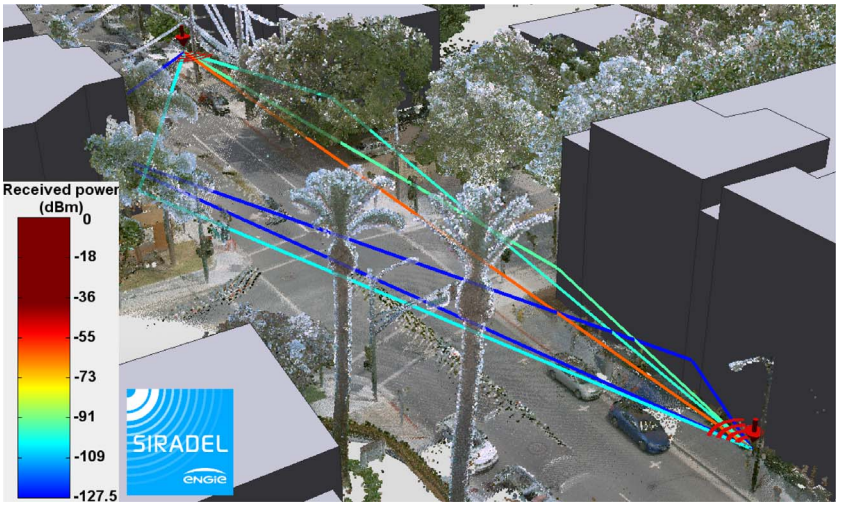

Figure 1. Multi-path propagation considering fine 3D tree's representation.

4. In-street backhaul evaluation

4.1. *System parameters and scenario*

Mapping between SNR levels and spectral efficiency is derived from the previously described P-QAM modulation scheme and following assumptions. A perfectly synchronized single-carrier modulation is considered. The channel phase shift is perfectly estimated and corrected. A forward error correction (FEC) scheme based on the 5G-NR LDPC with an input packet size of 1500 bytes is considered with a coding rate ranging from 0.3 to 0.9. The performance of the physical layer was first assessed to determine the best set of parameters: coding rate, modulation order and modulation shape given the SNR, the PN level and the targeted packet error rate of 10^{-2}. Resulting spectral efficiency with medium PN level goes from 0.6 bps/Hz at −0.8 dB SNR, to 7.2 bps/Hz at 29.7 dB SNR.

The system is operating in the D-band (150 GHz), with a bandwidth of possibly several tenths of GHz, divided in 1-GHz channels. The effective bandwidth of the signal is 800 MHz with a 20% overhead due to the control plane. The maximum reachable throughput is then 4.6 Gbps per channel (Gbps/ch). Parameters regarding the transmit power, antenna, and link budget are given in Table 1 for each simulated scenario. The adjustment factor in the last row of the table is used as a varying parameter to evaluate the sensitivity of the simulated system to any change or uncertainty in the link budget. As an example, a positive adjustment can be used to assess the impact of a larger transmit power or reduced noise figure.

The in-street backhaul scenario is run in a dense-urban densely-vegetated environment, San José downtown, California. The digital geographical data is composed of 3D vector buildings and a point cloud LiDAR data where trees and main street furniture e.g. lampposts are identified. A subset of 134 lampposts in this area is used as virtual sub-THz device positions. Antennas are localized at 8 m above the ground. All possible lamppost-to-lamppost links with range lower than 200 m are computed at frequency 150 GHz, leading to a total of 1873 predicted links.

4.2. *Performance evaluation*

The visibility conditions is first determined for each node-to-node link: 136 line-of-sight (LoS) links; 553 vegetation obstructions (Obstructed-LoS or OLoS); and 1204 building obstructions

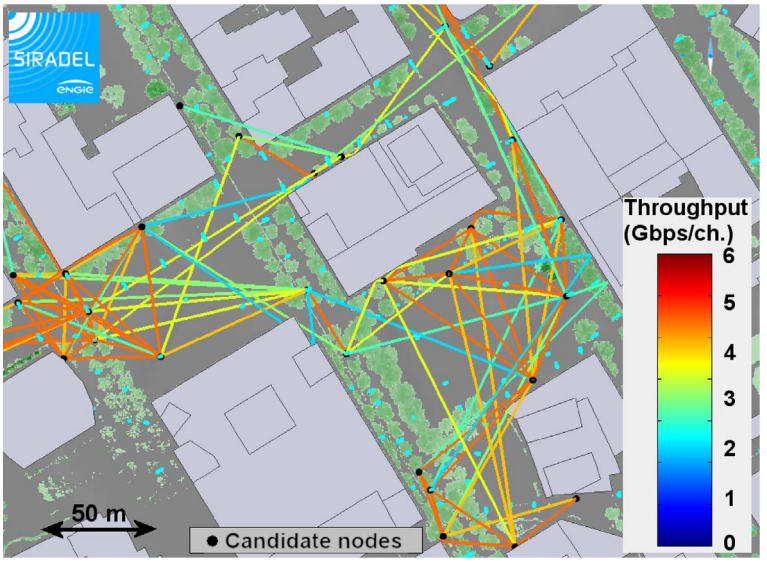

Figure 2. Mesh links in the outdoor backhaul network.

Table 1. System parameters

Parameter	Value
Frequency band	150 GHz
Channel BW	1 GHz
Tx power/ch	1 W
Tx antenna	25.0 dBi
Rx antenna	25.0 dBi
Th. noise floor	−84.0 dBm
Noise figure	10 dB
Rx sensibility	−98.2 dBm
Implementation loss	3.0 dB
Default rainfall rate	12.5 mm/h
Default PN level	Medium ($\sigma^2 = 10^{-2}$)
Adjustment factor	[−5;+5] dB

(Non-LoS or NLoS). A total of 585 links have sufficient SNR to establish a connection if antennas at both ends are perfectly aligned on the strongest propagation path. Figure 2 shows the simulated connections with their achievable throughput in one part of the study area; maximum throughput can be reached in clear LoS, while the vegetation significantly degrades the performance. We note that a few connections are allowed in building shadowed area due to indirect paths. Figure 3 zooms on some particular links and displays the main propagation paths, either line-of-sight or reflected along a trajectory out of any tree's obstruction.

Figure 4 gives statistics on the achievable throughput versus the distance between antennas, and for two different situations: (1) in case of LoS/OLoS visibility; (2) in case of a NLoS building obstruction. In first case, 98% links with range below 25 m reach a peak throughput greater than 4 Gbps/ch; the percentage drops to 81% and 52% for respectively the ranges]25;50] and]50;75] m, due to more likely and longer obstructions. It further decreases below 35% when the range is longer than 75 m. This result demonstrates that sub-THz hops longer than 75 m can provide

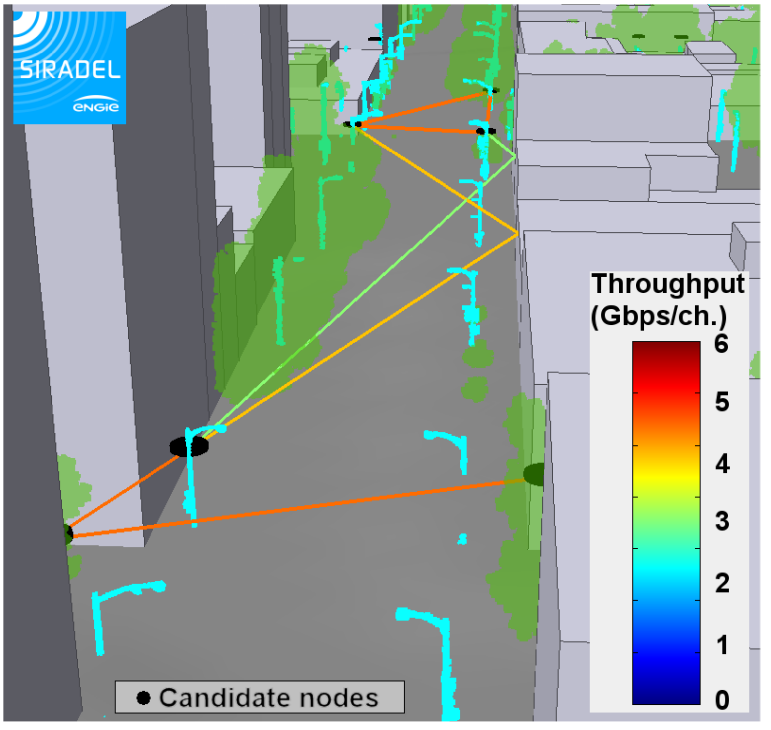

Figure 3. Direct and indirect connections.

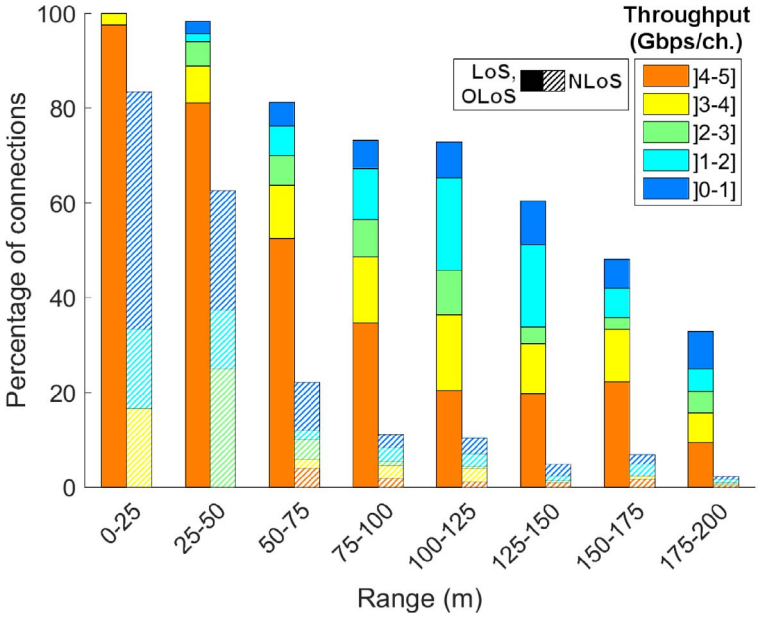

Figure 4. Percentage of links reaching a given throughput versus distance.

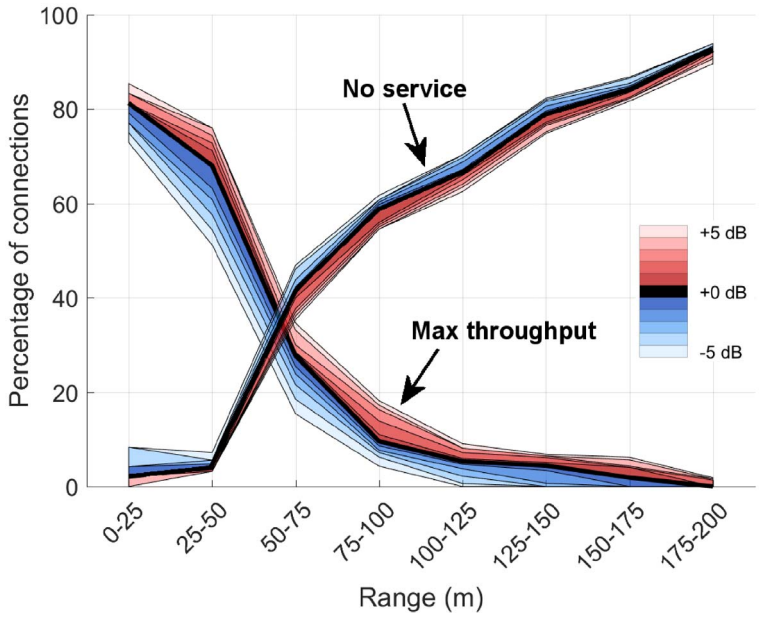

Figure 5. Percentage of links reaching a given throughput versus link budget gain.

more than 4 Gbps/ch, but need to be carefully chosen, based on an accurate knowledge of the environment. Figure 4 also gives the statistics for the Non-LoS links, and shows that indirect propagation paths can sometimes lead to high-throughput links, in particular for ranges below 75 m, which may be very useful for creating a link between orthogonal streets or as a backup connection. Finally, in the last 175–200 m range, the performance is strongly degraded for most of the predicted links; high-throughput connection is hardly possible.

The sensitivity of those results to the considered link budget parameters is illustrated in Figure 5, where the percentage of connections is plotted as a function of the distance and an additional gain in range [−5;+5] dB. A 4 dB adjustment in the link budget leads to 100% connection in the]0–25] m range, while 8% links in same range are losing connection with −5 dB adjustment. Besides, the [−5;+5] dB gain converts into maximum 25% variation in the high-throughput connection rate, as observed in the]25–50] m range.

Figure 6 indicates how many different propagation paths can be used by a node-to-node link in order to get connected, assuming the system is able to automatically align the Tx/Rx antenna beam towards the right departure/arrival directions. This result was computed from all links in range 0–200 m, whatever the visibility situation, but with a non-zero data rate. About 50% of those links do have a single connection path (due to the propagation channel sparsity), while respectively 30% and 10% of the links benefit from 2 or 3 possible connections paths. This number is actually a kind of diversity indicator. Depending on the communication system, the available diversity may be exploited in different ways, either for overcoming an obstruction on the dominant path, or optimizing the routing and inter-link interference, or transmitting several data streams on separated beams. We imagine the links with more than one possible connection path are better candidates when designing a network.

Finally, we have studied the impact of the rainfall rate on the link performance. Previous results were obtained for a rate of 12.5 mm/h, which is exceeded for approximately 0.1% of the time over a year. The same simulation was run for a clear weather and a 30 mm/h rate (0.01% of the time). The resulting throughput statistics are plotted as a function of the distance in Figure 7,

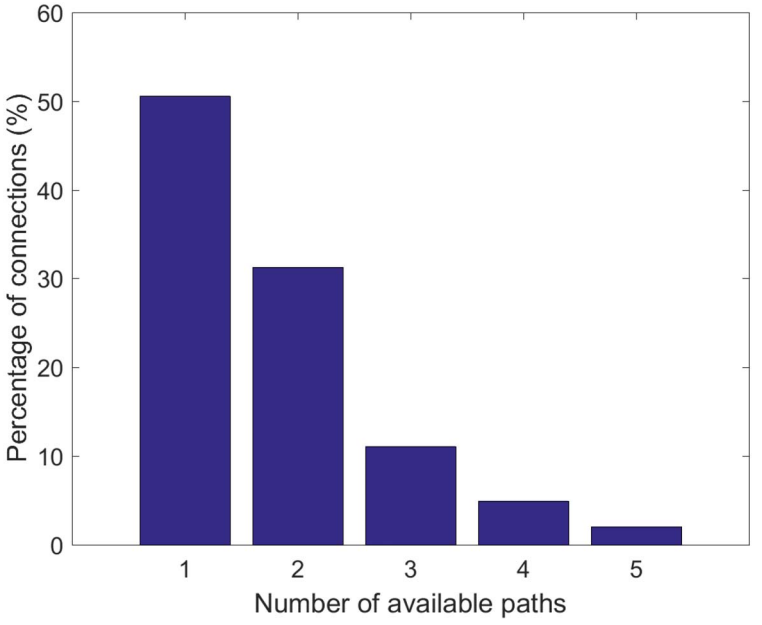

Figure 6. Statistics on the path diversity.

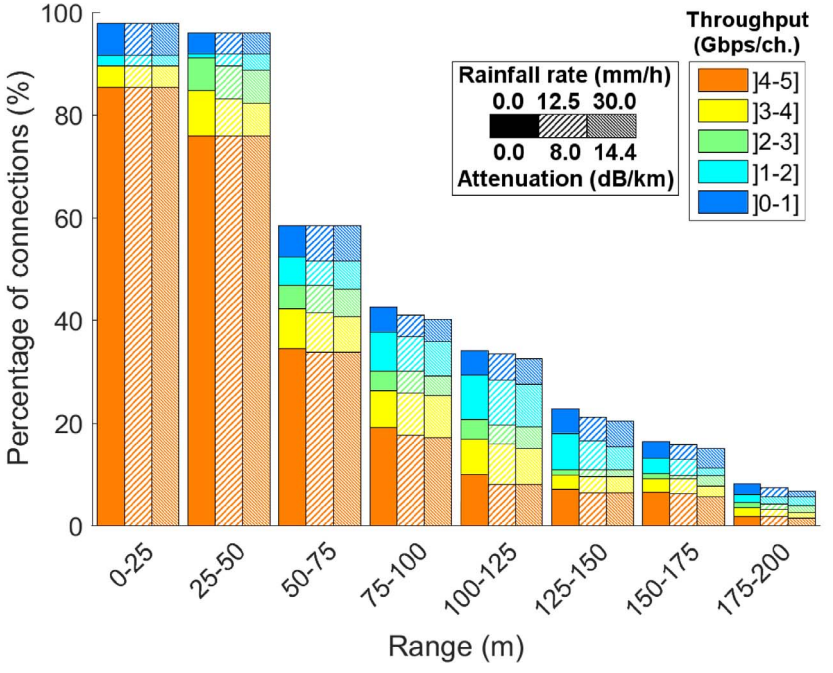

Figure 7. Impact of the rainfall rate on the achieved throughput.

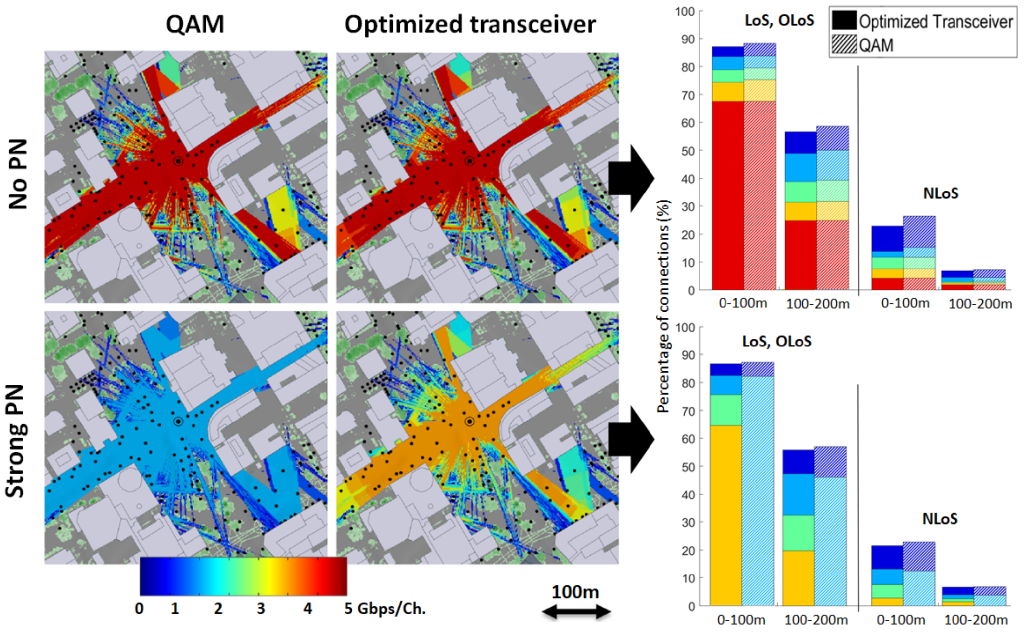

Figure 8. Performance for different PN levels and modulation schemes.

and compared. The different visibility conditions are not distinguished here (contrary to Figure 4) in order to make the illustration more compact. We observe the rainfall rate has no impact on the achievable throughput at ranges below 25 m, which is normal as the attenuation is proportional to the distance. Throughput degradation increases with the range, as expected, but it remains small. When assessing the link performance at such ranges below 200 m, the rain attenuation may be considered, but is obviously not a dominant factor. Precise knowledge of the geographical environment, presence of trees, or antenna misalignment issues, are more critical aspects.

4.3. *Impact of the phase noise level*

The phase noise (PN) level at the receiver might strongly affect the sub-THz backhaul link performance, and the modulation scheme must be appropriately selected depending on its robustness against PN impairments. Those considerations are illustrated in Figure 8, where coverage maps and throughput statistics are obtained with either no PN or strong PN ($\sigma_p^2 = 10^{-1}$), based on the traditional QAM or proposed P-QAM (named as the "optimized transceiver" in the figure). The coverage maps have been computed from a central transmitter node to any surrounding receiver pixel at 8 m above the ground (remark the lampposts i.e. candidate node positions are represented by black circles). And the throughput statistics were simulated from the same links as presented above in the article. The QAM does slightly overperform the P-QAM modulation in absence of any PN, with 2% more connected links in average. Same kind of improvement is observed under strong PN conditions, but then, the achievable throughput is limited below 2 Gbps/ch, while 64% of the LoS or obstructed-LoS links at ranges up to 100 m can still reach between 3 and 4 Gbps/ch thanks to the P-QAM optimization.

5. Conclusion

The presented simulation studies demonstrate the feasibility of sub-THz mesh backhaul networks, using a PN-robust modulation scheme, and considering real propagation constraints. This study shows the potential of the sub-THz technology to reach multi Gbps link in outdoor in-street typical scenarios, even in presence of strong phase noise. It is also observed that 50% of connected links have some multi-path diversity, which may be used for improving the capacity or protection of the network. The rainfall attenuation is found to have limited impact when radio links have a range inferior to 200 m. And finally, the simulation illustrates the benefit of the P-QAM modulation, which permits a large amount of links to reach a throughput greater than 3 Gbps/1 GHz channel in presence of strong PN impairments.

This work does continue today, with objective to demonstrate, dimension and assess future sub-THz mesh backhaul infrastructures.

Acknowledgment

The research leading to these results received funding from the French National Research Agency (ANR-17-CE25-0013) within the frame of the project BRAVE.

References

[1] 6G Research Vision 1, *Key drivers and research challenges for 6G ubiquitous wireless intelligence*, 6G Flagship, University of Oulu, Finland, 2019, White paper, http://jultika.oulu.fi/files/isbn9789526223544.pdf.

[2] Y. Corre, G. Gougeon, J.-B. Doré, S. Bicais, B. Miscopein, M. Saad, J. Palicot, F. Bader, E. Faussurier, "Sub-THz spectrum as enabler for 6G wireless communications up to 1 Tbit/s", 2019, 1st 6G Wireless Summit, Levi, Finland, https://hal.archives-ouvertes.fr/hal-01993187/document.

[3] S. L. H. Nguyen, J. Järveläinen, A. Karttunen, K. Haneda, J. Putkonen, "Comparing radio propagation channels between 28 and 140 GHz bands in a shopping mall", in *12th European Conference on Antennas and Propagation (EuCAP 2018), London, UK*, IEEE, 2018, p. 1-5.

[4] L. Pometcu, R. D'Errico, "Channel model characteristics in D-band for NLOS indoor scenarios", in *2019 13th European Conference on Antennas and Propagation (EuCAP), Krakow, Poland*, 2019, p. 1-4.

[5] J. M. Eckhardt, T. Doeker, S. Rey, T. Kürner, "Measurements in a real data center at 300 GHz and recent results", in *2019 13th European Conference on Antennas and Propagation (EuCAP), Krakow, Poland*, IEEE, 2019, p. 1-5.

[6] Y. Xing, T. S. Rappaport, "Propagation measurement system and approach at 140 GHz—moving to 6G and above 100 GHz", in *2018 IEEE Global Communications Conference (GLOBECOM), Abu Dhabi, United Arab Emirates*, IEEE, 2018, p. 1-6.

[7] G. Gougeon, Y. Corre, M. Z. Aslam, "Ray-based deterministic channel modelling for sub-THz band", in *2019 IEEE 30th International Symposium on Personal, Indoor and Mobile Radio Communications (PIMRC Workshops), Istanbul, Turkey*, IEEE, 2019, p. 1-6.

[8] M. R. Khanzadi, D. Kuylenstierna, A. Panahi, T. Eriksson, H. Zirath, "Calculation of the performance of communication systems from measured oscillator phase noise", *IEEE Trans. Circuits Syst. I Regul. Pap.* **61** (2014), no. 5, p. 1553-1565.

[9] S. Bicaïs, J.-B. Doré, "Phase noise model selection for sub-THz communications", in *2019 IEEE Global Communications Conference (GLOBECOM), Waikoloa, HI, USA*, IEEE, 2019, p. 1-6.

[10] R. Krishnan, A. Graell i Amat, T. Eriksson, G. Colavolpe, "Constellation optimization in the presence of strong phase noise", *IEEE Trans. Commun.* **61** (2013), no. 12, p. 5056-5066.

[11] S. Bicaïs, J.-B. Doré, J.-L. Gonzalez Jimenez, "On the optimum demodulation in the presence of Gaussian phase noise", in *2018 25th International Conference on Telecommunications (ICT), Saint-Malo, France*, IEEE, 2018, p. 269-273.

[12] S. Bicaïs, J.-B. Doré, "Design of digital communications for strong phase noise channels", *IEEE Open J. Veh. Technol.* **1** (2020), p. 227-243.

[13] M. Z. Aslam, Y. Corre, J. Belschner, G. S. Arockiaraj, M. Jäger, "Analysis of 60-GHz in-street backhaul channel measurements and LiDAR ray-based simulations", in *2020 14th European Conference on Antennas and Propagation (EuCAP), Copenhagen, Denmark*, IEEE, 2020, p. 1-5.

[14] UIT-R Radiocommunication Sector of ITU, “Propagation data and prediction methods for the planning of indoor radiocommunication systems and radio local area networks in the frequency range 300 MHz to 100 GHz”, July 2017, published in the *P Series Radiowave propagation*, https://www.itu.int/rec/R-REC-P.1238-9-201706-S/en.

[15] UIT-R Radiocommunication Sector of ITU, “Effects of building materials and structures on radiowave propagation above about 100 MHz”, Tech. Report ITU-R P2040-1, International Telecommunication Union, June 2015, published in the *P Series Radiowave propagation*, https://www.itu.int/dms_pubrec/itu-r/rec/p/R-REC-P.2040-1-201507-I!!PDF-E.pdf.

Comptes Rendus
Physique
2021, 22, nº S1, p. 47-52
https://doi.org/10.5802/crphys.62

URSI-France 2020 Workshop / *Journées URSI-France 2020*

Multi-beam modulated metasurface antenna for 5G backhaul applications at K-band

Jorge Ruiz-García *, [a], **Marco Faenzi** [a], **Adham Mahmoud** [a], **Mauro Ettorre** [a], **Patrick Potier** [b], **Philippe Pouliguen** [c], **Ronan Sauleau** [a] **and David González-Ovejero** [a]

[a] Univ. Rennes, CNRS, IETR - UMR 6164, F-35000, Rennes, France

[b] Direction Générale de l'Armement, 35174 Bruz, France

[c] Direction Générale de l'Armement, Agence de l'innovation de défense, 75509 Paris, France

E-mails: jorge.ruiz@univ-rennes1.fr (J. Ruiz-García), faenzi@diism.unisi.it (M. Faenzi), adham.mahmoud@univ-rennes1.fr (A. Mahmoud), mauro.ettorre@univ-rennes1.fr (M. Ettorre), patrick.potier@dga.defense.gouv.fr (P. Potier), philippe.pouliguen@dga.defense.gouv.fr (P. Pouliguen), Ronan.Sauleau@univ-rennes1.fr (R. Sauleau), david.gonzalez-ovejero@univ-rennes1.fr (D. González-Ovejero)

Abstract. We explore the use of a new modulated metasurface (MTS) antenna topology as solution for wireless backhaul at K band. The proposed structure is composed of a quasi-optical beamformer, which feeds the modulated MTS radiating aperture. These two elements are vertically stacked in a two-layer pillbox architecture to produce a very compact antenna. Furthermore, our design is able to provide several beams at different pointing angles and, hence, it offers the possibility of discrete beam steering by beam switching. The employment of a modulated MTS and the compactness given by the pillbox approach lead to a high-gain and low-profile antenna that could be an appealing solution for mobile backhaul networks.

Keywords. Metasurface antennas, Low profile, High gain, 5G, Backhaul, K-band, Leaky-wave antennas.

Available online 6th May 2021

1. Introduction

Microwaves and millimeter waves frequencies are among the frequency bands allocated for small-cell backhaul in 5G networks [1]. The use of metasurfaces (MTSs) for 5G systems has been studied and proved to be extremely useful in the aforementioned frequency ranges. Indeed, some antenna prototypes based on MTSs have already been developed with the aim of satisfying the needs of the new generation of mobile networks [2, 3]. Modulated MTS antennas, which were initially developed for satellite communications, are a special category of MTS antennas [4]. The

* Corresponding author.

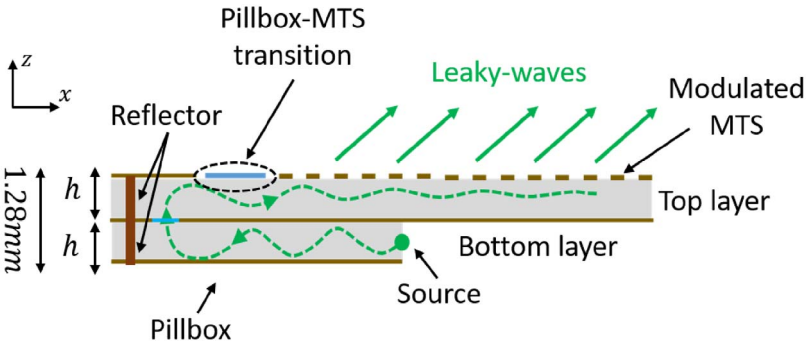

Figure 1. Side view of the pillbox fed MTS antenna.

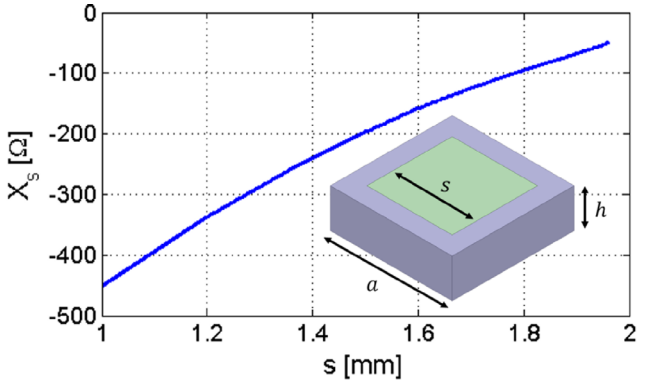

Figure 2. Unit-cell with square metallic patch and curve representing $X_s(s)$ for different patch sizes.

low profile, low cost and reduced power consumption of this kind of structures, along with the adaptability of the design process to different frequencies, make them a very attractive solution.

A MTS is generally formed by sub-wavelength elements arranged on a periodic lattice and either printed on a grounded dielectric slab or grown on a metallic base-plate. By changing the geometry of these constitutive elements in the lattice unit-cell, one can exert a high degree of control on the aperture fields [5–7]. The MTS layer can be modeled as a continuous impedance boundary condition (IBC) due to the small size of the elements compared to the wavelength. In modulated MTS antennas, a surface wave (SW) is excited on the aperture and gradually transformed into a leaky-wave owing to its interaction with the periodically modulated IBC, which results in a radiated beam [8]. By tuning the properties of the modulation one can control the attributes of the beam, such as the pointing angle, shape, and polarization.

This paper presents a modulated MTS antenna operating at K-band with multibeam performance. The system is based on a pillbox quasi-optical beamformer [9], which essentially transforms the cylindrical wave propagating on the pillbox's lower layer into a plane wave in the upper layer. By adding a modulated MTS on the top layer (Figure 1), one obtains a compact antenna. A pillbox-fed modulated MTS antenna at X-band was described in [10]. As mentioned before, the entire design process can be adapted for other frequency bands by properly modifying the material, the beamformer, and the MTS elements dimensions. Thus, in this work, we use a strategy similar to that described in [10] to design an antenna operating at $f_o = 20.7$ GHz.

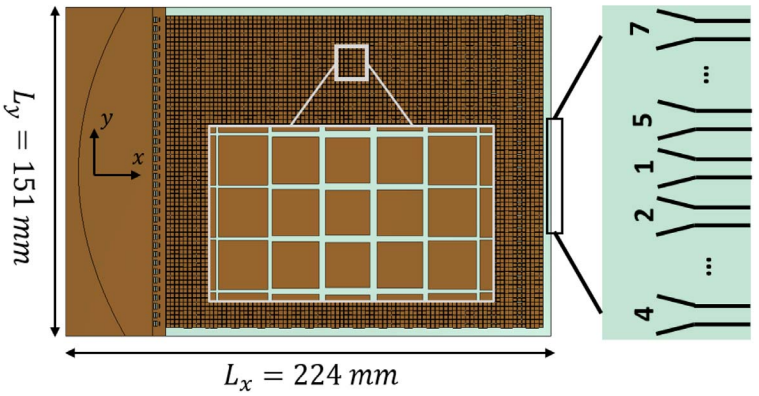

Figure 3. Top view of MTS antenna. Disposition of patches and ports in the pillbox beamformer.

2. Design of a multi-beam modulated metasurface antenna

In the following, we will refer to the Cartesian reference system (x, y, z) shown in Figure 1. The IBC used to model our MTS consists in a sheet transition [11, 12], penetrable [13] or transparent impedance [14, 15] $Z_s = \mathrm{j}X_s$ which lies on top of a grounded dielectric slab. This structure supports the propagation of a TM surface wave. In order to get the desired radiation effect, the sheet transition impedance is modulated along x-direction as

$$X_s(x) = X_{\mathrm{av}}(1 + M(x)\cos(2\pi x/p)), \tag{1}$$

where X_{av} is the average reactance, $M(x)$ is the modulation index ($0 \leq M(x) \leq 1$) and p is the period. The chosen material is Rogers RO3006 ($\varepsilon_r = 6.15$, $\tan\delta = 0.002$) with thickness $h = 0.64$ mm. In order to implement (1), we use square metallic patches whose size changes according to the spatial variation of $X_s(x)$. To that end, we first build a database that relates the patch dimensions to the sheet transition IBC values. Taking a unit-cell (a single MTS element) of side a on a substrate of thickness h, and assuming it inside a regular lattice to preserve the local periodicity principle, one can vary progressively the metallic patch size s and extract the equivalent sheet impedance Z_s. Figure 2 shows the curve that relates both parameters as well as an inset with the geometry of the unit-cell. The MTS element has a constant size $a = \lambda_0/7$, which makes it small compared to the SW wavelength, as indicated in Section 1. Once we have characterized the unit-cell, the next design step consists in retrieving the square patch dimensions that better match the ideal values in (1) to obtain our modulated MTS. The latter is placed then on the beamfomer top layer to get the final structure depicted in Figure 3.

In addition, it is important to note that the use of a pillbox allows one to place several sources (here, H-plane horns) in the bottom layer. These horns are arranged at the focal plane of the pillbox's reflector (Figure 3) and each one provides a beam pointing at a different direction. Indeed, when the source position is shifted in the focal plane (along y-direction), the direction of propagation of the resulting plane-wave changes. As a result, the placement of N ports originates up to N beams at different pointing angles. This feature will be illustrated in the next section. Obviously, the number of sources is limited by the pillbox dimension, the horn size, and the HPBW of the radiated beams. The antenna dimensions are sketched in Figures 1 and 3, from where we emphasize a very low profile, with a total thickness of 1.28 mm.

The main advantage of operating at a higher frequency with respect to the X-band model in [10] is the reduction of the antenna dimensions. First, for the require bandwidth, it is possible

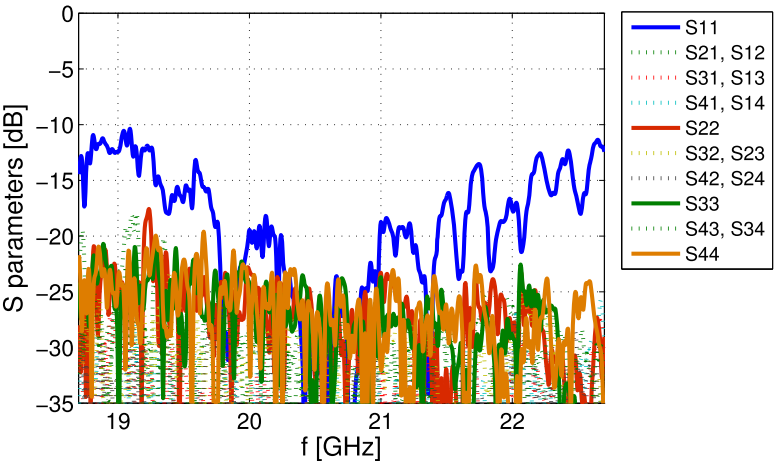

Figure 4. S-parameters for central and side ports, remaining ports behave as their symmetric ones.

to employ a thinner substrate that keeps providing the needed impedance range (Figure 2), which enforces the low-profile faculty of the system. The total radiating aperture size is also decreased, going up to almost a 50% smaller area than that in the X-band design. Another important aspect is the diminution of the feeding horn width, since the cut-off frequency is now larger. This allows one to set more sources along the pillbox focal plane and, hence, the number of beams on the scanning region is increased. The latter point is commented and exploited in Section 3.

In order to overcome the losses growth due to the frequency rise, the length of the lower layer is shortened (Figure 1). This is traduced into a minimization of the pillbox focal distance, while ensuring the required performance for the side lobe level (SLL ≤ -15 dB) and the beam-width at -3 dB (HPBW = 5°). Such a modification is realized by adjusting the horn dimensions and the pillbox reflector diameter.

The proposed design is a good alternative to phased array antennas [16, 17]. In fact, the absence of phase-shifters makes our MTS antenna simpler, cheaper and less power-consuming. Furthermore, the structure can be fabricated using PCB technology, which facilitates the manufacturing process and reduces the cost.

3. Simulation results

For the design at hand, we implement (1) to obtain a beam at $\theta_0 = 15°$ for normal incidence (port 1, $\phi_0 = 0°$). The employed modulation parameters are $p = 11.3$ mm, $X_{\text{av}} = -0.24\eta_0$ (where η_0 is the free-space impedance), and M varying with x to optimize the attenuation of the aperture fields and, therefore, enhance the aperture efficiency of the antenna [18]. Switching between the $N = 7$ ports implies the modification of both θ_0 and ϕ_0. The simulated S-parameters of the horns are shown in Figure 4, revealing a bandwidth of 20% and a very good isolation between ports.

Figure 5 presents the radiated beams for each source at f_o. The obtained angular coverage is displayed in Figure 5a, where the direction of the beam is given in (θ, ϕ) coordinates. Next, we represent in Figure 5b the radiation pattern in elevation at the E-plane for every port. The patterns are plotted by cutting every 3D beam at the angle $\phi = \phi_0$, where ϕ_0 is the azimuth angle of maximum gain for each source. The maximum realized gain at f_o is $G = 27.1$ dB for port 1 and the beam-switching losses are up to 2.5 dB (realized gain difference between port 1 and ports 4, 7). We note that the generated beams own the property of frequency scanning in θ. Thus, it would

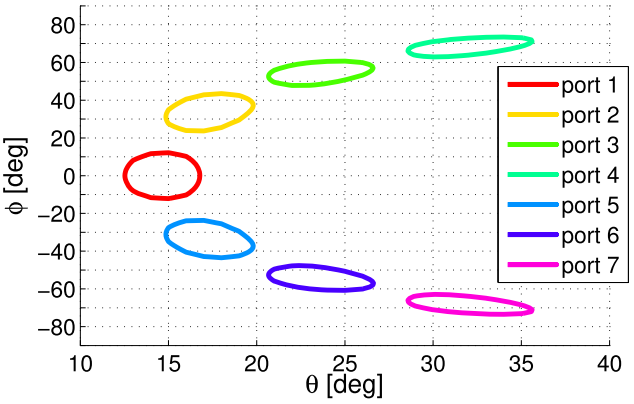

(a) -3dB contours of radiated beams

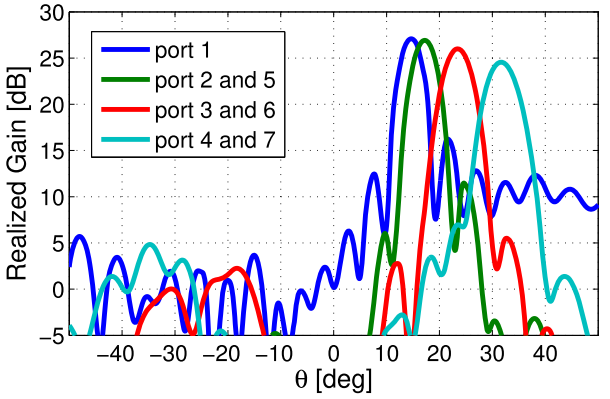

(b) E-plane radiation patterns at fixed $\phi = \phi_0$ of each port

Figure 5. (a) Radiation performance in (θ, ϕ) plane, and (b) realized gain at the E-plane cut for each horn.

be possible to operate at other frequencies around f_o within the bandwidth shown in Figure 4, modifying then the individual beam directions and the angular coverage.

The described model is under fabrication and a measuring experiment is planned. Besides, the scanning area can be extended to the region $\theta < 0°$ (Figure 5a) by arranging an additional reflector and horns opposed in the x-axis to the existing ones [19].

4. Conclusion

We presented the design and numerical results of a compact modulated MTS antenna at 20.7 GHz. The radiating aperture consists of metallic patches whose size is modified to produce an equivalent modulated impedance. The MTS antenna is fed by a plane SW, which is obtained by means of a quasi-optical beamformer in a pillbox architecture. Moreover, one can change the propagation direction of this SW by exciting different ports in the pillbox focal plane. The proposed antenna topology is able to generate high-gain beams at different pointing angles, while providing a good scanning range in θ and a wide angular coverage in ϕ. The extremely thin profile of the structure ($h_{\text{total}} = 1.28$ mm), the high-gain behavior, and the multi-beam capability make this antenna a suitable candidate for backhaul applications. Last but not least, this flat

aperture antenna can be easily integrated with a low visual impact on smart urban furniture, buildings, homes, and offices.

Acknowledgements

This publication was supported by the European Union through the European Regional Development Fund (ERDF), and by the French Region of Brittany, Ministry of Higher Education and Research, Rennes Métropole and Conseil Départemental 35, through the CPER Project STIC & Ondes. It has also been supported by the Direction Générale de l'Armement (DGA) and by Britanny Region under ARED program.

References

[1] M. M. Ahamed, S. Faruque, "5G backhaul: requirements, challenges, and emerging technologies", in *Broadband Communications Networks* (A. Haidine, A. Aqqal, eds.), IntechOpen, Rijeka, 2018.

[2] S. Gupta, Z. Briqech, A. R. Sebak, T. Ahmed Denidni, "Mutual-coupling reduction using metasurface corrugations for 28 GHz MIMO applications", *IEEE Antennas Wirel. Propag. Lett.* **16** (2017), p. 2763-2766.

[3] T. Li, Z. N. Chen, "Metasurface-based shared-aperture 5G *S*-/*K*-band antenna using characteristic mode analysis", *IEEE Trans. Antennas Propag.* **66** (2018), no. 12, p. 6742-6750.

[4] M. Faenzi *et al.*, "Metasurface antennas: new models, applications and realizations", *Sci. Rep.* **9** (2019), article no. 10178.

[5] S. Maci, G. Minatti, M. Casaletti, M. Bosiljevac, "Metasurfing: addressing waves on impenetrable metasurfaces", *IEEE Antennas Wirel. Propag. Lett.* **10** (2011), p. 1499-1502.

[6] D. González-Ovejero, G. Minatti, G. Chattopadhyay, S. Maci, "Multibeam by metasurface antennas", *IEEE Trans. Antennas Propag.* **65** (2017), no. 6, p. 2923-2930.

[7] D. González-Ovejero, N. Chahat, R. Sauleau, G. Chattopadhyay, S. Maci, M. Ettorre, "Additive manufactured metal-only modulated metasurface antennas", *IEEE Trans. Antennas Propag.* **66** (2018), no. 11, p. 6106-6114.

[8] A. Oliner, A. Hessel, "Guided waves on sinusoidally-modulated reactance surfaces", *IRE Trans. Antennas Propag.* **7** (1959), no. 5, p. 201-208.

[9] M. Ettorre, R. Sauleau, L. Le Coq, "Multi-beam multi-layer leaky-wave SIW pillbox antenna for millimeter-wave applications", *IEEE Trans. Antennas Propag.* **59** (2011), no. 4, p. 1093-1100.

[10] J. Ruiz-García, D. González-Ovejero, M. Faenzi, A. Mahmoud, M. Ettorre, P. Potier, P. Pouliguen, R. Sauleau, "Quasi-optical excitation of modulated metasurface antennas", in *13th Int. Congress on Artificial Materials for Novel Wave Phenomena (Metamaterials)*, 2019, p. X-348-X-350.

[11] E. F. Kuester, M. Mohamed, M. Piket-May, C. Holloway, "Averaged transition conditions for electromagnetic fields at a metafilm", *IEEE Trans. Antennas Propag.* **51** (2003), no. 10, p. 2641-2651.

[12] A. M. Patel, A. Grbic, "Effective surface impedance of a printed-circuit tensor impedance surface (PCTIS)", *IEEE Trans. Microw. Theory Tech.* **61** (2013), no. 4, p. 1403-1413.

[13] E. Bleszynski, M. Bleszynski, T. Jaroszewicz, "Surface-integral equations for electromagnetic scattering from impenetrable and penetrable sheets", *IEEE Antennas Propag. Mag.* **35** (1993), no. 6, p. 14-25.

[14] D. González-Ovejero, S. Maci, "Gaussian ring basis functions for the analysis of modulated metasurface antennas", *IEEE Trans. Antennas Propag.* **63** (2015), no. 9, p. 3982-3993.

[15] G. Minatti, F. Caminita, E. Martini, M. Sabbadini, S. Maci, "Synthesis of modulated-metasurface antennas with amplitude, phase, and polarization control", *IEEE Trans. Antennas Propag.* **64** (2016), no. 9, p. 3907-3919.

[16] L. Verma, M. Fakharzadeh, S. Choi, "Backhaul need for speed: 60 GHz is the solution", *IEEE Wirel. Commun.* **22** (2015), no. 6, p. 114-121.

[17] A. Valdes-Garcia, B. Sadhu, X. Gu, J. Plouchart, M. Yeck, D. Friedman, "Scaling millimeter-wave phased arrays: challenges and solutions", in *2018 IEEE BiCMOS and Compound Semiconductor Integrated Circuits and Technology Symposium (BCICTS)*, 2018, p. 80-84.

[18] D. R. Jackson, A. A. Oliner, "Leaky–wave antennas", in *Modern Antenna Handbook* (C. A. Balanis, ed.), Wiley, New Jersey, USA, 2007, p. 325-367.

[19] T. Potelon, M. Ettorre, L. Le Coq, T. Bateman, J. Francey, R. Sauleau, "Reconfigurable CTS antenna fully integrated in PCB technology for 5G backhaul applications", *IEEE Trans. Antennas Propag.* **67** (2019), no. 6, p. 3609-3618.

Comptes Rendus
Physique
2021, 22, nº S1, p. 53-71
https://doi.org/10.5802/crphys.68

URSI-France 2020 Workshop / *Journées URSI-France 2020*

Bandpass NGD function design for 5G microwave signal delay synchronization application

Sébastien Lalléchère *, [a], **Lala Rajaoarisoa** [b], **Laurent Clavier** [b], **Raul Sanchez Galan** [c] and **Blaise Ravelo** [c]

[a] Université Clermont Auvergne, Institut Pascal, SIGMA Clermont, France

[b] IMT Lille Douai, Institut Mines-Télécom, Univ. Lille, Centre for Digital Systems, F-59000 Lille, France

[c] Nanjing University of Information Science & Technology (NUIST), Nanjing, Jiangsu 210044, China

E-mails: sebastien.lallechere@uca.fr (S. Lalléchère), lala.rajaoarisoa@imt-lille-douai.fr (L. Rajaoarisoa), laurent.clavier@imt-lille-douai.fr (L. Clavier), r.galan@reading.ac.uk (R. S. Galan), blaise.ravelo@nuist.edu.cn (B. Ravelo)

Abstract. This paper introduces a design method of simple bandpass (BP) negative group delay (NGD) topology. The fundamental specifications of BP NGD function are defined. The NGD passive topology consists of parallel resistance associated with an open-ended microstrip stub. The NGD properties and characterization with respect to the constituting stub parameters are established. The validations are performed with theoretical calculated and simulated GD, transmission and reflection coefficients. The BP NGD circuit can be useful for the improvement of phase linearity and GD equalization of future 5G microwave devices.

Keywords. Negative group delay (NGD), Bandpass (BP) NGD function, Design method, Microstrip 5G circuit, NGD analysis and synthesis.

Available online 6th May 2021

1. Introduction

The twenty-first century differs from the previous ones under the incessant increase of tremendous communications initially between mankind. Following the different socio-economic needs, the communications were extended between mankind-object and even object-object [1]. The modern communication system is expected to operate under the master word target wireless connection "anything, anywhere and anytime". The scenario of a future 5G smart city proposed by 5G IA shown in Figure 1 illustrates the necessity of connected infrastructure, things and people [1].

* Corresponding author.

Figure 1. Architecture and scenario of 5G infrastructure proposed by 5G IA [1] (Permission granted by 5G IA).

To set this 5G city, significant technological race on 5G architecture requiring a higher data rate and higher bandwidth is currently open between developed countries (US, China, EU, ...) [2]. 5G technological advancement is expected as a promising solution for future mobile communication [3]. However, the communication system using 5G wireless sensor networks (WSNs) may suffer from electromagnetic compatibility (EMC) issues, for example, due to the radio link signal interferences [4, 5], EMC and massive Internet of Things (IoT) [6].

Different challenging RF and microwave device designs have been made to be under the race for the future 5G infrastructure deployment. For example, to improve the performances of the transmitter (Tx) and receiver (Rx) circuits, a reconfigurable phased array was introduced for controlling 5G terminals [7]. High directive beam steering of adaptive antenna array plays an important role in the performance of such communication terminals [8].

An innovative solution of phased array design, using the unfamiliar negative group delay (NGD) function, enabling beam squint elimination was proposed [9–12]. Such a phased array design method is fundamentally based on the use of NGD based non-Foster elements [13–15]. The NGD non-Foster networks were initially designed with lossy circuits which limit their fields of potential applications [13, 14]. Then, active circuit based non-Foster elements were also designed [15]. In addition to the phased array networks, the NGD circuits were also used for the design of oscillators, filters [16] and phase shifter [17] for RF and microwave communication systems. Moreover, the NGD function was also used for the design of diverse devices as an absorptive band-stop filter [18] and equalization of bandpass filters [19]. One of the most specific applications of NGD function concerns the signal delay compensation [20] and propagation delay synchronisation [21]. This later application is implemented with the reduction of the propagation delay based on the NGD function [21]. Despite these tentative applications, so far, the familiarity of non-specialist RF and microwave engineers to the NGD function necessitates further research works. For this reason, the present paper is focused on the design method of bandpass NGD circuit for 5G frequency band. Before the elaboration of the circuit design, it is worth noticing a brief description of microwave NGD state of the art.

The NGD microwave existence was one of the curious debates between research design engineers in the 2000s. Different feasibility of NGD effect generations [22–33] was investigated. The NGD effect was experimented with signal interference techniques [22]. Then, the NGD function was also designed with a microwave transversal filter approach [23]. The democratization of the NGD function was also be proven with its different aspects as the possibility of dual-band design [24]. The most promising NGD applications were encouraged by the number of research works on the compact and miniaturized microstrip transmission line (TL) circuit designs per-

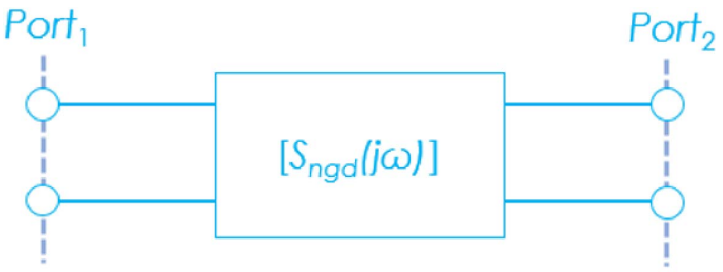

Figure 2. Two-port black box microwave system.

formed in the last decade [25–30].

Because of the unfamiliarity of RF/microwave design engineers and also research communities to this fascinating function, it would be necessary to highlight the NGD function meaning. In this way, the analogy between the filter and NGD functions was initiated in [31, 32]. The concept of bandpass (BP) NGD function was introduced as a function of the sign of the transmission coefficient group delay (GD) [32]. Because of the open-stub based NGD topology simplicity, a design of a BP NGD cell with 5G-centre frequency was recently proposed during URSI France scientific days 2020 [33]. This paper is an extension of the research work published in [33] with further detailed description of the BP NGD specifications, theoretical design and potential applications.

2. Preliminary definition of bandpass NGD function

A preliminary definition of the unfamiliar BP NGD function is introduced in this section. After the theoretical expression recall, the specification parameters will be defined. The key parameters required for the NGD study will be pedagogically explored.

2.1. *S-matrix black box*

First and foremost, acting as a two-port system, the NGD circuit investigated in the present paper can be generalized by the black box system represented in Figure 2. By denoting the complex angular frequency variable, $s = \mathrm{j}\omega$, this system can be analytically modelled by the 2-D S-matrix:

$$[S_{\mathrm{NGD}}(\mathrm{j}\omega)] = \begin{bmatrix} S_{11}(\mathrm{j}\omega) & S_{12}(\mathrm{j}\omega) \\ S_{21}(\mathrm{j}\omega) & S_{22}(\mathrm{j}\omega) \end{bmatrix}. \tag{1}$$

In contrast to the classical RF and microwave circuits, the NGD study requires more intensive analysis of frequency responses of GD calculated from the S-matrix introduced in (1).

2.2. *Magnitudes of S-parameters*

Before the NGD analytical definition, it is worth noting that the present paper is essentially focused on passive circuits. Therefore, the performance assessment of BP NGD circuit must include:

- The insertion loss or gain related to the transmission coefficient magnitude which should be lower than an expected value, $a < 1$:

$$S_{21}(\omega) = |S_{21}(\mathrm{j}\omega)| \geq a \tag{2}$$

- The input and output reflection losses related to the reflection coefficient magnitudes which must be lower than an expected matching value, $b < 1$:

$$S_{11}(\omega) = |S_{11}(\mathrm{j}\omega)| \leq b \tag{3}$$

$$S_{22}(\omega) = |S_{22}(\mathrm{j}\omega)| \leq b. \tag{4}$$

2.3. *Transmission GD definition*

By its definition, the NGD study is fundamentally dependent on the GD analytical expression. For this reason, it would be important to recall the mathematical definition of this key parameter. It is derived from the phase of the transmission coefficient of S-matrix introduced in (1). In other words, it is given by:

$$\varphi(\omega) = \arg[S_{21}(\mathrm{j}\omega)]. \tag{5}$$

The analytical model of the associated GD is defined by:

$$\mathrm{GD}(\omega) = \frac{-\partial\varphi(\omega)}{\partial\omega}. \tag{6}$$

2.4. *Graphical representation of BP NGD specifications*

The unfamiliar BP NGD function was inspired by BP filter response [31, 32]. However, it is important to note that the NGD function depends essentially on the sign of GD expressed in (6) but not the behaviour of the S_{21} magnitude. By taking:

$$\omega_{m=1,2} = 2\pi f_m \tag{7}$$

the type of NGD function depends on the frequency band position, $\omega_1 \leq \omega \leq \omega_2$, where we have:

$$\mathrm{GD}(\omega_1 \leq \omega \leq \omega_2) \leq 0. \tag{8}$$

Figure 3(a) illustrates an ideal GD response of BP NGD function. The main specifications can be defined:

- By taking a real positive delay, t, the GD value:

$$\mathrm{GD}(\omega_1 \leq \omega \leq \omega_2) = -t \tag{9}$$

- NGD bandwidth:

$$\Delta\omega = 2\pi\Delta f = \omega_2 - \omega_1 \tag{10}$$

- NGD centre frequency:

$$\Delta\omega_0 = 2\pi f_0 \in [\omega_1, \omega_2] \tag{11}$$

- As illustrated in Figure 3(b), through dB-value $-a_{\mathrm{dB}} = 20\log 10(a)$, the reflection coefficient:

$$S_{11}(\omega_1 \leq \omega \leq \omega_2) = a. \tag{12}$$

- And as explained in Figure 3(c), through dB-value $-b_{\mathrm{dB}} = 20\log 10(b)$, the transmission coefficient:

$$S_{21}(\omega_1 \leq \omega \leq \omega_2) = b. \tag{13}$$

3. Bandpass NGD theoretical investigation on open-ended passive topology

The present section describes the theoretical approach of the BP NGD circuit. The present study details essentially the analytical investigation reported in [33].

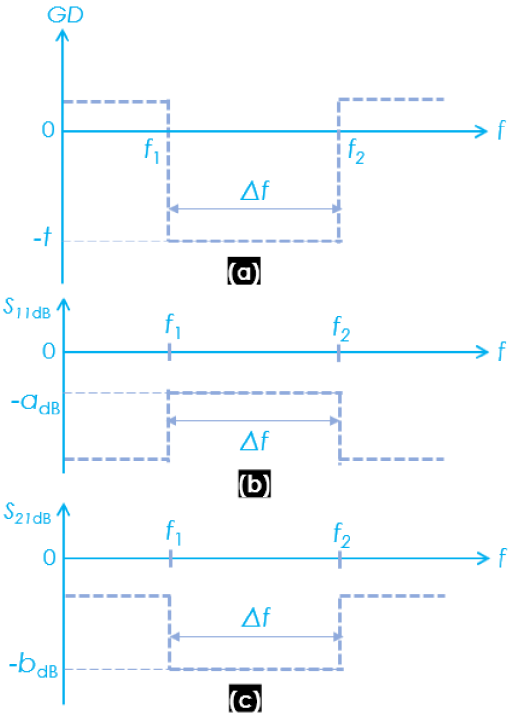

Figure 3. BP NGD function ideal specification: (a) GD, (b) S_{11} and (c) S_{21}.

3.1. *Topological description*

Figure 4 represents the TL based topology of NGD passive cell connected between node M and ground node [16]. This topology is assumed connected to terminal reference impedances, $R_0 = 50\ \Omega$ connected between nodes M_1M and MM_2. The circuit can be represented as a two-port system fed by voltage sources U_1 (left) and U_2 (right). It induces the input currents, I^1 and I^2. Meanwhile, the equivalent impedance, $[Z_{NGD}(j\omega)]$, is linked to the external voltage and current vectors by the matrix relation:

$$\begin{bmatrix} U_1(j\omega) \\ U_2(j\omega) \end{bmatrix} = [Z_{NGD}(j\omega)] \begin{bmatrix} I^1(j\omega) \\ I^2(j\omega) \end{bmatrix}. \tag{14}$$

The topology under study is essentially composed of a parallel resistance R ended by a lossless open-ended stub $TL(Z, \tau_0)$ which is defined by characteristic impedance Z and delay τ_0.

Acting as a lossless TL, the input impedance can be defined as [17]:

$$Z_{in}(j\omega) = R + \frac{Z}{j\tan(\omega\tau_0)} \tag{15}$$

Meanwhile, the equivalent impedance, $[Z_{NGD}(j\omega)]$, can be written as:

$$[Z_{NGD}(j\omega)] = \frac{\begin{bmatrix} 1 & 1 \\ 1 & 1 \end{bmatrix}}{Z_{in}(j\omega)}. \tag{16}$$

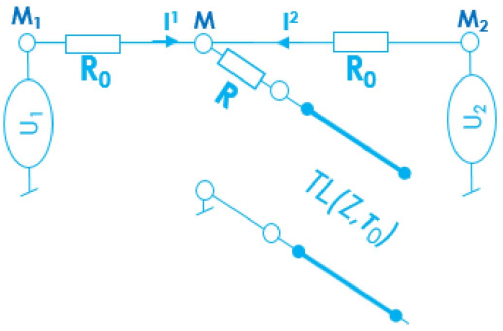

Figure 4. Open-ended stub based NGD passive circuit.

3.2. *S-matrix frequency response*

The equivalent S-matrix can be extracted from Z-to-S transform:

$$[S_{\mathrm{NGD}}(\mathrm{j}\omega)] = ([Z_{\mathrm{NGD}}(\mathrm{j}\omega)] - R_0[1_2]) \times ([Z_{\mathrm{NGD}}(\mathrm{j}\omega)] + R_0[1_2])^{-1} \tag{17}$$

where:

$$[1_2] = \begin{bmatrix} 1 & 0 \\ 0 & 1 \end{bmatrix}. \tag{18}$$

The analytical development of this matrix relationship enables us to determine the S-matrix of our circuit. Subsequently, we emphasize that the S-matrix must be symmetric and its elements must satisfy the relations:

$$S_{12}(\mathrm{j}\omega) = S_{21}(\mathrm{j}\omega) = \frac{2Z_{\mathrm{in}}(\mathrm{j}\omega)}{R_0 + 2Z_{\mathrm{in}}(\mathrm{j}\omega)} \tag{19}$$

$$S_{11}(\mathrm{j}\omega) = S_{22}(\mathrm{j}\omega) = \frac{-R_0}{R_0 + 2Z_{\mathrm{in}}(\mathrm{j}\omega)}. \tag{20}$$

It can be demonstrated that the reflection and transmission coefficient responses of the proposed topology can be written as:

$$S_{11}(\mathrm{j}\omega) = \frac{R_0 \tan(\omega\tau_0)}{2\mathrm{j}Z - (2R + R_0)\tan(\omega\tau_0)} \tag{21}$$

$$S_{21}(\mathrm{j}\omega) = \frac{2[\mathrm{j}Z - R\tan(\omega\tau_0)]}{2\mathrm{j}Z + (2R + R_0)\tan(\omega\tau_0)}. \tag{22}$$

The associated magnitudes are expressed as, respectively:

$$S_{11}(\omega) = |S_{11}(\mathrm{j}\omega)| = \frac{R_0|\tan(\omega\tau_0)|}{\sqrt{(2R + R_0)^2\tan^2(\omega\tau_0) + 4Z^2}} \tag{23}$$

$$S_{21}(\omega) = |S_{21}(\mathrm{j}\omega)| = \frac{2\sqrt{Z^2 + R^2\tan^2(\omega\tau_0)}}{\sqrt{(2R + R_0)^2\tan^2(\omega\tau_0) + 4Z^2}}. \tag{24}$$

3.3. *NGD analysis*

Before the NGD analysis, it is worth recalling the GD analytical expression. The mathematical condition between the NGD topology parameters is expressed. The analysis demonstrating why the proposed topology can be classified as a BP NGD function is presented.

3.3.1. *GD of the considered passive topology*

First, as a reminder to (5), the transmission phase associated to expression (21) is written as:

$$\varphi(\omega) = -\arctan\left[\frac{Z}{R\tan(\omega\tau_0)}\right] - \arctan\left[\frac{2Z}{(2R+R_0)\tan(\omega\tau_0)}\right]. \tag{25}$$

The GD of the open-ended stub cell introduced in Figure 4 can be derived from (6) and the previous transmission phase. As a matter of fact, we have the detailed analytical expression of the open-ended stub topology GD:

$$\mathrm{GD}(\omega) = \frac{R_0 Z\tau_0[1+\tan^2(\omega\tau_0)][2Z^2 - R(2R+R_0)\tan^2(\omega\tau_0)]}{[Z^2+R^2\tan^2(\omega\tau_0)][2Z^2+(2R+R_0)^2\tan^2(\omega\tau_0)]}. \tag{26}$$

3.3.2. *NGD existence condition*

The GD expressed in (25) satisfies the condition:

$$\mathrm{GD}(\omega) \leq 0 \tag{27}$$

Equivalently, this inequality can be expressed as:

$$2Z^2 - R(2R+R_0)\tan^2(\omega\tau_0) \leq 0. \tag{28}$$

In other words, this inequality can be transformed as:

$$\tan^2(\omega\tau_0) \geq \frac{2Z^2}{R(2R+R_0)} \Rightarrow \tan(\omega\tau_0) \geq \frac{Z\sqrt{2}}{\sqrt{R(2R+R_0)}}. \tag{29}$$

From the latter inequality, the NGD bandwidth is derived:

$$\Delta f = \left\{\frac{\omega_0}{\pi} - \frac{2}{\tau_0}\arctan\left[\frac{Z\sqrt{2}}{\sqrt{R(R_0+2R)}}\right]\right\}. \tag{30}$$

3.3.3. *Analysis at the particular frequency, $\omega = \omega_0$*

The NGD analysis consists in proving that the proposed passive topology is capable of operating as a BP NGD function. Doing this, we intuitively have the NGD centre frequency:

$$f_0 = \frac{\omega_0}{2\pi}. \tag{31}$$

Acting as quarter wave length TL, this characteristic frequency can be expressed as a function of the propagation delay:

$$f_0 = \frac{0.25}{\tau_0}. \tag{32}$$

At this particular frequency, it can be established that the S-parameters established in (22) and (23) become, respectively:

$$S_{11}(\omega_0) = |S_{11}(\mathrm{j}\omega_0)| = \frac{R_0}{2R+R_0} \tag{33}$$

$$S_{21}(\omega_0) = |S_{21}(\mathrm{j}\omega_0)| = \frac{2R}{2R+R_0}. \tag{34}$$

It means that the reflection coefficient is intrinsically linked to the transmission coefficient by the relationship:

$$S_{11}(\omega_0) = 1 - S_{21}(\omega_0). \tag{35}$$

Furthermore, the GD expressed in (26) is simplified as:

$$\mathrm{GD}(\omega_0) = \frac{-R_0 Z\tau_0}{R(R_0+2R)}. \tag{36}$$

3.4. *NGD design synthesis equations of the proposed open-ended stub topology in function of given specifications*

Similar to the classical filter or amplifier or other microwave circuits, the specifications of the BP NGD function introduced earlier in Figure 3 are necessary to design the unknown circuit (see Figure 4).

3.4.1. *Equation of TL delay*

The desired NGD centre frequency, f_0, is the main parameter to determine the propagation delay of TL constituting our BP NGD circuit introduced in Figure 4. The analytical equation can be transited from (32). Therefore, we have the synthesis equation:

$$\tau_0 = \frac{0.25}{f_0}. \tag{37}$$

3.4.2. *Equation of R*

To determine the resistor, R, of the open-ended stub topology introduced in Figure 4, we need the value of return loss, $a < 1$. Generally, to fulfil the matching expectation, $a = -10$ dB is considered for standard microwave circuits. Therefore, the unknown resistor can be obtained by solving the equation:

$$S_{11}(f_0) = a. \tag{38}$$

In this case, as predicted by (35), the transmission coefficient is systematically:

$$S_{21}(f_0) = 1 - a. \tag{39}$$

Emphatically, we can establish the synthesis equation:

$$R = \frac{0.5R_0(1-a)}{a}. \tag{40}$$

3.4.3. *Equation of TL characteristic impedance*

The design equation of the TL characteristic impedance, Z, can be established from the given propagation delay, which needs to be reduced from BP NGD circuit. We can denote for example this delay by the real positive, $t > 0$. The resolution of the following equation enables to determine the synthesis formula of this impedance:

$$\mathrm{GD}(f_0) = -t. \tag{41}$$

Accordingly, we can demonstrate from expression (36) that the characteristic impedance synthesis equation of NGD circuit introduced in Figure 4 is:

$$Z = \frac{0.5R_0(1-a)t}{a^2\tau_0}. \tag{42}$$

4. BP NGD validation results and delay reduction application principle

This section is focused on the validation of the previous BP NGD theory. Doing this, a proof of concept (POC) designed with microstrip circuit is introduced. The ideal circuit synthesis from previously established design formulas will be introduced. Then, the comparison between the ideal model and commercial tool simulation is discussed.

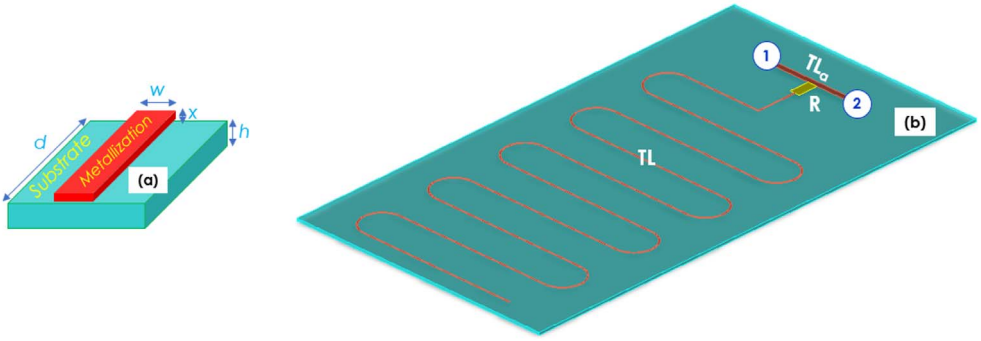

Figure 5. (a) Microstrip design and (b) NGD circuit POC 3D design.

Table 1. Specifications of the NGD microstrip circuit

Structure	Designation	Parameter	Value
Dielectric substrate	Kapton	—	—
	Relative permittivity	ε_r	3.3
	Loss tangent	$\tan(\delta)$	0.002
	Height	h	125 µm
Conductor metallization	Copper	—	—
	Conductivity	σ	58 MS/s
	Thickness	t	17 µm

4.1. *POC description*

As POC, microstrip circuits were designed and simulated to validate more concretely the previously developed BP NGD theory. The geometrical parameters of the microstrip structure is illustrated in Figure 5(a). The dielectric substrate is supposed characterized by thickness, h and the Copper-metallized conductor supposed is characterized by physical width w, length d and thickness x. Figure 5(b) shows the 3D design of the NGD circuit POC constituted by:

- Resistor, R,
- Terminated by an open-ended, TL(w,d) having physical width, w, and physical length, d, and,
- Access lines TL$_a(w_a,d_a)$ having physical width, w_a, and physical length, d_a.

The specifications of the Kapton substrate and metallization of the NGD circuit POC are indicated in Table 1.

4.2. *Discussion on the obtained results*

This subsection explores the validation results of the open-ended stub-based BP NGD theory. It is noteworthy that the analytical Matlab calculations of the BP NGD circuit ideal model were realized with:

- Reflection coefficient given in (22),
- Transmission coefficient carried out from (23),
- And GD from (25).

To validate the analytical calculated results, the POC circuit introduced in Figure 5(b) was simulated with the commercial tool ADS® from Keysight Technologies® schematic environment.

Table 2. BP NGD specifications to operate at 3.6 GHz

Designation	Name	Value
NGD centre frequency	f_0	3.6 GHz
Delay	t	0.34 ns
Reflection loss	$-a_{\mathrm{dB}}$	10 dB

Table 3. Calculated parameters for the ideal BP NGD circuit

Designation	Name	Value
Resistor	R	60 Ω
TL delay	τ_0	69 ps
TL characteristic impedance	Z	1 kΩ

Table 4. Specifications of the NGD microstrip circuit

Element	Designation	Name	Value
Stub TL	Width	w	62 µm
	Length	d	23.4 cm
Resistor	Resistor	R	60 Ω
Access line	Width	w_a	277 µm
	Length	d_a	2 mm

4.2.1. *3.6-GHz BP NGD POC*

Table 2 addresses the desired NGD specifications to design the 5G NGD POC with 3.6 GHz centre frequency. By using design (37), (40) and (42), we obtain the NGD parameters summarized in Table 3.

The present computational study was carried out in the bandwidth from $f_{\min}$ = 3.3 GHz to $f_{\max}$ = 3.9 GHz under more than 200 samples.

Parametric analyses were performed in function of resistor, R, and the TL characteristic impedance, Z. Figures 6(a), 6(b) and 6(c) display the cartographies of GD, S_{11} and S_{21}, respectively, when R is varied from 50 Ω to 100 Ω by keeping the other parameter values the same as in Table 3. It can be seen that the NGD center frequency is insensitive to R. However, the GD optimal absolute value and transmission coefficient optimal value at f_0 = 3.6 GHz are decreasing when R increases. The results of the other parametric analysis versus TL characteristic impedance, Z, are shown in Figure 7. Figures 7(a), (b) and (c) display the cartographies of GD, S_{11} and S_{21} when Z is varied from 0.5 kΩ to 1.5 kΩ by keeping the other parameters same as in Table 3. Once again, the NGD center frequency is insensitive to Z. The GD optimal absolute value and transmission coefficient optimal value at f_0 = 3.6 GHz behave inversely to the case of resistor variation.

After calculations and slight optimization of TL width and length, the NGD POC operating at 3.6 GHz was designed with the parameters indicated in Table 4.

Figure 8 display the compared results from calculations ("Calc.") and ADS® simulations ("Simu."). As expected theoretically, the BP NGD function is observed as depicted in Figure 8(a): the NGD centre frequency is of about f_0 = 3.6 GHz. Table 5 summarizes the differences between the Matlab calculated and ADS® simulated results. Figure 8(b) presents a comparison between the transmission coefficients. It can be seen that the loss is higher around the NGD centre frequency. Nevertheless, as depicted in Figure 8(c), the circuit is well-matched, i.e. S11 better than −10 dB over the frequency band. The slight deviation between the calculation and simulation

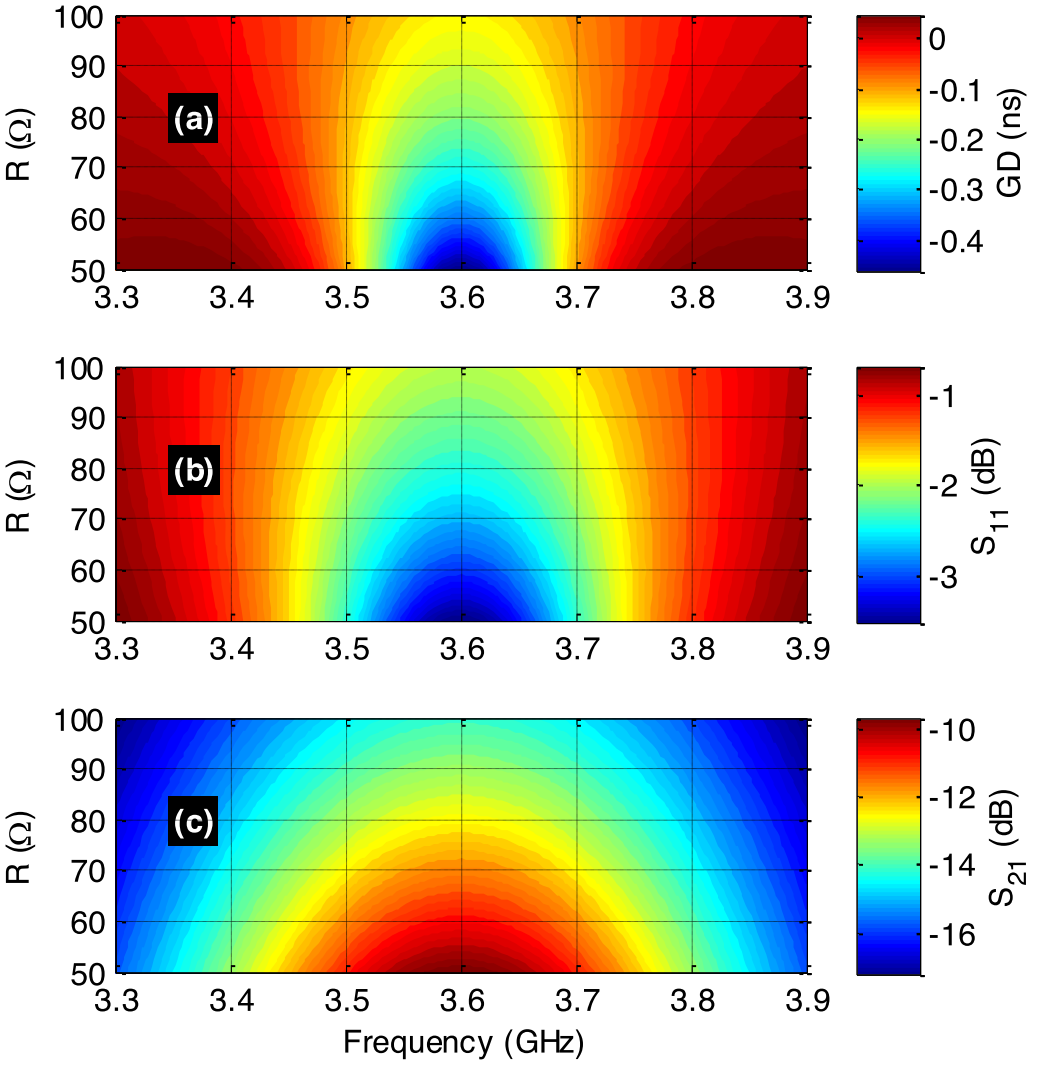

Figure 6. Parametric analyses of (a) GD, (b) S_{21} and (c) S_{11} versus (f, R).

Table 5. Characteristic of ideal and simulated NGD POCs

Characteristics	f_0 (GHz)	GD(f_0) (ns)	Δf (MHz)	S_{21} (f_0) (dB)	S_{11} (f_0) (dB)
Ideal	3.6	−0.34	327	−3.025	−10.63
Simu.	3.599	−0.298	172	−2.35	−12.67

herein is due to the skin effect and the substrate diffraction induced in the numerical simulation. Those effects are not included in the ideal model of our circuit in the S-matrix of (16).

4.2.2. *5.25-GHz BP NGD POC*

Table 6 summarizes the desired NGD specifications to design the 5G NGD POC to operate with 5.25 GHz centre frequency with respect to the US UNII standard [34]. The calculated NGD parameters by using design (37), (40) and (42) are given in Table 6.

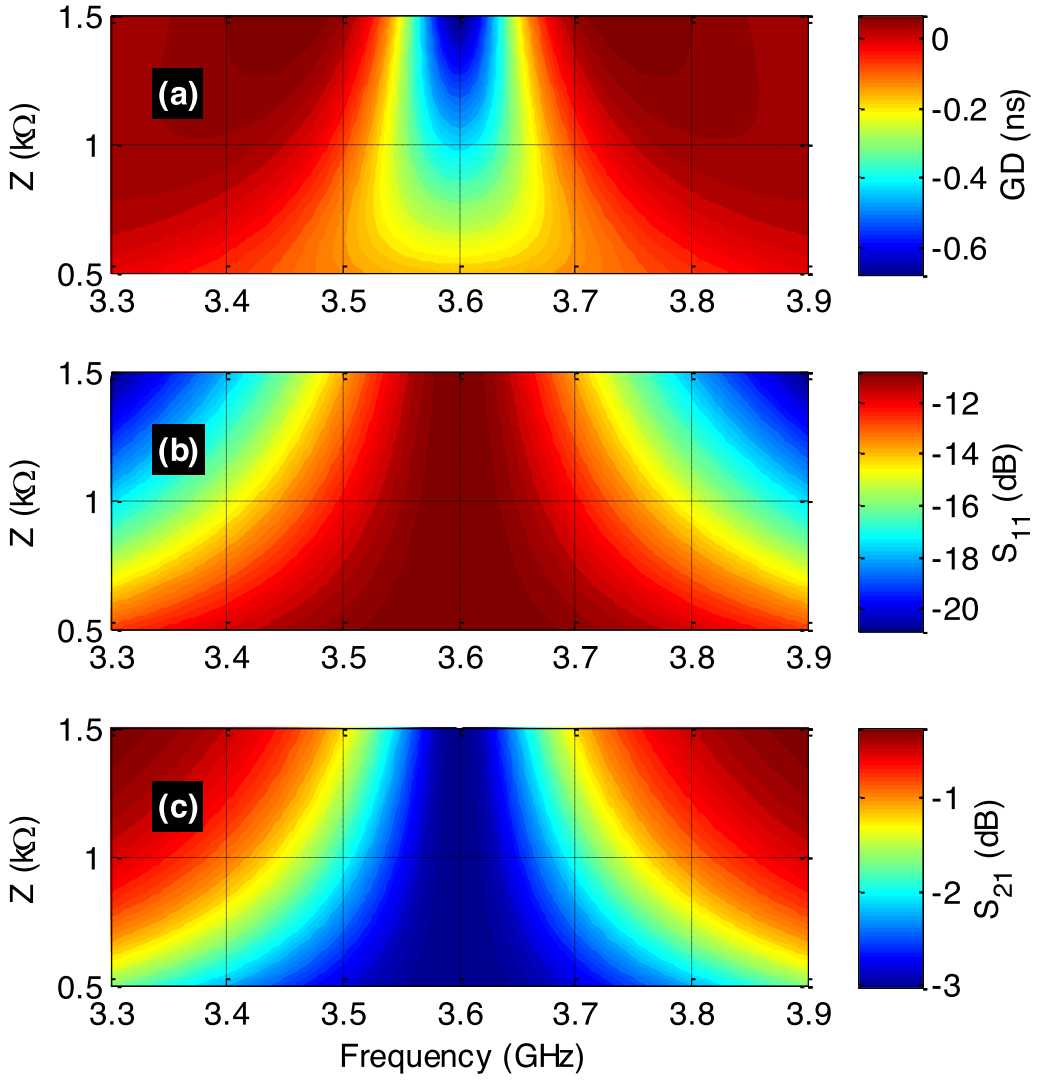

Figure 7. Parametric analyses of (a) GD, (b) S_{21} and (c) S_{11} versus (f, Z).

Table 6. NGD specifications and calculated parameters of the considered POC

Specifications	Designation	f_0	t	$-a_{\mathrm{dB}}$
	Value	5.25 GHz	0.23 ns	10 dB
NGD ideal parameters	Designation	τ_0	R	Z
	Value	47.6 ps	60 Ω	1 kΩ

In this case, the S-parameter analyses were computed in the bandwidth with f_{min} = 4.9 GHz and f_{max} = 5.6 GHz under more than 200 sampling.

Similar to the previous case of f_0 = 3.6 GHz, Figures 9 present the parametric analysis results with respect to resistor, R, and Figures 10 present that of parameter, Z. The same BP NGD behaviors are found even the center frequency is increased up to 5.25 GHz.

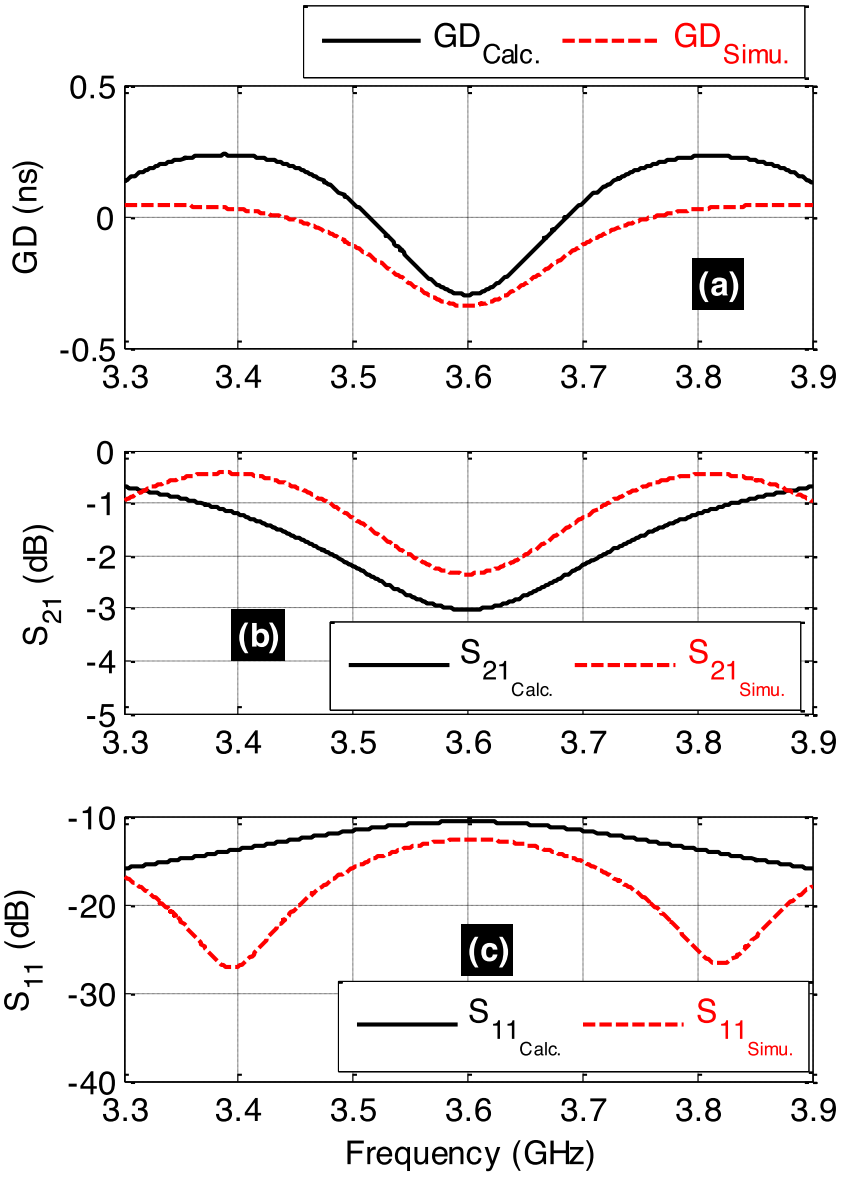

Figure 8. Calculated and simulated (a) GD, (b) S_{21} and (c) S_{11} of BP NGD circuit shown in Figure 5.

In an analogue way as in the previous case, the 5.25 GHz BP NGD POC was designed after calculations and slight optimization of TL width and length. The circuit was designed with the same parameters as indicated in Table 4 except the TL physical length, $d = 16$ cm.

Figure 11 illustrate the BP NGD behavior validation through theoretical and simulation results. Figure 11(a) presents a comparison between the calculated and simulated GDs. As expected, the NGD centre frequency is equal to $f_0 = 5.25$ GHz. Table 7 depicts the differences between the Matlab calculated and ADS® simulated results. Moreover, a good correlation between the calculated and simulated transmission and reflection coefficients are observed in Figures 11(b) and 11(c), respectively.

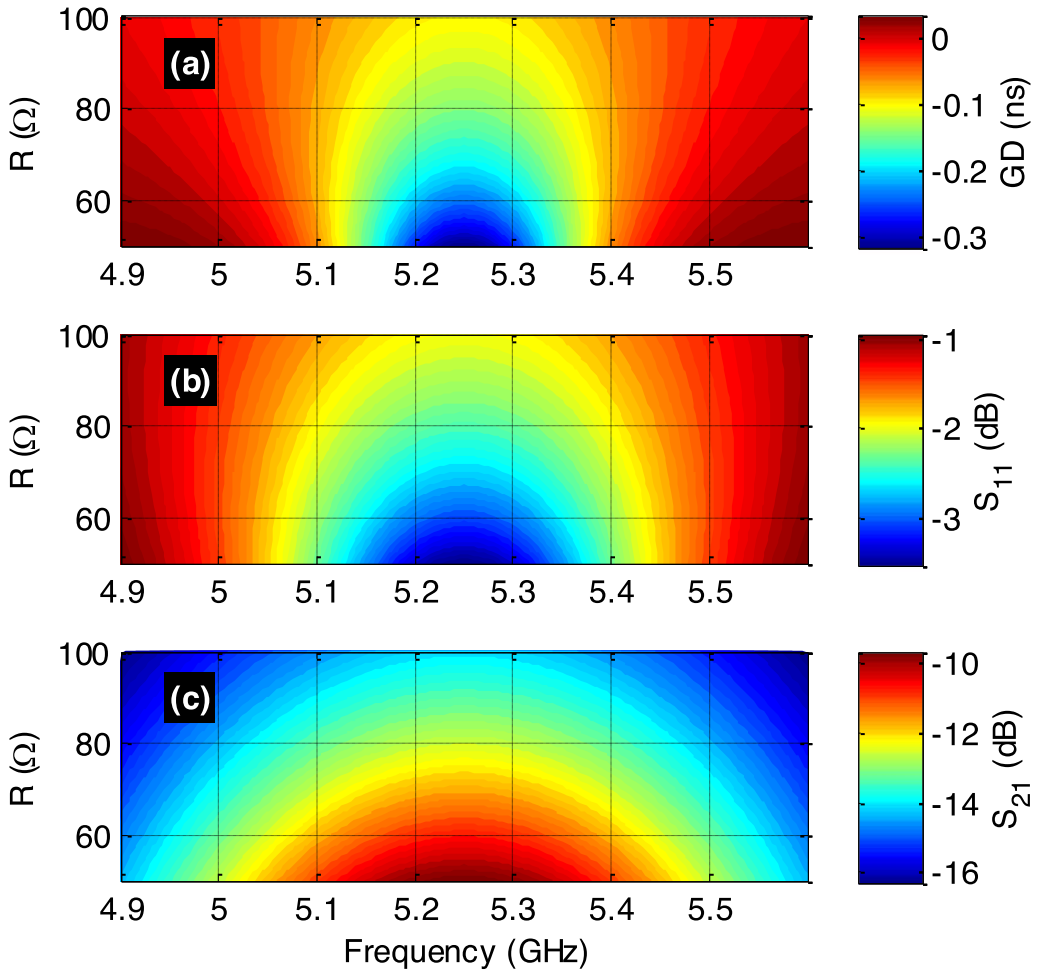

Figure 9. Parametric analyses of (a) GD, (b) S_{21} and (c) S_{11} versus (f, R).

Table 7. Characteristic of ideal and simulated NGD POCs

Characteristics	f_0 (GHz)	GD (f_0) (ns)	Δf (MHz)	S_{21} (f_0) (dB)	S_{11} (f_0) (dB)
Ideal	5.25	−0.334	470	−3.02	−10.6
Simu.	5.255	−0.2185	245	−2.447	−12.37

4.3. *Discussion on 5G applications*

The feasibility of the unfamiliar BP NGD function previously confirmed by the POC example raises questions on the ongoing research. The developed BP NGD concept led to think on a potential application for future design of RF and microwave devices.

4.3.1. *Tx–Rx architecture*

Among the different possibilities of application, we expect that the BP NGD responses can be used for the delay correction of multi-channel systems as the case of 802.11 a/b standards. One concrete scenario of application is illustrated by the network architecture of 5G displayed

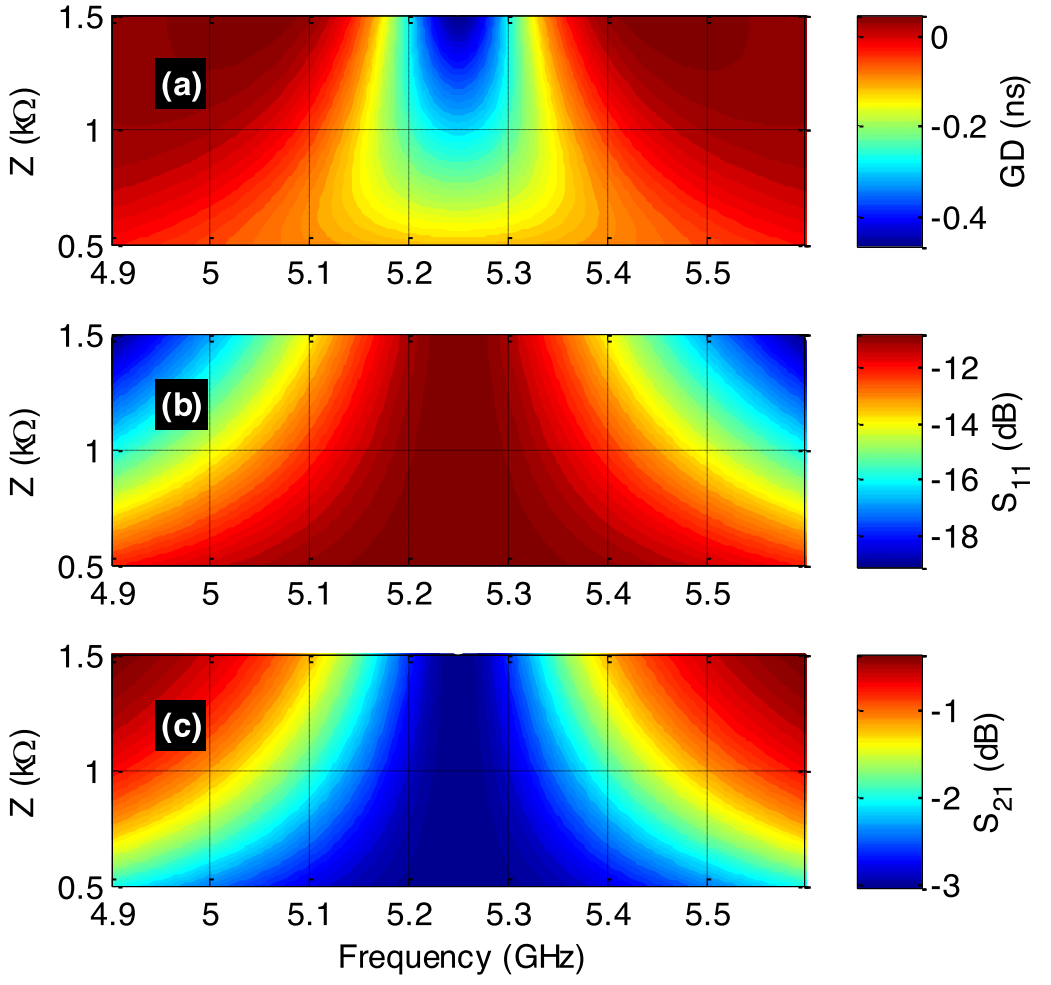

Figure 10. Parametric analyses of (a) GD, (b) S_{21} and (c) S_{11} versus (f, Z).

in Figure 12. Based on this scenario, we can imagine that multiple data can be transmitted from wireless communication standards as WiFi, GSM, LTE or 5G.

4.3.2. *Principle of differential delay correction with BP NGD function [21]*

In the more current cases of multiple connected objects, information can be transmitted from WSNs included in a Tx–Rx system. An example of WSN scenario and NGD delay effect reduction [20] between different channels, with centre frequencies-bandwidths, $(f_{m=1,2,3}, \Delta f_m)$, is illustrated in Figure 13(a). In the propagation environment with wave signal propagating at speed of light, c = 300,000 km/s, we can estimate the delay of the signal propagating from Tx($WS_{m=1,2,3}$) point, M_m, to Rx point, M, by:

$$t_m(f_m) = \frac{d_m}{c}. \tag{43}$$

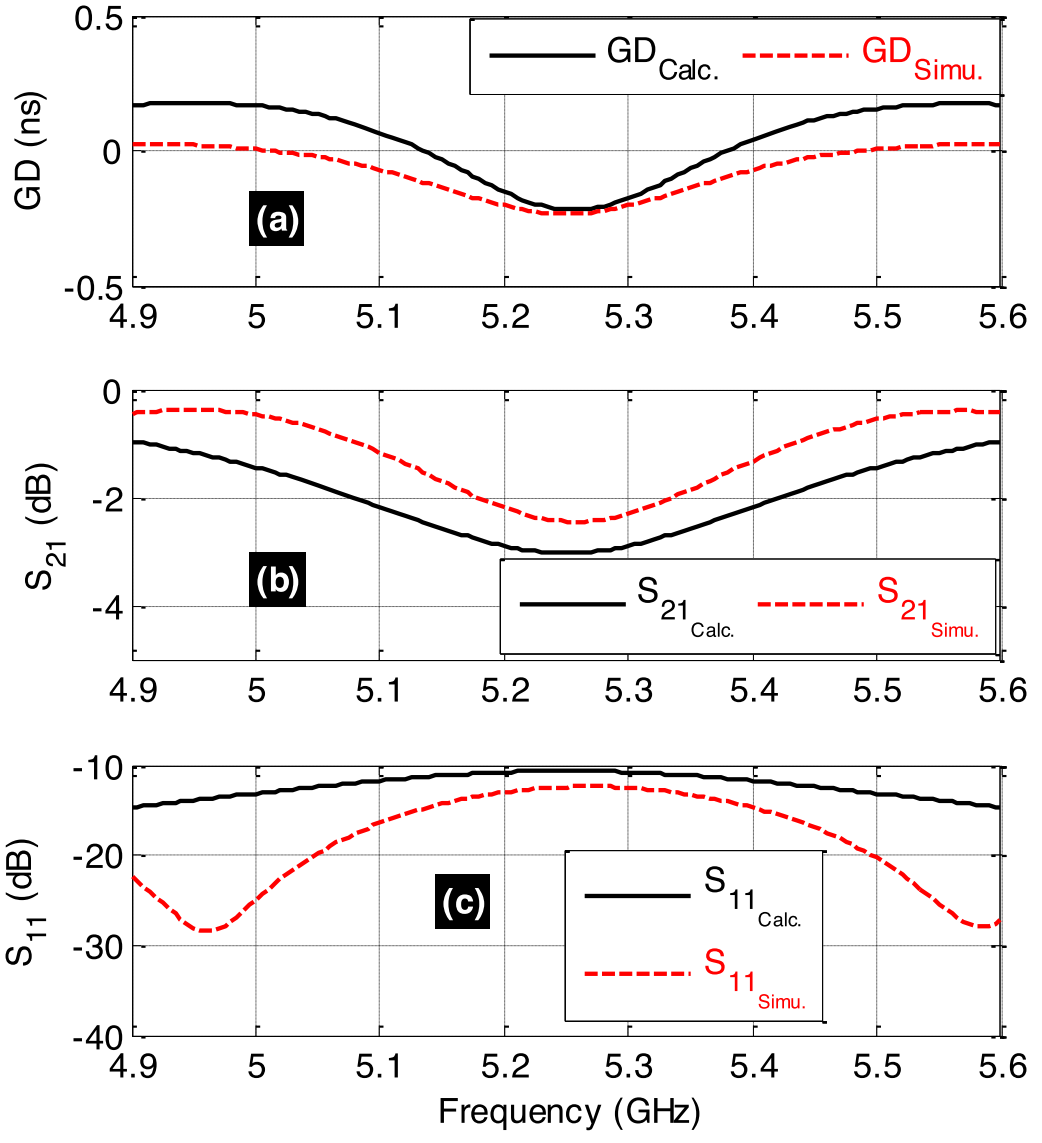

Figure 11. Calculated and simulated (a) GD, (b) S_{21} and (c) S_{11} of BP NGD POC operating with 5.25 GHz centre frequency.

In certain case of configuration as illustrated by Figure 9(a), we may consider delay differences:

$$\begin{cases} \Delta t_2 = t_2(f_2) - t_1(f_1) = \dfrac{d_2 - d_1}{c} \\ \Delta t_3 = t_3(f_3) - t_1(f_1) = \dfrac{d_3 - d_1}{c}. \end{cases} \tag{44}$$

Based on the innovative BP NGD function, a potential solution of delay difference inducing desynchronization between future 5G networks can be implemented with the configuration of Figure 13(b) [21]. It consists inserting a BP NGD function in the Rx system with, for example, dual

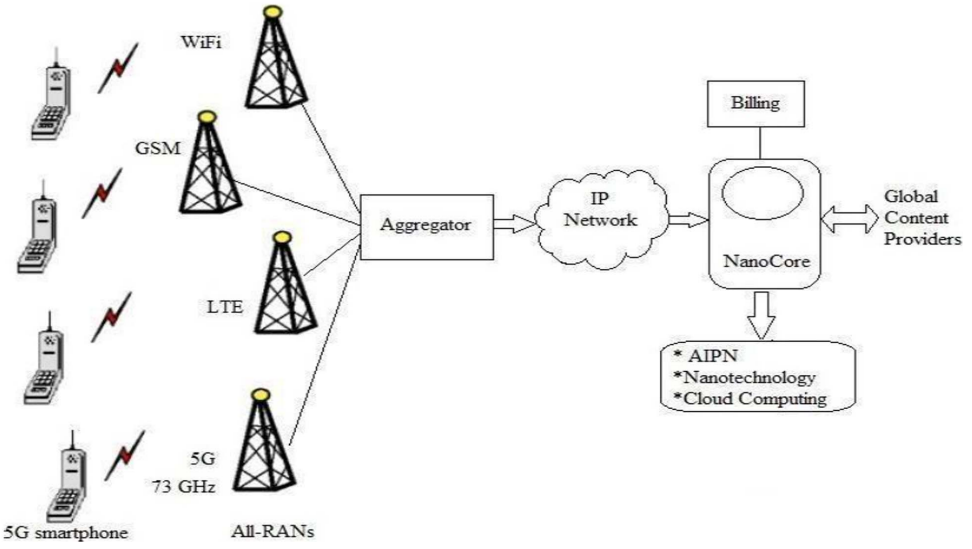

Figure 12. Network Architecture for 5G [3].

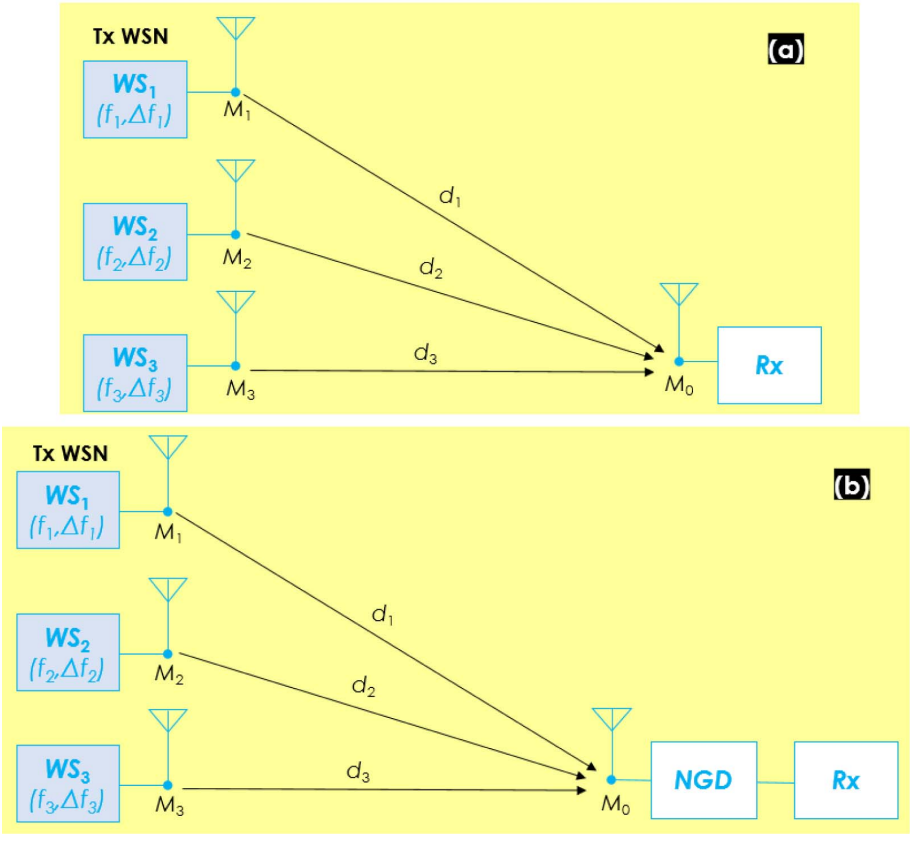

Figure 13. Configuration NGD delay reduction [21].

band NGD aspect defined by:

$$\begin{cases} \mathrm{GD}(f_2) = \dfrac{d_1 - d_2}{c} \\ \mathrm{GD}(f_3) = \dfrac{d_1 - d_3}{c}. \end{cases} \tag{45}$$

In this case, assuming ideal matching between the Rx antenna, NGD circuit and input of the Rx system, the total delay for each channel can be expected as:

$$\begin{cases} \mathrm{delay}_{\mathrm{total}}(f_1) = \dfrac{d_1}{c} \\ \mathrm{delay}_{\mathrm{total}}(f_2) = t_2 + \mathrm{GD}(f_2) = \dfrac{d_1}{c} \\ \mathrm{delay}_{\mathrm{total}}(f_3) = t_3 + \mathrm{GD}(f_3) = \dfrac{d_1}{c}. \end{cases} \tag{46}$$

5. Conclusion

An investigation of BP NGD function generated with open-ended stub based passive topology is introduced. A pedagogical BP NGD theory is investigated. The basic specifications of the BP NGD function are introduced. The NGD circuit is constituted by a shunt parallel resistor ended by an open-ended stub. The NGD analysis and synthesis equations have been derived from the S-matrix equivalent model. The S-matrix model of the proposed topology is established based on the impedance matrix. The NGD analysis is realized from the expression of GD given by the assumed transmission coefficient. The synthesis formulas enabling to determine the considered topology parameters in function of the desired NGD specifications are proposed.

The validity of the BP NGD theory is verified with a POC of microstrip circuit operating around the 5G frequencies 3.6 GHz and 5.25 GHz. The promising S-parameters and GD results were obtained and discussed. As expected, results showing a BP NGD behaviour with a good correlation between calculation and commercial tool simulation is obtained. The obtained results are promising as an upcoming application of the BP NGD function for future developments related to 5G system delay correction.

References

[1] 5G Infrastructure Association, "5G PPP – The 5G infrastructure Public-Private Partnership", 2020, https://5g-ppp.eu/ (Permission granted to produce Figure 1), accessed dec. 2020.

[2] IEEE Spectrum, "The Race to 5G: The Latest 5G News and Analysis", 2019, https://spectrum.ieee.org/static/the-race-to-5g.

[3] S. Arunachalam, S. Kumar, H. Kshatriya, M. Patil, "Analyzing 5G: prospects of future technological advancements in mobile", *IOSR J. Eng.* **1** (2018), p. 6-11, International Conference on Innovative and Advanced Technologies in Engineering.

[4] Q. Yu, "The era of 5G and its impacts on EMC design and testing", in *Proceedings of IEEE International Symposium on EMC, SI/PI, Washington, DC, USA*, 2017, p. 7-11.

[5] V. Tikhvinskiy, A. Aitmagambetov, V. Koval, P. Korchagin, "Experimental test results of EMC between 5G and radio relay links in millimeter band", in *2019 International Symposium on Electromagnetic Compatibility - EMC EUROPE*, IEEE, 2019, p. 220-225.

[6] K. Wiklund, P. Stenumgaard, "EMC challenges for the era of massive internet of things", *IEEE Electromagn. Compat. Mag.* **8** (2019), no. 2, p. 65-74.

[7] J. Zhang, S. Zhang, Z. Ying, A. S. Morris, G. F. Pedersen, "Radiation-pattern reconfigurable phased array with p-i-n diodes controlled for 5G mobile terminals", *IEEE Trans. Microw. Theory Tech.* **68** (2020), no. 3, p. 1103-1117.

[8] V. Kallnichev, "Analysis of beam-steering and directive characteristics of adaptive antenna arrays for mobile communications", *IEEE Antennas Propag. Mag.* **43** (2001), no. 3, p. 145-152.

[9] W. Alomar, A. Mortazawi, "Elimination of beam squint in uniformly excited serially fed antenna arrays using negative group delay circuits", in *Proceedings of IEEE International Symposium on Antennas and Propagation, Chicago, IL, USA, July 2012*, IEEE, 2012, p. 1-2.

[10] H. Mirzaei, G. V. Eleftheriades, "Arbitrary-angle squint-free beamforming in series-fed antenna arrays using non-foster elements synthesized by negative-group-delay networks", *IEEE Trans. Antennas Propag.* **63** (2015), no. 5, p. 1997-2010.

[11] A. Mortazawi, W. Alomar, "Negative group delay circuit", 2016, United States Patent Application US20160093958.

[12] M. Zhu, C.-T. M. Wu, "Reconfigurable series feed network for squint-free antenna beamforming using distributed amplifier-based negative group delay circuit", in *Proceedings of 2019 49th European Microwave Conference (EuMC), Paris, France, 1–3 October 2019*, IEEE, 2019, p. 256-259.

[13] W. Alomar, A. Mortazawi, "Method of generating negative group delay in phase arrays without using lossy circuits", in *Proceedings of IEEE Antennas and Propagation Wireless Symposium (IWS) 2013, Beijing, China, 14–18 April 2013*, IEEE, 2013, p. 1-4.

[14] H. Mirzaei, G. V. Eleftheriades, "Realizing non-Foster reactive elements using negative-group-delay networks", *IEEE Trans. Microw. Theory Tech.* **61** (2013), no. 12, p. 4322-4332.

[15] T. Zhang, R. Xu, C. M. Wu, "Unconditionally stable non-foster element using active transversal-filter-based negative group delay circuit", *IEEE Microw. Wirel. Compon. Lett.* **27** (2017), no. 10, p. 921-923.

[16] C. D. Broomfield, J. K. A. Everard, "Broadband negative group delay networks for compensation of oscillators, filters and communication systems", *Electron. Lett.* **36** (2000), no. 23, p. 1931-1933.

[17] B. Ravelo, "Distributed NGD active circuit for RF-microwave communication", *Int. J. Electron. Commun.* **68** (2014), no. 4, p. 282-290.

[18] L.-F. Qiu, L.-S. Wu, W.-Y. Yin, J.-F. Mao, "Absorptive bandstop filter with prescribed negative group delay and bandwidth", *IEEE Microw. Wirel. Compon. Lett.* **27** (2017), no. 7, p. 639-641.

[19] T. Shao, Z. Wang, S. Fang, H. Liu, Z. Chen, "A full-passband linear-phase band-pass filter equalized with negative group delay circuits", *IEEE Access* **8** (2020), p. 43336-43343.

[20] B. Ravelo, S. Lalléchère, A. Thakur, A. Saini, P. Thakur, "Theory and circuit modelling of baseband and modulated signal delay compensations with low- and band-pass NGD effects", *Int. J. Electron. Commun.* **70** (2016), no. 9, p. 1122-1127.

[21] F. Wan, N. Li, W. Rahajandraibe, B. Ravelo, "Reduction technique of differential propagation delay with negative group delay function", in *Proceedings of IEEE EuCAP 2020, Copenhagen, Denmark, 15–20 March 2020*, IEEE, 2020, p. 1-5.

[22] Z. Wang, Y. Cao, T. Shao, S. Fang, Y. Liu, "A negative group delay microwave circuit based on signal interference techniques", *IEEE Microw. Wirel. Compon. Lett.* **28** (2018), no. 4, p. 290-292.

[23] C.-T.-M. Wu, T. Itoh, "Maximally flat negative group-delay circuit: a microwave transversal filter approach", *IEEE Trans. Microw. Theory Tech.* **62** (2014), no. 6, p. 1330-1342.

[24] H. Choi, Y. Jeong, J. Lim, S. Y. Eom, Y. B. Jung, "A novel design for a dual-band negative group delay circuit", *IEEE Microw. Wirel. Compon. Lett.* **21** (2011), no. 1, p. 19-21.

[25] G. Chaudhary, Y. Jeong, J. Lim, "Miniaturized dual-band negative group delay circuit using dual-plane defected structures", *IEEE Microw. Wirel. Compon. Lett.* **24** (2014), no. 8, p. 521-523.

[26] G. Chaudhary, J. Jeong, P. Kim, Y. Jeong, J. Lim, "Compact negative group delay circuit using defected ground structure", in *2013 Asia-Pacific Microwave Conference Proceedings (APMC), Seoul*, IEEE, 2013, p. 22-24.

[27] G. Liu, J. Xu, "Compact transmission-type negative group delay circuit with low attenuation", *Electron. Lett.* **53** (2017), no. 7, p. 476-478.

[28] T. Shao, Z. Wang, S. Fang, H. Liu, S. Fu, "A compact transmission line self-matched negative group delay microwave circuit", *IEEE Access* **5** (2017), p. 22836-22843.

[29] G. Chaudhary, Y. Jeong, J. Lim, "Miniaturized dual-band negative group delay circuit using dual-plane defected structures", *IEEE Microw. Wirel. Compon. Lett.* **21** (2011), no. 1, p. 19-21.

[30] T. Shao, S. Fang, Z. Wang, H. Liu, "A compact dual-band negative group delay microwave circuit", *Radio Eng.* **27** (2018), no. 4, p. 1070-1076.

[31] B. Ravelo, "Similitude between the NGD function and filter gain behaviours", *Int. J. Circ. Theor. Appl.* **42** (2014), no. 10, p. 1016-1032.

[32] B. Ravelo, "On the low-pass, high-pass, bandpass and stop-band NGD RF passive circuits", *URSI Radio Sci. Bull.* **2017** (2017), no. 363, p. 10-27.

[33] B. Ravelo, S. Lalléchère, "FUTURE NETWORKS: 5G AND BEYOND. Design of 3.6-GHz 5G NGD passive circuit", 2020, 20e Journées Scientifiques URSI-France (JS'20), Future Network: 5G and Beyond, march 2020, Paris, France. https://hal.archives-ouvertes.fr/hal-02814577.

[34] Aruba Network, "802.11ac In-Depth", 2014, 37 pages, https://www.arubanetworks.com/assets/wp/WP_80211acInDepth.pdf.

Comptes Rendus
Physique
2021, 22, nº S1, p. 73-82
https://doi.org/10.5802/crphys.63

URSI-France 2020 Workshop / *Journées URSI-France 2020*

Enhanced integrated multiband HPM radiator, combining a hyperband source with a high-Q frequency selective surface

Fernando Albarracin-Vargas [*, a], **Felix Vega** [a, b], **Chaouki Kasmi** [a, c], **David Martinez** [a] **and Lars Ole Fichte** [c]

[a] Directed Energy Research Centre, Technology Innovation Institute, Abu Dhabi, UAE

[b] Universidad Nacional de Colombia, Facultad de Ingenieria, Sede Bogota, Colombia

[c] Faculty of Electrical Engineering, Helmut Schmidt University, Germany

E-mails: fernando.albarracin@derc.tii.ae (F. Albarracin-Vargas), felix.vega@derc.tii.ae (F. Vega), chaouki.kasmi@derc.tii.ae (C. Kasmi), david.martinez@derc.tii.ae (D. Martinez), lo.fichte@hsu-hh.de (L. O. Fichte)

Abstract. This work presents advances on the development of a resonant radiator, obtained as the augmentation of a conventional Impulse Radiating Antenna (IRA) with a Frequency Selective Surface (FSS), in the L-band. An improved passband-type FSS is obtained by exploring the Multiple Split Ring Resonators (MCSRR) unit cells to obtain a higher *Q*-factor radiator. The effects of a multiband and of a tunable FSS's are also studied and verified via simulations. A variety of applications are enabled by modifying the UWB waveform from the IRA into a damped sinusoidal from the combined radiator like IEMI testing, hardening of infrastructures, cloaking of wide aperture radiators, among other. The system analysis methodology can also be applied to other FSS geometries, or the combinations of various of them.

Keywords. Frequency selective surface, Complementary split ring resonators, Electromagnetic hardening, Hyperband radiators, HPM sources, IEMI.

Available online 6th May 2021

1. Introduction

Design and development of hardening modules for critical infrastructures like airports, electrical grids, and IT headquarters involve the study of the Electromagnetic Compatibility (EMC), and Intentional Electromagnetic Interference (IEMI) effects. IEMI studies requires the characterization of potential disruptions on modern microelectronic systems. Such characterization require the use of high-power electromagnetic radiators consisting, in general, of complex, high-cost generators and sophisticated antennas [1, 2]. The task becomes even more challenging when tunable, band-pass, high power emitters are required to asses the radiated susceptibility of equipment and systems.

* Corresponding author.

A key part of the design of a pulse radiator is the antenna system. This involves the use of radiators with the ability to radiate at low frequency, nearly constant gain and impedance over bandwidth ratios greater than 10 (i.e., hyperband region), and high-voltage handling capabilities. The Impulse Radiating Antenna (IRA), first proposed by Baum and Farr [3, 4], is one of the most known radiators used in IEMI tests, due to its hyper-band response and high-voltage capability. The working principle of an IRA is to launch a spherical and non-dispersive TEM wave-front from the focal point of a parabolic reflector. Such a TEM spherical wave propagates through the feeder arms, that act as a TEM transmission line.

Both components mentioned so far, the antenna and the pulsed source, share two important characteristics: high cost and fixed working bandwidth. In this context, the use of a frequency selective planar structure arises as a strategy to add frequency agility to the system: Antenna + HPM source. The ability to radiate over multiple bands is possible by arranging multiple resonating unit-cell types into the Frequency Selective Surface (FSS), or by changing the separation of a multilayer lattice.

In related studies, it has been shown that a metal-grid embedded within the walls of a building displays interesting properties when illuminated with an ultra-wideband (UWB) radiator. Tesche *et al.* [5] analyzed the possibility of damping the emitted pulse signal by chaining a set of metal grids placed in front of the antenna. These serve to transform the fast-pseudo-impulse from the antenna into a damped sinusoidal waveform. A low-pass FSS that can be integrated into an ultra-wideband radiator was presented in [6]. Other alternatives, like the use of self-actuated surfaces, using arrays of semiconductors, are described in [7, 8]. A Voltage-controlled piezoelectric actuators are used to tune an FSS in [9].

Modern technologies, like the fifth generation (5G) wireless communication, can also take advantage of radiators enhanced with FSS's. On one hand, specific IEMI studies on systems in the sub-1 GHz band supporting Internet of things (IoT) platforms, and in the sub-6 GHz band used for handheld devices communications, are enabled because of the electrically small size of the resonant unit cells commonly implemented in FSS's. This condition allows developing manageable FSS's to conduct those tests. On the other hand, for higher frequency band services (i.e. 26 GHz band and beyond), where the multiple beam and massive MIMO capabilities are intended, radiators integrated with FSS's have been reported in [10]), in the form of pass-band radomes that prevent the transceiver from IEMI effects at frequencies other than the working ones.

FSS's are narrowband passive structures that exhibit interesting properties when illuminated by electromagnetic fields [11]. The well-known Split Ring Resonators (SRR) proposed in [12], and its complementary version (i.e., CSRR), have been studied and characterized in the last years as a compact structure to compose an FSS [13, 14]. To avoid diffractive effects and grating-lobes on the intended radiated beam, both the unit cell size and separation must be smaller than the wavelength of the incident radiation.

A relevant characteristic of these resonators is the capability of being cross-polarized. In an SRR, a polarizing surface results by either the E- or the H-field passing through the structure. This phenomenon produces a band-stop response [13]. On the other hand, an electric dipole is induced from the excitation of a CSRR with an incident wave whose electric field component is parallel to the rings' gaps, resulting in a bandpass filtering surface. Marques *et al.* [13] presented an analytical solution for the behavior of FSS based on SRR and CSRR cells. Although restricted to the infinitesimally thin perfect conductor in free space, the analytical approach gives a first approximation to the response of a band-pass-type FSS. Bilotti *et al.* proposed an approximation to the analytical model of Multiple-SRR (MCSRR) and Spiral Resonators in [15].

In this work, we explore a concept that can be used when a high-amplitude adjustable and high Q-factor band-pass electric field is required. The resulting integrated multiband and tunable

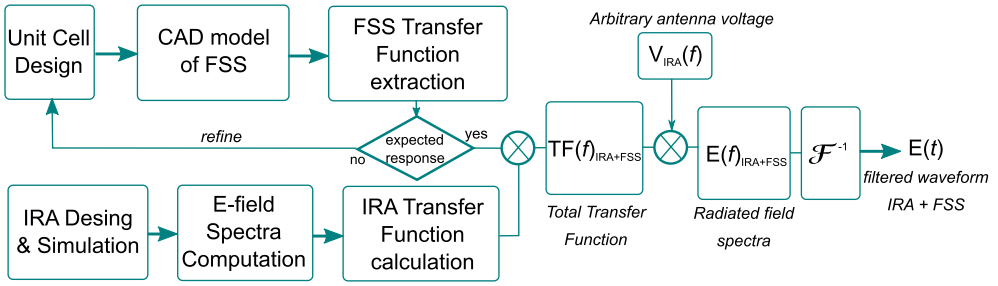

Figure 1. Design flowchart of the proposed integrated HPM radiator.

HPM radiators, are composed of a CSRR-based FSS in the near-field of a hyperband radiator, like the IRA. All the designs presented comprise a strategy to add waveform and frequency agility to the resulting HPM source. An improved version of the passband FSS is presented as the implementation of a Multiple-CSRR (MCSRR) instead of the conventional CSRR to obtain higher Q-factor response. The enhanced single-band and the multiband integrated HPM source approach, and the unit cell designs are described in Section 2. The cascaded-system analysis of the integrated radiator is presented in Section 3. Conclusions are included in Section 4.

2. Multiband and enhanced Q-factor FSS

In this section, we present an application of the proposed approach as the design of the FSS to be integrated with the IRA. The complete design methodology can be summarized in the scheme shown in Figure 1. The unit cell is designed and its CAD model is simulated as a periodic structure to obtain the S-parameter matrix of the FSS. A transfer function can be extracted by computing a representation of the electric and magnetic fields as voltage and current driving a two-port ABCD parameter set. A *total* transfer function is obtained as the product of the FSS transfer function and the transfer function from the IRA, which relates the radiated electric field with the voltage driving the antenna. Finally, the radiated electric field from the integrated HPM radiator can be computed, for any voltage waveform driving the IRA.

Two examples are presented as passband FSS's. The first one is a single layer FSS based on a conventional two-slots CSRR augmented with an additional pair of rings. A second FSS design incorporates of a second CSRR of different size to implement a multiband FSS whose passing bands are tuned around 1.5 GHz and 2.4 GHz, respectively.

2.1. *Single frequency CSRR, and MCSRR design*

Figure 2a shows the CSRR unit cell, inspired by [14], used to illustrate the single band FSS tuned at $f_0 = 1.5$ GHz. The circuit model of the unit cell is shown Figure 2b. As an alternative to enhance the selectivity of the passband FSS, a modified unit cell based on the multiple complementary ring resonators (MCSRR) is designed. The new geometry is sketched in Figure 2c, and its associated circuit model is shown in Figure 2d. The reactive parameters of the circuit models shown in Figures 2b,d, can be computed as [15, 16]:

$$\begin{aligned} L_0 &= (\mu_0/4\varepsilon_0)C_{0,\mathrm{SRR}} \\ C_c &= 4(\varepsilon_0/\mu_0)L_s \\ f_0 &= \frac{1}{2\pi}\sqrt{\frac{1}{L_c C_c}} \end{aligned} \tag{1}$$

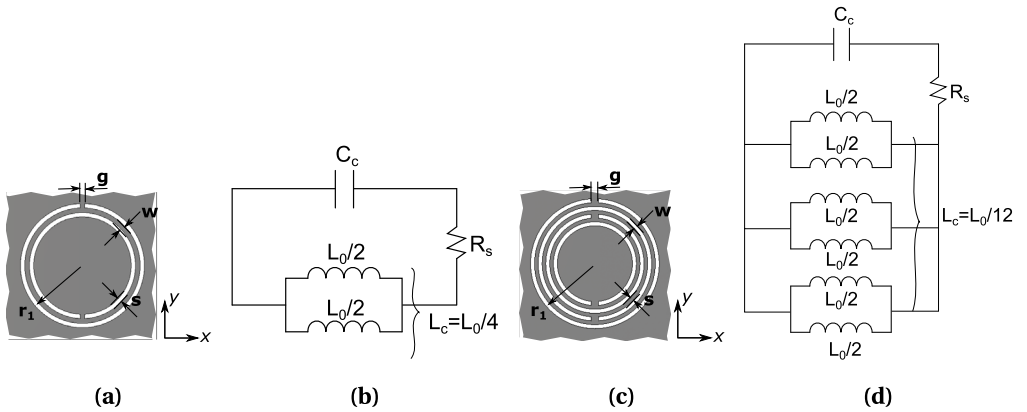

Figure 2. (a) Sketch of the CSRR unit cell geometry, $n = 2$, (all the dimensions are in mm): $w = s = 1$; $r_1 = 13.1$; $g = 1$. (b) Circuit model of the CSRR. Values are computed as in (1): $L_c = 2.06$ nH, $C_c = 5.62$ pF, $R_s = 0$ (lossless case). (c) Geometry of the MCSRR unit cell, for $n = 4$, re-tuned to resonate at 1.5 GHz. $w = 0.78$; $r_1 = 10$; $g = 1$; $s = 0.35$. (d) Circuit model of the MCSRR. Circuit quantities are: $L_c = 2.63$ nH, $C_c = 4.58$ pF.

where f_0 is the resonant frequency, C_c is the capacitance of a conductor disk surrounded by a ground plate, L_0 is the inductance connecting such disk to ground from two sides. For duality, the parameter $C_{0,\mathrm{SRR}}$, which represents the total capacitance between the conductor strips in the equivalent SRR, is used to compute L_0. In the same way, the total inductance of the SRR, L_S, is used to estimate the capacitance C_c in the CSRR. This approximations are valid for the lossless case. Higher order effects like mutual inductances, the mutual capacitances between non adjacent slots and the split inductance are neglected in the model [15]. The exact solution for L_s for the conventional SRR is presented in [17]. An approximate model for the total inductance L_C in the MCSRR case is described in [15].

The narrowband response of both, the CSRR- and the MCSRR-FSS showing its bandpass filter capability is observed in Figure 3, where each unit cell has been simulated as a periodic lattice to form and ideally infinite FSS. Only waves whose E-field is aligned to the gaps in the rings (y-axis in Figure 2a) will be able to pass through the FSS, at frequencies slightly higher than the resonant frequencies of the composing CSRR sizes. The 3 dB-bandwidth of the passband around f_0 is 35 MHz (2.33%), for the CSRR and 4.6 MHz (0.31%) for the MCSRR case. The Q-factor, $Q = f_0/BW_{3\ \mathrm{dB}}$, yields 42.8 for the CSRR and 328 for the MCSRR. The improvement in the selectivity of the passband response is evident for the MCSRR.

Since the increase in the Q-factor comes with a miniaturization effect, represented by a resonant frequency shift to lower frequencies, a re-tuning of the geometrical parameters of the MCSRR was needed to compare both FSS's at the same frequency, $f_0 = 1.475$ GHz. The final dimensions are described in the caption of Figure 2. A more detailed analysis of multiple turns ring resonators and spiral resonators is presented in [15]. The resulting radiated electric field waveform is presented in Section 3.

2.2. *Multiband single layer FSS*

The proposed unit cell is to be supported by a low relative permittivity substrate, (ideally $\epsilon_r = 1$), simulated as losses free as a first approximation. It is composed of two different CSRRs, oriented as shown in Figure 4a. Since the intended response of the FSS is multiband, each band shall be

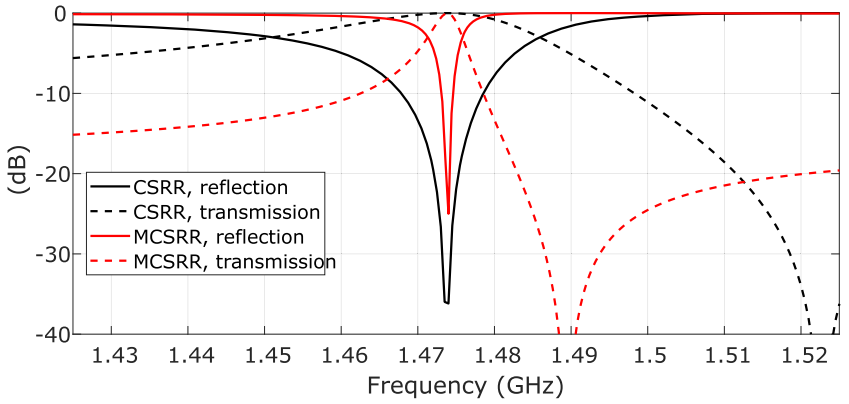

Figure 3. Reflection and transmission parameters for the CSRR and the MCSRR FSS's. The improvement in the Q-factor is evident for the MCSRR ($n = 4$).

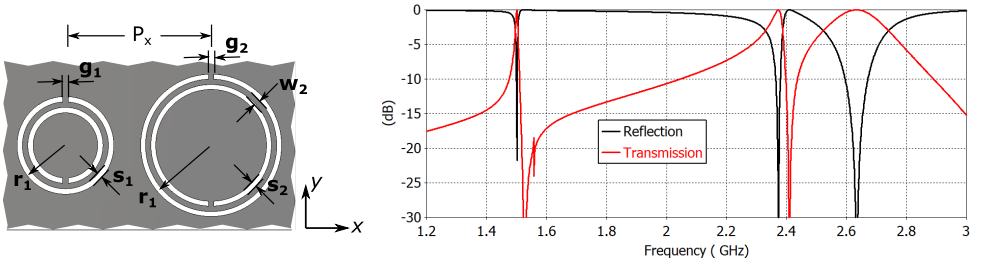

(a) **(b)**

Figure 4. (a) Sketch of the two CSRR unit cells geometry. Unit cell 1, on the left, is associated with a passband frequency of 2.4 GHz. The unit cell on the right is resonant at 1.5 GHz. The dimensions are (all in mm) $P_x = 26.5$, $P_y = 26.5$, $r_1 = 8.5$, $r_2 = 12.65$, $g_1 = g_2 = 1$, $s_1 = s_2 = 1$, $w_1 = w_2 = 1$, and (b) FSS response, simulated as an infinite periodic structure.

tuned according to the resonant frequency of each unit-cell size. Figure 4b shows the reflection and the transmission parameter, respectively, for the CSRR-based FSS. An additional resonant frequency is observed at 2.6 GHz in Figure 4b. This is associated with a high-frequency resonance of the 1.5 GHz unit cell. This additional passband is expected to be overlapped with the response from the 2.4 GHz unit cell.

3. HPM radiator integration

3.1. *Reflector based IRA*

The sketch of a two-arm IRA is shown in Figure 5a. When connected to a pulsed voltage source, the IRA radiates an impulse-like waveform over a narrow beam on boresight direction (z-axis in Figure 5a). The electric field related to the waveform radiated by the IRA can be described as [18]:

$$E_t(t,r) = f_1 \frac{1}{2\pi f_g} \left(\begin{array}{c} \dfrac{V(t-r/c)}{r} \dfrac{\sin(\beta)}{1+\cos(\beta)} - \dfrac{V(t-L/c-R_2/c)}{R_2} \dfrac{\sin(\beta)+\sin(\gamma)}{1+\cos(\beta-\gamma)} \cdots \\ -\dfrac{4}{D} V(t-2F/c-r/c) + (2+2\cos(\gamma)) \dfrac{V(t-l/c-R_2/c)}{D} \end{array} \right) \left(\frac{V}{m}\right) \tag{2}$$

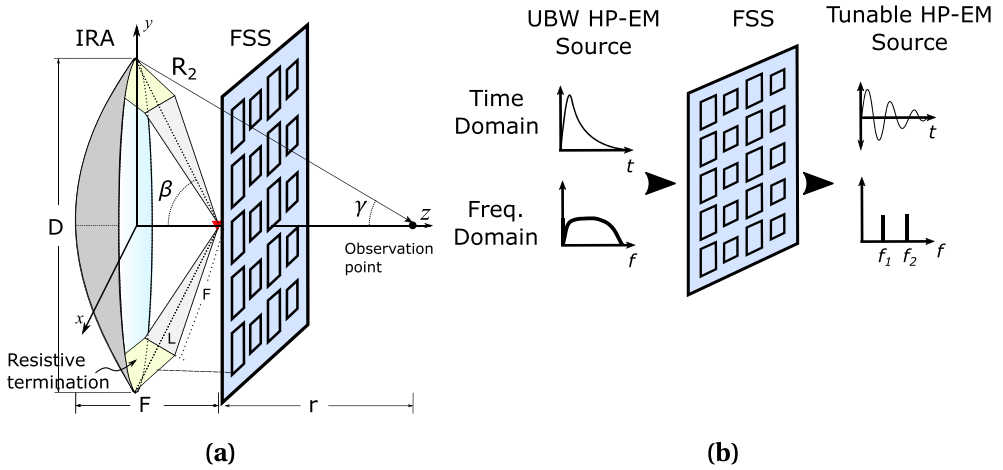

Figure 5. (a) IRA + FSS geometry, and (b) principle of the Tunable HPM Radiator.

where $V(t)$ is the feeding voltage, $f_1 = 1$ for the two-arm IRA, c is the speed of light, and r is the distance between the focal point and the measurement point. The geometric impedance factor, $f_g = Z_{\text{IRA}}/120\pi$, is a reference parameter related to the feeder geometry which acts as the transmission line of the spherical wave into the reflector. Z_{IRA} is the input impedance of the antenna. D, F, l, β, γ, and R_2 are described in Figure 5a. The two-arm IRA presented in this paper is designed with the following parameters: $D = 1$ (m), $F/D = 0.4$, $Z_{\text{IRA}} = 400$ (Ω).

3.2. *Tunable HPM radiator with FSS*

The multiband radiator concept presented here is depicted in Figure 5b. The FSS acts as a pass-band filter with a high-Q factor response. As mentioned before, the FSS modifies the impulse-like waveform propagating from the IRA by converting it into a damped sinusoidal. For the case of the multiband FSS, the radiated waveform will present two main frequency components. Only the electric field components aligned with the y-axis, and around the resonant frequency of each unit cell, will effectively pass through the FSS. Unit cells of the same size are aligned along the y-axis, in order to align each resonant polarization with the incoming wideband transient wave from the IRA.

One effective way of determining the radiated electric field waveform, from the IRA + FSS system, is by applying classical linear cascaded system approach, as outlined in Figure 1.

The field radiated from the IRA in (2) can be related to the voltage at the feed point through the transfer function, $T_A(f)$, computed as

$$T_A(f) = E_{\text{IRA}}(f)/V_{\text{IN}}(f). \tag{3}$$

$T_A(f)$ can be understood as the inverse of the effective length, $l_{\text{eff}(f)}$ of the IRA. Note that the $E_{\text{IRA}}(f)$ does not necessarily have to be computed in the far-field region. Due to the nature of the radiation from a parabolic reflector, a normally incident E field propagates through the FSS from the left (see Figure 5b), and continues along the z-axis, but with its spectral characteristics filtered.

By applying the chain parameters approach, as described in [5], it is possible to represent the FSS by a linear two-port network. The conventional currents and voltages are linearly related to

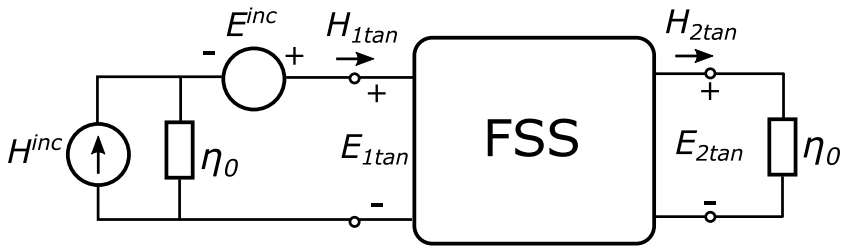

Figure 6. FSS, as an $ABCD$ parameter circuit representation. Tangential E- and H-field act as the voltage and current variables of a conventional circuit model. The FSS in this paper replaces the conductive grid representation in [5].

the tangential components of the E- and H-fields at the input and output ports, as depicted in Figure 6. This yields to

$$\begin{bmatrix} E_{1,\tan} \\ H_{1,\tan} \end{bmatrix} = \begin{bmatrix} A & B \\ C & D \end{bmatrix} \begin{bmatrix} E_{2,\tan} \\ H_{2,\tan} \end{bmatrix}. \tag{4}$$

The tangential fields $E_{1,2}$, and $H_{1,2}$ represent the network input and output voltages, $V_{1,2}$, and currents $I_{1,2}$, respectively, of a terminated two-port network. By using the expression for the current in the load (see [19], ch. 3), the same expression gives the voltage (or current) transfer function, as the ratio of $V_2(f)/V_1(f)$. The current through the load, represented by $H_{2,\tan}$, can be computed as

$$\begin{aligned} H_{2,\tan} &= \frac{E_{2,\tan}}{\eta_0} = \frac{E^{\text{inc}}}{(A+\eta_0 C)\eta_0 + (B+\eta_0 D)} \\ E^{\text{inc}} &= 2E_{1,\tan} \end{aligned} \tag{5}$$

where η_0 is the free space impedance (i.e., 377 Ω).

Then, the transfer function of the FSS can be easily computed from the transmission-reflection parameters shown in Figure 3. In this model, $E_{1,\tan}(f) = E_{\text{IRA}}(f)$. The output tangential $E_{\text{IRA+FSS}}(f)$, in the y-axis direction, can be computed as

$$\begin{aligned} E_{\text{IRA+FSS}}(f) &= E_{2,\tan} = 2E_{1,\tan}\left(\frac{\eta_0}{(A+\eta_0 C)\eta_0 + (B+\eta_0 D)}\right) \\ E_{\text{IRA+FSS}}(f) &= T_{\text{FSS}} E_{1,\tan}. \end{aligned} \tag{6}$$

Finally, an expression for the electric field once the transient pulse passes through the FSS is given by

$$\begin{aligned} T_{\text{TOTAL}}(f) &= T_A(f)\, T_{\text{FSS}}(f) \\ E_{\text{IRA+FSS}}(f) &= T_{\text{TOTAL}} V_{\text{IN}}(f). \end{aligned} \tag{7}$$

Once the complete transfer function of the integrated IRA + FSS radiator is extracted, the spectral response of the electric field waveform, related to a pulsed voltage signal driving the IRA terminals, i.e., $V_{\text{IN}}(f)$, can be analytically evaluated, as it will be shown below. The electric field in the time domain can be computed as the inverse Fourier transform of $E_{\text{IRA+FSS}}(f)$.

3.3. *Results*

The integrated FSS + IRA radiator is modeled in the commercial suite CST. A square array of unit cells is designed to cover 1 m^2, which is the area circumscribing the reflector aperture. In both FSS typologies we are illustrating, the FSS structure is located 10 cm away from the focal point of the IRA. Although a larger separation between FSS and antenna would minimize multiple reflections, diffracted waves from the perimeter of the FSS structure will have a more significant effect in the filtered pulse.

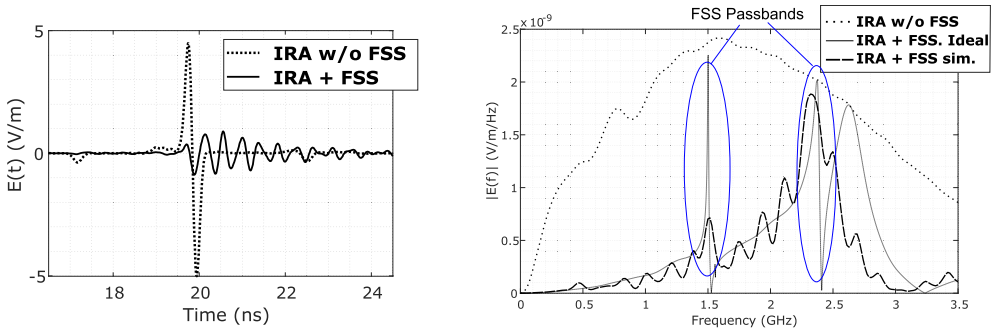

(a) **(b)**

Figure 7. (a) Electric field in the time domain, 5 m away from the focal point of the IRA. (b) Spectral amplitude of the IRA + FSS.

The multiband FSS is designed as an array of 22×36 unit cells (see Figure 4a). The whole system, IRA + FSS, is discretized into a 50 million cells mesh, applying a electric symmetry around the xz-plane (see Figure 5b). An absorbing open boundary was set quarter-wavelength (at 1.5 GHz) away from the structure. 19,600 time steps were simulated with a time-step length of 7.6×10^{-4} ns. The cell fraction at maximum frequency was set to 20. The simulation time reached 2 h in a computer with a GPU of 512 cores and 6 GB memory size. The electric field has been computed 5 m away from the focal point of the IRA, in broadside (z-axis). The time-domain response of the radiated electric field is shown in Figure 7a. The field radiated by a conventional two-arm unloaded IRA, with the same dimensions, is also shown as a reference. In both cases, a Gaussian pulse, with spectral content ranging from 0 to 3.5 GHz and 18 V in amplitude in the time domain, is used as the driving signal. The damped-like sinusoidal response of the proposed design is observed, as expected.

The passband filtering behavior of the FSS loading the IRA is observed in the frequency domain response of the electric field, as shown in Figure 7b. The ideal filtering response of the IRA + FSS system can also be computed by applying the chain parameter analysis described by (4)–(7), and is shown as a reference. For the ideal system response, the ABCD parameters of the FSS have been computed from the single unit cell simulation in Figure 4b, using the infinite periodic boundary conditions capability of the simulator. This leads to a significantly shorter simulation time since the IRA is simulated apart from the FSS.

Despite the amplitude drop in the full-wave simulated IRA + FSS field, the intended passband effect holds around the resonant frequency of each unit-cell size, as can be seen in Figure 7b. Ideally, the impulse-like radiated pulse shall be converted into a signal with two different frequency components. However, harmonic resonances from the unit cells limit the bandwidth operation of the integrated radiator, as observed in the overlapped band around 2.6 GHz.

A symmetric and still directive radiation pattern can be expected, since the structure symmetry of the original IRA is not affected by adding the FSS, as it is shown in Figure 8. Significant degradation in the SLL ratio is observed in both frequency bands, especially in the E-plane. The effects of diffraction due to the FSS edges are evident but less severe at higher frequencies (i.e. 2.4 GHz). The maximum directivity is decreased from 18 dBi to 11 dBi at 1.5 GHz, while remained 22 dBi at 2.4 GHz (see Figure 8). This response is in accordance with the higher field strength around 2.4 GHz, once the wave passes through the FSS (see Figure 7b). One possible solution for this problem can be simply increasing the total area of the FSS, at the expense of affecting the manageability of the radiator. Furthermore, the reduced radiation intensity on boresight at the lower frequency band, could also be associated with the electrical size of the simulated

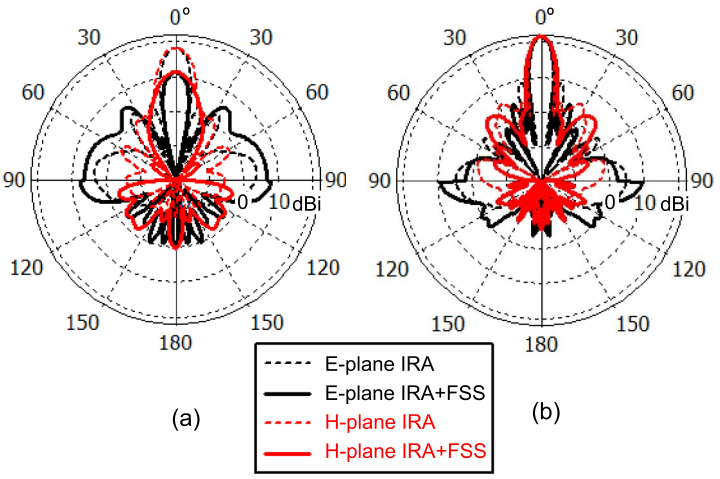

Figure 8. Radiation response of the integrated radiator, IRA + FSS (a) 1.5 GHz, and (b) 2.4 GHz. The radiation pattern from the unloaded IRA is shown as a reference.

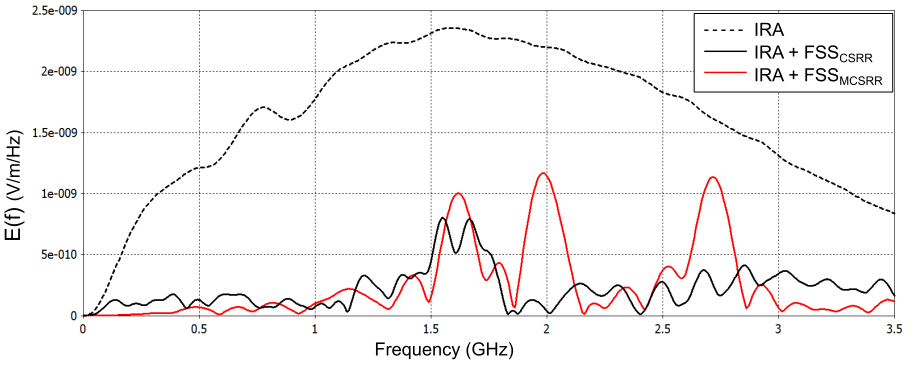

Figure 9. Spectral amplitude of the electric field amplitude, computed 5 m away from the Integrated HPM radiator, for both the CSRR- and the MCSRR-based FSS.

structure (1×1 m^2). Experimental validation is therefore required to confirm the influence of the finite-size FSS on the radiation diagram of the overall system.

The radiated field on boresight is computed for the MCSRR-based FSS. The numerical simulation is presented in Figure 9. Besides the drop in amplitude in the passing band in both, the CSRR- and the MCSRR-based FSS, the increase in the Q-factor is observed for the MCSRR case. Multiple bands for the MCSRR are observed as expected, due to the multiple coupling between the increased number of turns in the unit cell. In general, the resulting combination of the FSS with the IRA provides an efficient way to introduce the tunability and agility for multiple applications of the HPM source.

4. Conclusion

The concept of designing a narrowband HPM radiator is presented as the integration of a passband FSS with high Q-factor capabilities. An analytical approach to compute the radiated electric field is presented along with the fullwave simulation for validation. An enhanced FSS,

in terms of passband selectivity, is presented by implementing the axial-symmetric multiple-CSRR as unit cell. Computed results in terms of the field strength, spectral density of the electric field, and the radiation pattern of the integrated antenna system have been obtained. The presented approach is also applicable to other FSS geometries and UWB radiators. Currently, the implementation of a prototype of the proposed design is under process for experimental validation.

References

[1] D. D. V. Giri, F. M. Tesche, "Modeling of propagation losses in common residential and commercial building walls", 2013, http://ece-research.unm.edu/summa/notes/In/IN624.pdf, *Interaction Notes* 624, 24 pages, published by the Summa Foundation.

[2] D. V. Giri, R. Hoad, F. Sabath, "Implications of high-power electromagnetic (HPEM) environments on electronics", *IEEE Electromagn. Compat. Mag.* **9** (2020), no. 2, p. 37-44.

[3] C. E. Baum, "Radiation of impulse-like transient fields", 1989, http://ece-research.unm.edu/summa/notes/SSN/note321.pdf, *Sensor and Simulation Notes* 321, 28 pages, published by the Summma Foundation.

[4] C. E. Baum, E. G. Farr, "Impulse radiating antennas", in *Ultra-Wideband, Short-Pulse Electromagnetics* (H. L. Bertoni, L. Carin, L. B. Felsen, eds.), vol. 2, Springer US, Boston, MA, 1993, p. 139-147.

[5] F. M. Tesche, D. V. Giri, "Modification of impulse-radiating antenna waveforms for infrastructure element testing", 2015, http://ece-research.unm.edu/summa/notes/SSN/SSN572.pdf, *Sensor and Simulation Notes* 572, 25 pages, published by the Summa Foundation.

[6] W. Bigelow, E. Farr, J. S. Tyo, "A frequency selective surface used as a broadband filter to pass low-frequency UWB while reflecting X-band radar", 2006, http://www.farr-research.com/Papers/ssn506.pdf, *Sensor and Simulation Notes* 506, 17 pages, published by the Summa Foundation.

[7] C. Yang, P.-G. Liu, X.-J. Huang, "A novel method of energy selective surface for adaptive HPM/EMP protection", *IEEE Antennas Wirel. Propag. Lett.* **12** (2013), p. 112-115.

[8] S. Monni, D. J. Bekers, M. van Wanum, R. van Dijk, A. Neto, G. Gerini, F. E. van Vliet, "Limiting frequency selective surfaces", in *2009 European Microwave Conference (EuMC)*, IEEE, 2009, p. 606-609.

[9] M. Mavridou, K. Konstantinidis, A. Feresidis, P. Gardner, "Novel tunable frequency selective meta-surfaces", in *2016 46th European Microwave Conference (EuMC)*, IEEE, 2016, p. 301-304.

[10] D. Li, T. Li, E. Li, Y. Zhang, "A 2.5-D angularly stable frequency selective surface using via-based structure for 5G EMI shielding", *IEEE Trans. Electromagn. Compat.* **60** (2017), no. 3, p. 768-775.

[11] B. A. Munk, *Frequency Selective Surfaces: Theory and Design*, John Wiley & Sons, New York, 2005.

[12] J. B. Pendry, A. J. Holden, D. J. Robbins, W. J. Stewart, "Magnetism from conductors and enhanced nonlinear phenomena", *IEEE Trans. Microw. Theory Techniq.* **47** (1999), no. 11, p. 2075-2084.

[13] R. Marqués, J. D. Baena, M. Beruete, F. Falcone, T. Lopetegi, M. Sorolla, F. Martín, J. Garcia, "Ab initio analysis of frequency selective surfaces based on conventional and complementary split ring resonators", *J. Opt. A: Pure Appl. Opt.* **7** (2005), no. 2, p. S38-S43.

[14] J. D. Ortiz, J. D. Baena, V. Losada, F. Medina, J. L. Araque, "Spatial angular filtering by FSSs made of chains of interconnected SRRs and CSRRs", *IEEE Microw. Wirel. Compon. Lett.* **23** (2013), no. 9, p. 477-479.

[15] F. Bilotti, A. Toscano, L. Vegni, "Design of spiral and multiple split-ring resonators for the realization of miniaturized metamaterial samples", *IEEE Trans. Antennas Propag.* **55** (2007), no. 8, p. 2258-2267.

[16] J. D. Baena, J. Bonache, F. Martin, R. M. Sillero, F. Falcone, T. Lopetegi, M. A. G. Laso, J. Garcia-Garcia, I. Gil, M. F. Portillo, M. Sorolla, "Equivalent-circuit models for split-ring resonators and complementary split-ring resonators coupled to planar transmission lines", *IEEE Trans. Microw. Theory Techniq.* **53** (2005), no. 4, p. 1451-1461.

[17] R. Marques, F. Mesa, J. Martel, F. Medina, "Comparative analysis of edge- and broadside-coupled split ring resonators for metamaterial design—theory and experiments", *IEEE Trans. Antennas Propag.* **51** (2003), no. 10, p. 2572-2581.

[18] O. V. Mikheev, S. A. Podosenov, K. Y. Sakharov, A. A. Sokolov, Y. G. Svekis, V. A. Turkin, "New method for calculating pulse radiation from an antenna with a reflector", *IEEE Trans. Electromagn. Compat.* **39** (1997), no. 1, p. 48-54.

[19] F. M. Tesche, M. Ianoz, T. Karlsson, *EMC Analysis Methods and Computational Models*, John Wiley & Sons, New York, 1996.

Comptes Rendus
Physique
2021, 22, nº S1, p. 83-93
https://doi.org/10.5802/crphys.67

URSI-France 2020 Workshop / *Journées URSI-France 2020*

Compatibility between EESS (passive) in band 23.6–24 GHz and 5G in band 24.25–27.5 GHz

Thibaut Caillet [a]

[a] Direction de la Prospective du Spectre et des Affaires Européennes, ANFR - Agence Nationale des Fréquences, BREST, France
E-mail: thibaut.caillet@anfr.fr

Abstract. The 24.25–27.5 GHz band was allocated to IMT (International Mobile Telecommunication) during the World Radiocommunication Conference (WRC) after studies were elaborated between this potential allocation and the services in adjacent band and in particular with Earth Exploration by satellite in adjacent band. Several studies were evaluated during the WRC-19 cycle. This document describes only the studies undertaken by some European states for the protection of Earth exploration by satellite. The elements provided in this document are the basis of the European position for WRC-19 on the protection of passive EESS in 23.6–24 GHz.

Keywords. WRC-19, Passive EESS, 5G, Unwanted emissions, Sensors, IMT, Resolution ITU-R 750.
Available online 6th May 2021

1. Introduction

Many bands have been proposed for new IMT allocations during the cycle of WRC-19 under agenda item 1.13 (24.25–27.5 GHz, 31.8 33.4 GHz, 37–40.5 GHz, 40.5–42.5 GHz, 42.5–43.5 GHz, 45.5–47 GHz, 47–47.2 GHz, 47.2–50.2 GHz, 50.4–52.6 GHz, 66–71 GHz, 71–76 GHz and 81–86 GHz). These bands have been chosen primarily for the introduction of 5G broadband equipment in urban and suburban environments. Nine of these bands were already allocated to the mobile service, but by definition, an identification of the band by IMT changes the sharing conditions between the mobile service and other services in the band or adjacent band. The band 24.25–27.5 GHz appeared quickly the more appropriate band for 5G enabling at the same time, best propagation condition (in regards of other higher bands) and good data transfer capacities.

2. Usage and status of the band 23.6–24 GHz

Typically in the 22.21–22.5 GHz and 23.6–24 GHz bands, passive measurements focus primarily on the quantification and characterization of atmospheric water vapor [1]. The protected bands in this range are therefore usually used for atmospheric sounding. However, in this frequency range, radiometric measurements of water vapor are generally made in the high 23.6–24 GHz band in order to replace the strong dynamics of signals from the resonance of H_2O in 22.21–22.5 GHz. The 23.6–24 GHz bands is essential to all measurement performed in other passive

Table 1. Protection criteria of passive sensor in the band 23.6–24 GHz

Frequency band (GHz)	Total bandwidth (MHz)	Reference bandwidth (MHz)	Maximum interference level (dBW)	Percentage of area or time permissible interference level may be exceeded[(1)]
23.6–24	400	200	−166	0.01

[(1)] For a 0.01% level, the measurement area is a square on the Earth of 2000,000 km.

bands by radiometer by enabling the correction of these measurements in presence of water vapor.

Today, the World Meteorological Organization (WMO) has identified approximately 70 satellites in orbit that perform passive measurements in the 23.6–24 GHz band using a radiometer. Most of the listed satellites are meteorological and in particular:

- METOP satellites from Eumetsat operating AMSU-A (Advanced Microwave Sounding Unit—15 channels from 23 to 89 GHz [2]), MWS or MWI type radiometers.
- ROSHYDROMET satellite from Russians, METEOR type satellites carrying MTVZA-GY type radiometers (Advanced Microwave Sounding Unit—21 channels from 10.6 to 183 GHz [3]).
- NOAA US, NOAA or JPSS type satellites carrying AMSU-A type sensors.
- Chinese CMA, FY type satellites carrying MWRI (Micro-Wave Radiation Imager—6 channels from 10.65 to 150 GHz) or MWTS type radiometers.

In terms of status, the band 23.6–24 GHz bands is internationally protected by Radio Regulation in the footnote RR 5.340 (“all emissions are prohibited”).

3. Characteristics of EESS systems operating in the band 23.6–24 GHz

The various radiometers carried by these satellites are characterized today in Recommendation ITU-R RS.1861 [4]. It precisely defines all the parameters of these sensors (maximum size and gain of the antenna, integration period, etc.) as well as the orbital specificities of the satellites that transport them. The sensors are generically specified in the Recommendation (and not directly named). In the frequency band 23.6–24 GHz, 8 sensors are described.

The Recommendation ITU-R RS.2017 [5] defines the protection criteria to be respected for the proper use of these radiometers. From a practical point of view, interfering emissions have the consequence of increasing the noise level of the receiver and therefore degrading its sensitivity. The protection criterion is therefore defined as an acceptable temperature variation of the noise of the radiometric receiver by the presence of an interfering emission (transcribed in terms of power in dBW). This variation is associated with a percentage of time during which this level must not be exceeded. In the 23.6–24 GHz band, the artificial interference in the receiver must not exceed the smallest measurable noise temperature difference (equal to 0.05 °K) during 99.99% of the time. In terms of power, this means that interference from all emission sources should not exceed −166 dBW/200 MHz for 99.99% of the time (Table 1). The measurement area, on which this percentage applied is a surface of 2000,000 km^2.

Due to the surrounding of the passive band by several active systems, one apportionment of the protection criteria was introduced. Below the passive band, the Fixed Service (FS) is massively deployed and above, the IMT will be introduced. The unwanted emission of this two services fall into the passive band 23.6–24 GHz and an apportionment of 3 dB are then applied to the protection criteria to ensure the compliance of the EESS protection from emission of both active services together. The acceptable interference power becomes −169 dBW/200 MHz for 0.01% of the time for IMT.

4. Characteristics of IMT systems operating in the band 24.25–27.5 GHz

Table 2 provides the planned characteristic of IMT in the band 24.25–27.5 GHz. These parameters were defined by the ITU-R expert group of IMT (Working Party 5D) several particularities have to be highlighted:

1. The 5G Network in millimetric band is based on Time Duplex Division, enabling some exchange in time between Base Station (BS) and User Equipment (UE) on the same frequency channel. The division in time (activity factor) is respectively 80% for the BS and 20% for the UE.
2. The unwanted emissions of BS and UE in the band 23.6–24 GHz are defined in terms of Total Radiated Power (TRP) and represent respectively −24 dBW/200 MHz and −20 dBW/200 MHz (3 dB of ohmic losses were applied to the estimated unwanted conducted power). This TRP is defined as the power radiated in the entire sphere around the antenna.
3. The BS and UE antennas used for 5G are Active Antenna System (AAS) and their beams are respectively formed by 8 × 8 or 4 × 4 radiated elements presented each an intrinsic gain of 5 dBi. Their antenna pattern is modeled in the Recommendation ITU-R M.2101 [6].
4. The BS and UE antennas, always point their maximum gain toward each other during communication.
5. Due to power control, the power transmit by the UE is not constant and depends on its position from the BS. The deployment considers that 5% of UE could be indoors.
6. Due to the number of UEs connected to BS, the maximum power of the BS is distributed on each UE.
7. In an IMT cell, for one operator, the proposed deployment consists in one BS and 3 UEs.
8. A channel aggregation factor of 2 dB was used in order to mainly take into account the summation of power in the passive band of the unwanted emission of IMT 2020 channels used by different operators.
9. The distribution of UEs in the BS coverage follows a Rayleigh distribution in terms of distance from BS ($\sigma = 32$) and a normal distribution in regards of its position in azimuth ($\mu = 0°$ and $\sigma = 30°$).
10. The proposed deployments of BS and UE per km^2 are provided in Table 2 (from 30 to 10 BS/km^2 for respectively urban and suburban deployment). It has to be noted that the deployment needs to be reevaluated by two factors Ra and Rb. Ra represents the real coverage rate of equipment in a building area (city) and Rb the rate of building area in a specific environment (urban, suburban, rural...).

During the cycle of studies, two different assumptions were discussed on the behavior of AAS antenna in unwanted domain (or more precisely in the band 23.6–24 GHz). Two options were assumed:

1. In unwanted domain, the correlation between radiated elements totally disappears and the antenna is not able to shape the main beam and the side lobes in an appropriate way. The radiated pattern could be described as the pattern of a single element (closed to omnidirectional) and the global antenna is not able to perform electrical pointing.
2. In unwanted domain, due to the facts that IMT equipment will be designed to operate in a large band (3.25 GHz) and that a low frequency distance between the center frequency of IMT equipment and passive band will exist (250 MHz, that means 1/13 of the total band), the AAS will be able to create beamforming in adjacent band. In this particular case, the parameter of the M.2101 model was modified in order to take into account the

Table 2. Parameter of simulations

Sensor	F1	F2	F3	F4		F5		F6	F7		F8
Type of sensor	Conical	Conical	Conical	Mechanical (cross-track)		Mechanical (cross-track)		Conical	Push-broom		Conical
Sensor geometric characteristics											
Orbit altitude (km)	817	705	828	833		824		835	850		699.6
Nadir angle (°)	44.5	47.5	46.6	±48.33	0.0	±52.725	0.0	55.4	±50	0.0	47.5
Elev at ground Θ (°)	37.7	35.0	34.8	32.4	90.0	26.01	90.0	21.4	29.7	90.0	35.1
Slant path distance (km)	1228	1124	1309	1378	833	1563	824	1767	1482	850	1114
Footprint size (km^2)	1880	452	169	9298	1847	35,983	4395	2430	201	201	306
Antenna gain (dBi)	40	46.7	52	34.4	34.4	30.4	30.4	43	45	45	48.5
Protection criteria (dBW/200 MHz)	−166	−166	−166	−166	−166	−166	−166	−166	−166	−166	−166
Apportionment (dB)	3	3	3	3	3	3	3	3	3	3	3
Propagation losses											
Free space losses (dB)	181.72	180.95	182.27	182.72	178.34	183.81	178.25	184.88	183.35	178.52	180.87
Atmospheric losses (dB)	0.69	0.73	0.74	0.78	0.42	0.95	0.42	1.15	0.85	0.42	0.73
Clutter losses (dB)[5]	Distributed (see Figure 1)										
Polarisation losses (dB)	3	3	3	3	3	3	3	3	3	3	3
Urban BS characteristics											
Unwanted emission (dBW/200 MHz)	−21	−21	−21	−21	−21	−21	−21	−21	−21	−21	−21
Ohmic losses (dB)	−3	−3	−3	−3	−3	−3	−3	−3	−3	−3	−3
Unwanted TRP (dBW/200 MHz)	−24	−24	−24	−24	−24	−24	−24	−24	−24	−24	−24
Urban deployment (BS/km^2)	30	30	30	30	30	30	30	30	30	30	30
Urban area (km^2)	200	200	169	200	200	200	200	200	200	200	200
Ra (%) urban	7%	7%	7%	7%	7%	7%	7%	7%	7%	7%	7%
Number of BS[1]	420	420	338	420	420	420	420	420	420	420	420
Sensor geometric characteristics											
Suburban Deployment (BS/km^2)	10	10	10	10	10	10	10	10	10	10	10
Remaining area (km^2)	1680	252	−31	9098	1647	35,783	4195	2230	1	1	106
Ra (%) suburban	3%	3%	3%	3%	3%	3%	3%	3%	3%	3%	3%
Rb (%)	5%	5%	5%	5%	5%	5%	5%	5%	5%	5%	5%
Number of BS[1] in remaining area	202	30	0	1092	198	4294	503	268	0	0	13
Total number of BS	622	450	420	1512	618	4714	923	688	420	420	433
Loading factor (%)	20	20	20	20	20	20	20	20	20	20	20
TDD factor (%)	80	80	80	80	80	80	80	80	80	80	80
Antenna gain (dBi)[2]	Distributed										
Channel Aggregation (dB)	2	2	2	2	2	2	2	2	2	2	2
Urban UE characteristics											
Unwanted emission (dBW/200 MHz)	−17	−17	−17	−17	−17	−17	−17	−17	−17	−17	−17
Ohmic losses (dB)	−3	−3	−3	−3	−3	−3	−3	−3	−3	−3	−3
Unwanted TRP (dBW/200 MHz)	−20	−20	−20	−20	−20	−20	−20	−20	−20	−20	−20
Mean power control attenuation (dB)	Distributed										

(continued on next page)

Table 2. (continued)

Sensor	F1	F2	F3	F4		F5		F6	F7		F8
Type of sensor	Conical	Conical	Conical	Mechanical (cross-track)		Mechanical (cross-track)		Conical	Push-broom		Conical
Urban deployment (UE/km^2)	100	100	100	100	100	100	100	100	100	100	100
Urban area (km^2)	200	200	169	200	200	200	200	200	200	200	200
Ra (%)	7	7	7	7	7	7	7	7	7	7	7
Number of UE[(1)]	1400	1400	1183	1400	1400	1400	1400	1400	1400	1400	1400
Suburban deployment (UE/km^2)	30	30	30	30	30	30	30	30	30	30	30
Suburban area (km^2)	1680	252	0	9098	1647	35,783	4195	2230	1	1	106
Ra (%)	3	3	3	3	3	3	3	3	3	3	3
Rb (%)	5	5	5	5	5	5	5	5	5	5	5
Number of UE[(1)]	664	100	0	3594	651	14,134	1657	881	0	0	42
Total number of UE	2064	1500	1183	4994	2051	15,534	3057	2281	1400	1400	1442
Loading factor (%)	20	20	20	20	20	20	20	20	20	20	20
TDD factor (%)	20	20	20	20	20	20	20	20	20	20	20
Antenna gain (dBi)[(2)]	Distributed										
Body loss (dB)	−4	−4	−4	−4	−4	−4	−4	−4	−4	−4	−4
Channel aggregation (dB)	2	2	2	2	2	2	2	2	2	2	2
Total received power by sensor from UE and BS											
Interference power (dBW/200 MHz)	Distributed (see Section 6)										

changes in terms of wavelength of the radiated element and the spacing between them in the unwanted domain.

5. Scenario of study

5.1. *Surface of study and IMT deployment*

The scenario of study is principally based on the characteristics and protection of Earth Exploration satellites. If some consideration of long time is taken, it is possible to establish that the satellite footprints cover uniformly all the Earth surface on which the sensor could fly (depending of its orbit inclination). The acceptable interference power can exceed −169 dBW/200 MHz for 0.01% of the time. As depicted in the Recommendation ITU-R RS.2017, this criterion has to be applied to a surface on the Earth of 2000,000 km^2. Considering the long time assumption, the 0.01% of time can be translated as 0.01% of the surface and finally the protection criteria should be respected if only a surface of 200 km^2 presents an exceedance of power. This kind of surface is closed to the surface of a city like Paris.

In the deployment of BS and UE in the satellite footprints, the Ra and Rb parameters are used. If the considered sensor footprint is:

1. Lower than the city dimension, only the value of Ra for urban environment was used (Rb was taken equal to 1).
2. Higher that the city, the value of Ra for urban environment was used only on 200 km^2 of the footprint and the value of Ra and Rb for suburban environment was used in the remaining area.

For each footprint, the total number of deployed equipment is calculated based on the previous element. In a second step, the total number of equipment that emit in the same time

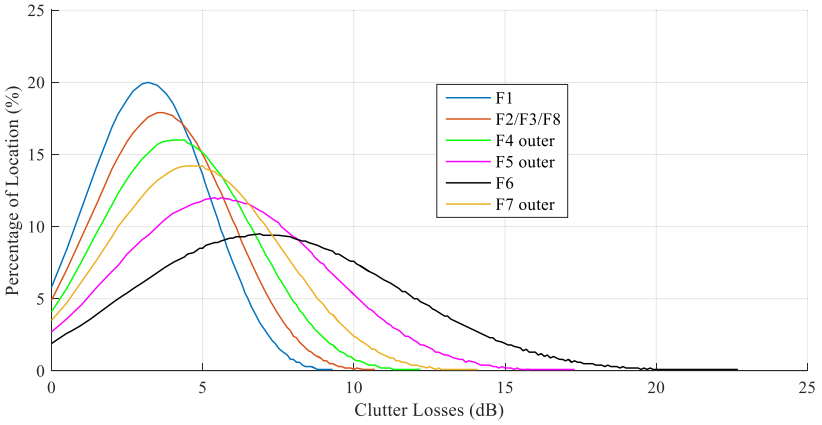

Figure 1. Distribution of clutter losses for different elevation angle between mobile systems and satellite. Elevation is taken from ground.

is assumed by using the loading factor (20%). And finally the global emission toward satellite is split between 80% of BSs and 20% of UEs.

5.2. *Losses between IMT network emissions and satellite*

The losses between active IMT systems and passive satellite can be summarized as:

1. Free space losses calculated on the slant path distance. From the satellite, all emitters in the footprint can be "seen" as an aggregation of emitters deployed on a point. The distance between all emitters in the footprint and the satellite are identical.
2. Atmospheric losses, based on Recommendation ITU-R P.676 [7].
3. Clutter losses extracted form Recommendation ITU-R P.2108 [8] for different incident angles from the ground (angle under which that emitters "see" the satellite). Figure 1 presents the Probability Distribution Functions (PDF) of clutter for different elevation angle (matching with the elevations of the sensors from ground). For an elevation angle of 90°, when satellite is in the zenith of IMT equipment (i.e., nadir of mechanical sensor satellite) the clutter losses are equal to 0 dB.
4. 3 dB of polarization losses due to the IMT emissions in cross polarization and the EESS reception in linear.

5.3. *Simulations*

The simulations were performed for each footprint, considering the total number of equipment (Table 2). Between each snapshot (Figure 2), most of parameters are considered as fixed, except the position of UEs in regard of BSs resulting in some changes for:

1. The antenna gains from BS to UE and reciproqually and from BS/UE to EESS satellites.
2. The UE conducted power, as a consequence of the UE power control.
3. The Clutter losses in a given elevation. Each snapshot, this factor is randomly chosen for each path between UEs and BS towards satellite (considering it elevation angle from ground).

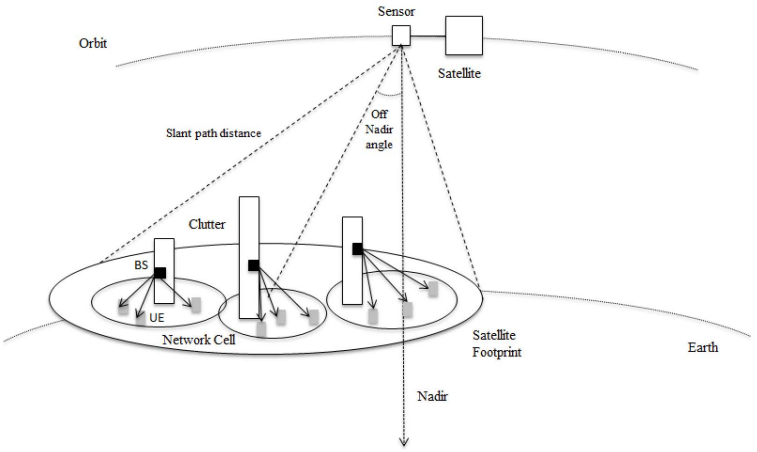

Figure 2. Scenario of simulations.

The total interference level I_{tot} (in linear) in the satellite sensor F_x can be expressed as:

$$I_{\text{tot}} = 10^{\left[\frac{(G_{\text{sat}}+\text{AF})}{10}\right]}\left[F_{\text{BS}}\sum_{i=1}^{i=\text{Nb}_{\text{BS}}} 10^{\left[\frac{(P_{\text{BS}_i}+G_{\text{BS}_i}-L_{\text{BS}_i})}{10}\right]} + F_{\text{UE}}\sum_{j=1}^{j=\text{Nb}_{\text{UE}}} 10^{\left[\frac{(P_{\text{UE}_i}+G_{\text{UE}_i}-L_{\text{UE}_i})}{10}\right]}\right]$$

where

- Nb_{BS} and Nb_{UE}: the total number of active BS and UE in the footprint of F_x
- F_{BS} and F_{UE}: the TDD factor of active BSs and UEs in the footprint (%)
- P_{BS_i} and P_{UE_i}: the conduced power of the ith BS or jth UE (dBW/200 MHz)
- G_{sat}: the satellite gain (dBi)
- L_{BS_i}: the total losses between BS_i and satellite. These losses include free space on the slant path, clutter, polarization and atmospheric losses (dB)
- L_{UE_i}: the total losses between UE_i and satellite. This losses are equal to L_{BS_i} with additional losses due to body loss (dB)
- AF: Multi-operator aggregation factor (dB).

6. Results

The following Table 4 provides the summary of some results of Monte Carlo simulations performed on all sensors considering the antenna pattern in adjacent band as single element or as beamforming antenna.

In the case of beamforming in unwanted domain, the result of interference is taken at 99% of the interference cumulative distribution. In the case of single element behavior in unwanted domain, the result of interference is based on the average (weighted sum) of the distribution.

This choice of result analysis could be explained by two different facts:

1. First, the spread of the distribution of interference when beamforming assumptions are considered in the passive band. Globally for conical sensors that point every time in the same elevation, the dynamics of the distribution considering the single element assumption is around 6 dB. In the case of beamforming pattern assumptions, this dynamics is between 11 to 14 dB.
2. Secondly, 99% of the interference, for beamforming assumption, could be explained by the fact that 2000,000 km^2 represent approximately half of the European Union surface

Table 3. Summary of results: Monte Carlo simulation for both assumptions in adjacent band (single element and beamforming antenna)

Sensor		F1	F2	F3	F6	F8
Beamforming antenna	99% (dBW/200 MHz)	−160.2	−153.3	−150.6	−161.6	−151.5
	Margin (dB)	8.8	15.7	18.4	8.4	17.5
Single element	Average (dBW/200 MHz)	−153.8	−147.5	−144.6	−153.5	−145.8
	Margin (dB)	15.2	21.5	24.4	15.5	23.2

Conical sensors (F1, F2, F3, F6 and F8).

Table 4. Summary of results: Monte Carlo simulation for both assumptions in adjacent band (single element and beamforming antenna)

Sensor		F4		F5		F7	
Footprint position		Nadir	Outer	Nadir	Outer	Nadir	Outer
Beamforming antenna	99% (dBW/200 MHz)	−162	−165	−165	−168	−152.9	−157.6
	Margin (dB)	7	4	4	1	16.1	11.4
Single element	Average (dBW/200 MHz)	−161.7	−156	−163.9	−156	−153	−151.5
	Margin (dB)	7.3	13	7.1	13	16	17.5

Mecanical sensors (F4, F5, F7).

and in this area, at least 100 cities present a surface closed or higher than 200 km^2, so only one "pixel" of 200 km^2 can exceed the protection criteria.

As shown in Figures 3 and 4, considering only the shape of the distribution, the interference increases by around 10 to 15 dB for high percentage and by 5 to 7 dB in low percentage if the "single element" assumption is taken to model the antenna behavior in adjacent band.

The studies have shown that the sensor F3 was the most sensitive sensors to interference from IMT 2020 in both assumptions of antenna radiation pattern. The position of CEPT was based on the capability of AAS to build a beam in adjacent band and a reduction of IMT unwanted emission by 18 dB (Table 3 for F3) was proposed in order to ensure the protection of every sensors, resulting of unwanted emission of respectively −42 and −38 dBW/200 MHz for BS and UE.

During WRC-19, the final decision, based on a two-steps principle was inserted in the Resolution ITU-R 750 [9]:

1. In a first time, a reduction of 9 dB (−33 and −29 dBW/200 MHz for BS and UE) is imposed to IMT equipment. This value is mandatory until September 2027.
2. After this date, the reduction will be equal to 15 dB (−39 and −35 dBW/200 MHz for BS and UE).

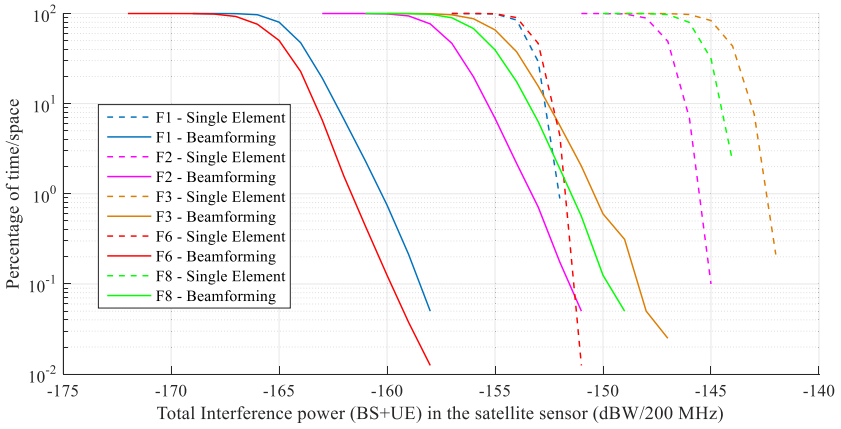

Figure 3. Distribution of interference power in conical sensors (F1, F2, F3, F6 and F8).

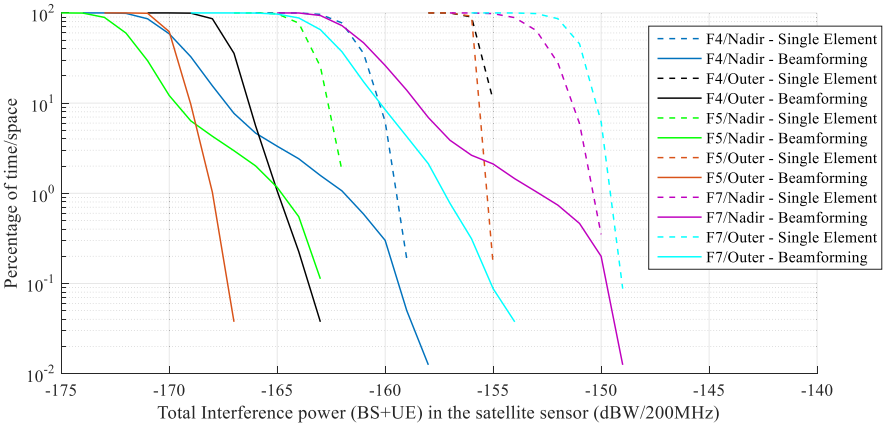

Figure 4. Distribution of interference power in mechanical sensors (F4, F5 and F7).

Europe, by ECC, took the decision to minimize the impact of IMT on passive EESS by reducing the time during which the unwanted emission will be higher. In Europe, the 15 dB of reduction will apply from January 2024 instead of September 2027. In addition, since the long term limit of −39 dBW/200 MHz, instead of −42 dBW/200 MHz, was justified by not taking into account the 3 dB apportionment factor, Europe also enshrined in its decisions that the frequency band below 23.6 GHz shall not be used by high density broadband systems.

7. Conclusions and discussion

This document proposed to explain the calculation performed by some European States in order to protect the meteorological space system in the band 23.6–24 GHz. All the parameters and assumptions provided in this document were intensively discussed during the WRC-19 cycle in ITU (International Telecommunication Union) and some of them were not agreed by all member States. Particularly, it was the case for the 2 dB of channel aggregation and the 3 dB of protection criteria apportionment.

Based on these assumptions, the European position to WRC-19 was to impose a reduction of 18 dB to IMT system in the unwanted domain. Long discussions took place during the WRC and some compromises were made, coming to an approach in two steps.

With or without these elements, the Sensors F3 seems to be the most sensitive sensors to interference. It can be mostly explained by its high gain (52 dBi) in regards of the other sensor gains. It should be noted that this sensor is planned to be used but not deployed yet in space. However, it could be noticed that the results of studies for sensors F2 and F8, already in orbit, are closed to those for F3 by respectively around 3 dB and 1 dB. Their respective antenna presents a lower gain than F3 antenna but in the same time their own slant path distance is lower too (so the propagation losses are lower).

The way to model the IMT antenna has an important impact on the results. The decision was taken for WRC-19 to use the assumption of beamforming in adjacent band. Some monitoring of effective IMT stations and deployment parameters (including active antenna but also base station density, real unwanted emission level, tilt statistic, etc.) will be necessary to ensure the absence of satellite interference in the long term.

Abbreviations

AAS	Active Antenna System
AMSU	Advanced Microwave Sounding Unit
BS	Base Station
CEPT	Conférence Européenne des Administrations des Postes et des Télécommunications
CMA	China Meteorological Administration
CMR	Conférence Mondiale des Radiocommunications
ECC	Electronic Communications Commitee
EESS	Earth Exploration Satellite Systems
IMT	International Mobile Telecommunication
ITU	International Telecommunication Union
JPSS	Joint Polar Satellite System
MWI	Microwave Imager
MWRI	Micro-Wave Radiation Imager
MWS	Microwave Sounder
MWTS	Microwave Temperature Sounding
NOAA	National Oceanic and Atmospheric Administration
SETS	Service d'Exploration de la Terre par Satellite
UE	User Equipment
UIT	Union Internationale des Télécommunications
WMO	World Meteorological Organization
WRC	Word Radiocommunication Conference

References

[1] Meens, Vincent and others, "Handbook. Use of Radio Spectrum for Meteorology: Weather, Water and Climate Monitoring and Prediction", 2008, https://www.itu.int/dms_pub/itu-r/opb/hdb/R-HDB-45-2008-PDF-E.pdf.

[2] F. Karbou, C. Prigent, L. Eymard, J. R. Pardo, "Microwave land emissivity calculations using AMSU measurements", *IEEE Trans. Geosci. Remote Sens.* **43** (2005), no. 5, p. 948-959.

[3] I. V. Cherny, L. M. Mitnik, A. B. Uspensky, A. M. Streltsov, "On-orbit calibration of the "Meteor-M" microwave imager/sounder", in *IEEE International Geoscience & Remote Sensing Symposium, IGARSS 2010, July 25–30, Honolulu, Hawaii, USA*, IEEE, 2010.

[4] ITU-R Radiocommunication Sector of ITU, "Typical technical and operational characteristics of Earth exploration-satellite service (passive) systems using allocations between 1.4 and 275 GHz", Tech. Report ITU-R RS.1861, International Telecommunication Union, 2010, published in the *RS Series Remote sensing systems*, https://extranet.itu.int/brdocsearch/R-REC/R-REC-RS/R-REC-RS.1861/R-REC-RS.1861-0-201001-I/R-REC-RS.1861-0-201001-I!!PDF-E.pdf.

[5] ITU-R Radiocommunication Sector of ITU, "Performance and interference criteria for satellite passive remote sensing", Tech. Report ITU-R RS.2017-0, International Telecommunication Union, 2012, published in the *RS Series Remote sensing systems*, https://www.itu.int/dms_pubrec/itu-r/rec/rs/R-REC-RS.2017-0-201208-I!!PDF-E.pdf.

[6] ITU-R Radiocommunication Sector of ITU, "Modelling and simulation of IMT networks and systems for use in sharing and compatibility studies", Tech. Report ITU-R M.2101-0, International Telecommunication Union, 2017, published in the *M Series Mobile, radiodetermination, amateur and related satellite services*, https://www.itu.int/dms_pubrec/itu-r/rec/m/R-REC-M.2101-0-201702-I!!PDF-E.pdf.

[7] ITU-R Radiocommunication Sector of ITU, "Attenuation by atmospheric gases and related effects", Tech. Report ITU-R P.676-12, International Telecommunication Union, 2019, published in the *P Series Radiowave propagation*, https://www.itu.int/dms_pubrec/itu-r/rec/p/R-REC-P.676-12-201908-I!!PDF-E.pdf.

[8] ITU-R Radiocommunication Sector of ITU, "Prediction of clutter loss", Tech. Report ITU-R P.2108-0, International Telecommunication Union, 2017, published in the *P Series Radiowave propagation*, https://www.itu.int/dms_pubrec/itu-r/rec/p/R-REC-P.2108-0-201706-I!!PDF-E.pdf.

[9] International Telecommunication Union, "Resolution ITU-R 750 (REV.WRC-19). Compatibility between the Earth exploration satellite service (passive) and relevant active services", 2019, 517-524 pages.

Comptes Rendus

Physique

Objet de la revue

Les *Comptes Rendus Physique* sont une revue électronique évaluée par les pairs de niveau international, qui couvre l'ensemble des domaines de la physique et de l'astrophysique. Ils publient principalement des numéros thématiques, mais également des articles originaux de recherche, des annonces préliminaires, des articles de revue, des mises en perspective historiques, des textes à visée pédagogique ou encore des actes de colloque, sans limite de longueur, en anglais ou en français. Ils proposent également des numéros spéciaux consacrés à certains aspects récents et/ou significatifs de la discipline, dont les auteurs sont choisis parmi les chercheurs les plus actifs sur le sujet et dont la coordination est assurée par des rédacteurs en chef invités.

Les *Comptes Rendus Physique* sont diffusés selon une politique vertueuse de libre accès diamant, gratuit pour les auteurs (pas de frais de publications) comme pour les lecteurs (libre accès immédiat et pérenne).

À propos de la revue

Toutes les informations concernant la revue, y compris le texte des articles publiés qui est en accès libre intégral, figurent sur le site https://comptes-rendus.academie-sciences.fr/physique/.

Informations à l'attention des auteurs

Pour toute question relative à la soumission des articles, les auteurs peuvent consulter le site https://comptes-rendus.academie-sciences.fr/physique/.

Contact

Académie des sciences
23, quai de Conti, 75006 Paris, France
Tél. : (+33) (0)1 44 41 43 72
CR-Physique@academie-sciences.fr

Comptes Rendus
de l'Académie des sciences

Physique

Volume 22, nº S1, 2021

Special issue / *Numéro thématique*
URSI-France 2020 Workshop / *Journées URSI-France 2020*

Guest editor / *Rédacteur en chef invité*
Joe Wiart (LTCI, Télécom Paris, Institut Polytechnique de Paris, Institut Mines-Télécom, France)

1878-1535 (electronic)

Académie des sciences — Paris

COMPTES RENDUS
DE L'ACADÉMIE DES SCIENCES

Physique

Volume 22, n° S1, 2021